

Photo and Auger Electron Angular Distributions of  
Fixed-in-Space CO<sub>2</sub>  
Diplomarbeit

von

Felix Paul Sturm

Juni 2009



Hochschullehrer:  
Betreuer am LBNL:

Prof. Dr. Reinhard Dörner  
Dr. Thorsten Weber

Goethe Universität Frankfurt am Main, Institut für Kernphysik  
und  
Lawrence Berkeley National Laboratory,  
Chemical Sciences Division, Berkeley CA, USA



Ich versichere hiermit, dass ich die vorliegende Arbeit selbstständig verfasst, keine anderen als die angegebenen Hilfsmittel verwendet und sämtliche Stellen, die benutzten Werken im Wortlaut oder dem Sinne nach entnommen sind, mit Quellen bzw. Herkunftsangaben kenntlich gemacht habe.

Frankfurt am Main, den 6. September 2009

---



# Contents

<b>1</b>	<b>Introduction</b>	<b>3</b>
<b>2</b>	<b>Physical Background</b>	<b>7</b>
2.1	Quantum mechanics	7
2.2	Approximations in atomic physics	9
2.2.1	Born-Oppenheimer approximation	9
2.2.2	Dipole approximation	10
2.2.3	Franck-Condon principle	10
2.2.4	Axial recoil approximation	11
2.3	Photoionization	12
2.3.1	Auger decay in the two-step model	13
2.4	The carbon dioxide molecule	14
2.5	Experiments on $K$ -shell photoionization of $\text{CO}_2$	14
<b>3</b>	<b>Experimental Setup</b>	<b>17</b>
3.1	Vacuum system	17
3.2	Target	19
3.3	Spectrometer	23
3.3.1	Electrostatic lens	23
3.3.2	Geometry and resolution	25
3.4	Detectors and readout electronics	26
3.4.1	Signal acquisition and conversion	27
3.4.2	Time measurement	27
3.4.3	Operation specifications	27
3.5	Synchrotron light source	29
3.5.1	Focus adjustment	30
<b>4</b>	<b>Data Analysis</b>	<b>33</b>
4.1	Data readout	33
4.2	Momentum calculation	35
4.2.1	Time zero and magnetic field	35
4.2.2	Electron momentum	35
4.2.3	Ion momentum and electric field	37
4.3	Calibration and corrections	38
4.3.1	Photon energy calibration	39
4.3.2	Electron energy and momentum	39
4.3.3	Ion energy and momentum	40
4.4	Additional corrections	41
4.4.1	Electrostatic lens effects	41
4.4.2	Time dependent drifting effects	42
4.5	Error analysis	44
4.5.1	Experimental uncertainties	44
4.5.2	Statistical errors	45

---

<b>5</b>	<b>Results and Conclusions</b>	<b>47</b>
5.1	Breakup channels . . . . .	47
5.2	Photoelectron angular distributions . . . . .	49
5.3	Processes affecting MFPADs . . . . .	50
5.3.1	Post collision interaction . . . . .	52
5.3.2	Initial state correlation . . . . .	52
5.3.3	Vibrational modes . . . . .	54
5.4	Auger electron angular distributions . . . . .	56
<b>6</b>	<b>Summary and Outlook</b>	<b>61</b>
6.1	Summary . . . . .	61
6.2	Outlook . . . . .	61
	<b>Appendix</b>	<b>65</b>
1	Three-dimensional linear interpolation . . . . .	65
2	Vacuum data . . . . .	66
3	Statistical errors . . . . .	67
4	The chamber at BL 11.0.2 . . . . .	68
5	Atomic Units . . . . .	69
	<b>Bibliography</b>	<b>71</b>
	<b>Acknowledgements</b>	<b>77</b>
	<b>Index</b>	<b>79</b>

# 1 Introduction

If one looks at objects, animals or humans, symmetries can be found everywhere in Nature. In physics, the concept of symmetries plays a decisive role. *Noether's theorem* says that any (differential) symmetry leads to a conservation law such as energy- and momentum conservation. Therefore, searching for symmetries and symmetry operations is an important method of research. However, symmetries can be broken by various processes. In molecules, already single photons can destroy the initial symmetry, which was even observed in the smallest molecule  $\text{H}_2$  [31].

Our experiment tried to find the causes for a surprising symmetry breaking recently observed in  $\text{CO}_2$ . A group in Japan performed photoionization of carbon dioxide molecules with synchrotron light and found an asymmetry of the emission of carbon K-shell electrons with respect to the molecular axis. These *photoelectrons* scatter at the oxygen atoms forming an interference pattern which was investigated by the experimentalists. The singly ionized  $\text{CO}_2^+$  ions are highly excited and decay by emission of a second electron, called the Auger electron. Being doubly charged, the ions break up back-to-back into  $\text{CO}^+$  and  $\text{O}^+$ .

$\text{CO}_2$  is a linear molecule in which the carbon atom is positioned in between the two oxygen atoms. The carbon has the same distance to both oxygen atoms on its sides, resulting in a mirror symmetry of the oxygen atoms to the center of the carbon. The photoelectron originates from an orbital with spherical symmetry. On average, both the electron position as well as the position of the oxygen atoms are symmetric along the molecular axis with respect to the carbon nucleus. If the photoelectron leaves the carbon, and one counts how many electrons were emitted to each side of the linear ion, it would be expected to obtain the same amount on each side, because of the described mirror symmetry.

Instead, Liu *et al.* [30] found that the probability for emission in direction of the  $\text{CO}^+$  and the  $\text{O}^+$  ions was not equal, but higher for one of both sides, changing with the electron energy. They speculated over an explanation, but could not prove it, as they were missing some important information. They did not measure the Auger electron, the second electron emitted shortly after the photoelectron. In other experiments, interaction has been observed between the two electrons: while leaving the molecule, the very fast Auger electron can influence the slow photoelectron directly. The effect is known as *post collision interaction*, emphasizing an interaction after emission. Another possibility of interaction between the two electrons emerges from a quantum mechanical description. The observed link between Auger and photoelectron in the data could be caused by electron-electron correlation in the initial state. To summarize, it was possible that the observed asymmetry could not be explained without taking into account the Auger electron.

In order to illuminate this question, we performed the experiment reported in this work. We built a setup in which not only the electrons were measured with much improved resolution, but also we were able to observe the Auger electron and to inspect dependencies between these particles.

Common methods of investigation in atomic physics consist of directing photons, electrons or ions onto target atoms or molecules. The interaction of the projectile with the target contains information about the atomic system and its initial state. Interference patterns of scattered electrons reflect the structure of the molecule, and the measurement of electronic transitions displays energy levels existing in the system. In ion and electron collisions, the

momentum of the projectile is transferred to the target. It is important for the description of the observed process to define the momentum of the projectile, and this is one of the major difficulties in these experiments. In comparison, the interaction with light can be regarded as a very ‘pure’ method of investigation; as the momentum of the photons is too small to influence the system it can be neglected. The only effect of the photons on the atom is the deposition of energy and the transfer of a well defined angular momentum.

At standard temperature and pressure, CO<sub>2</sub> is a gas which is a part of the earth’s atmosphere and it is used by plants in photosynthesis. It is produced in many natural processes but also in the combustion of fossil fuels, as in cars or coal power plants. In the atmosphere, it transmits visible light, but absorbs light in the infrared and near-infrared regions, heating the earths temperature. Its role in the greenhouse effect has been the subject of many studies, whereas in this experiment the focus was on the observation of electronic effects in CO<sub>2</sub> as a linear molecule.

A number of effects can be treated semi-classically, but other surprising observations result entirely from the fundamental laws that characterize quantum theory. In the first chapter, the basics of quantum mechanics will be introduced together with a mathematical description. The theoretical background of this experiment and a model of Auger decay is described in more detail. The properties of the CO<sub>2</sub> molecule and experiments performed on K-shell photoionization are listed in the last sections.

The experimental technique and the components of the setup are described in the second chapter. The initial momenta of the particles involved in the reaction can be reconstructed from time and position information on detectors. A main challenge in this experiment was to achieve high momentum resolution in the measurement of the ions. It was not possible to detect both electrons with sufficient resolution, because their difference in energy was too large. Momentum conservation allows for the possibility of reconstructing one particle if the other particles are detected. Therefore, we decided to calculate the Auger electron momentum from its recoil on the other particles, but the small momentum of the Auger electron on the two heavy ions made a very precise measurement necessary. The high resolution measurement could be performed by modification of an already established experimental setup. Hereby, the concept of our three dimensional focusing spectrometer including the electrostatic lens are explained in Sec. 3.3. In a gas at room temperature, the momenta of the reaction could not be separated from thermal movement. This problem was addressed by providing the carbon dioxide molecules in form of a supersonic gas jet. In Sec. 3.2 the gas jet and its physical properties are described together with estimated parameters of the molecular jet. The standard parts of our setup, such as the detectors and the electronic devices were already treated in many other works and are outlined here only shortly, whereas the electronic logics setup needed for the three-particle coincident detection is visualized and explained in two figures. During the preparation of the experiment, a new device for photon beam focus measurement was designed, which is described in detail at the end of the chapter.

Chapter 4 leads step by step through the process of data analysis. A large part of the work in this experiment was the analysis of the obtained data. In order to obtain the initial momenta from the position of the particles and their time-of-flight onto the detectors, several levels of calculation and calibration are needed. This procedure as well as the formulae needed are noted and could serve as a manual for further experiments. The electrostatic lens improved the resolution of the recoil ions significantly but also added additional difficulties to the analysis. An interpolation function was written during this thesis for compensating for unwanted effects caused by the lens. Also, a correction for timef dependent drifting of the target position could be useful in the future.

Finally, all results are presented in the last chapter. We confirmed earlier results and were able to reveal new features in the photoelectron angular distributions. With our high statistics measurement, we found evidence for the origin of the asymmetry in the photoelectron angular distributions.



## 2 Physical Background

*Quantum mechanics* brought to an end the classical view of physics that everything in Nature could be described exactly if one looked just closely enough and knew its rules and laws. In Quantum mechanics all energy is quantized i.e. only exists in multiples of the *Planck constant*  $h$ . Heisenberg's uncertainty principle prohibits the achievement of more than a certain level of accuracy in measurements. Many puzzling effects like entanglement, where it seems as if particles were communicating instantaneously over infinite distances, are due to quantum mechanics. This fundamental change in the view of Nature and its laws has been discussed for many years, and despite all doubts and attempts to disprove this theory, it is now established in modern Physics

Some basics will be introduced in this section. Important approximations used in atomic physics are explained in separate sections. Nevertheless, one should be aware of the fact that this short description alone cannot be sufficient for real understanding of the effects caused by quantum mechanics. In Sec. 2.3, the focus turns on this experiment, where *Photoionization* was the method of investigation. The characteristics of the carbon dioxide molecule are described followed by an overview of previous experiments on *K-shell* photoionization in the last section.

### 2.1 Quantum mechanics

In quantum mechanics, a particle cannot be described by a set of coordinates and properties, but instead by a *wavefunction* or 'state'. This function can be regarded as the amplitude of a well defined probability distribution (normalized to one) of one particle in all configurations. The wavefunction is defined in an infinitely dimensional *Hilbert space*  $\mathcal{H}$  of all possible states. This space is characterized by a set of mathematical restrictions (complete *vector space* with a scalar-product), which are needed for a consistent description in this theory. Each particle is represented by a vector  $|\psi\rangle$  which is constructed by a basis set  $|\psi\rangle = \sum_n c_n |\phi_n\rangle$ .<sup>1</sup> Several postulates build the basis for the quantum mechanical description of physics [10]:

1. At  $t_0$  the state of a physical system is given by  $|\psi(t_0)\rangle$  being part of the space  $\mathcal{H}$ .
2. Every measurable physical quantity is described by an operator  $\mathcal{A}$  acting in  $\mathcal{H}$  called *observable*.
3. The result of a measurement of  $\mathcal{A}$  can only give one of its *eigenvalues*  $a_n$ . The *eigenstates* form a basis set.<sup>2</sup>
4. The probability to find the system  $|\psi\rangle$  in the state  $|\phi\rangle$  is  $P = |\langle\phi|\psi\rangle|^2$ .
5. After a measurement of  $\mathcal{A}$  the system will be immediately in the *eigenstate*  $|e_n\rangle$  corresponding to the measured eigenvalue  $a_n$ .

---

<sup>1</sup>This short description is restricted on the case of a discrete basis set.

<sup>2</sup>I consider only non-degenerate *eigenvalues*. If there is more than one *eigenvalue* corresponding to an eigenvector one has to expand  $a_n \rightarrow \sum_i a_n^i$ .

6. The time evolution of a system is given by the *Schrödinger equation*.

$$H(t)|\psi(t)\rangle = i\hbar \frac{d}{dt}|\psi(t)\rangle \quad \text{Time dependent Schrödinger equation} \quad (2.1)$$

The fifth postulate describes the measurement of an experimentalist. Even though the state, e.g. the position of an electron is described by a wavefunction, once a measurement is performed this probability distribution ‘collapses’ and indeed the electron is only in one specific state, the eigenstate to the measured operator.

The observables correspond to a certain symmetry, i.e. they leave the system unchanged with time. The *eigenvalues* of the observables are often called ‘good’ quantum numbers as they characterize the state of a system. The set of quantum numbers changes depending on which interactions one takes into account. In atoms, the solution of the *Schrödinger equation* leads to several quantum numbers for the electronic states: The *principal quantum number*  $n$ , the *angular momentum*  $l$ , the *magnetic quantum number*  $m_l$ , and the *spin*  $s$ . *Spin-orbit interaction* leads to a different set, as the chosen basis does not fit the problem anymore.

In atoms, we find rotational symmetry around the nucleus. In a molecule this symmetry is broken, as we have more than one nucleus. The norm of the angular momentum is not conserved and  $l$  is no ‘good’ quantum number anymore. Instead, the intermolecular axis of a linear molecule defines a new symmetry axis  $\vec{z}$ , and the projections on this axis are new quantum numbers.

In order to describe the electronic states in a molecule a method has been established which approximates the observed energies. In the *Linear Combination of Atomic Orbitals (LCAO)* formalism, molecular electronic states are calculated by combining the orbitals obtained from the calculations for each single atom. The labels for molecular orbitals are listed in Table 2.1 [13, 3].

**Table 2.1:** Quantum numbers characterizing a molecular orbital of a diatomic molecule

$\lambda$	The projection of the orbital angular momentum on the internuclear axis $\lambda = 0, 1, 2, \dots \equiv \sigma, \pi, \delta \dots$
$N$	Label for the symmetry i.e. $1\sigma, 2\sigma, \dots$
$\mathbf{g} \setminus \mathbf{u}$	Point symmetry of the wavefunction to the center of charge (homonuclear molecules only)

Example for orbital notation:  $1\sigma_g^2$

The superscript number indicates the amount of electrons in this state. In the literature, sometimes, the symmetry label is replaced by the principal quantum number of the atomic orbital from which the molecular state is derived.

The total electronic configuration of a molecule can be described by summing over partially occupied orbitals, as closed shells cancel each other out. The notation of a molecular orbital configuration is shown in Table 2.2 [3].

As a molecule consists of at least two nuclei, their motion adds additional structure to the spectra obtained in experiments with molecules. Vibration and rotation of the nuclei create new substructure to electronic transitions. The energy of transitions between different vibrational levels is significantly smaller than between electronic states and structure from rotations is again on a much smaller scale than vibrations (see Sec. 2.2.4). Therefore, pure transitions between only vibrational or rotational levels are rare and one often talks about *vibronic transitions*, mixing the words electronic and vibrational.

**Table 2.2:** Quantum numbers characterizing the electronic state of a molecule

<b>X</b>	Energy label $X = 1, 2, 3, \dots \equiv X = A, B, C, \dots$
<b><math>\Lambda</math></b>	Total angular momentum around the internuclear axis $\Lambda = \sum_i \lambda_i$ with $\Lambda = 0, 1, 2, \dots \equiv \Sigma, \Pi, \Delta, \dots$
<b>S</b>	Sum of spins $S = \sum_i m_{s,i}$
<b>g \ \ u</b>	Point symmetry of the wavefunction to the center of charge
<b>+ \ -</b>	Symmetry to a plane through $\vec{z}$

The notation has the form:  $X^{2S+1}\Lambda_{g/u}^{+/-}$

The superscript preceding  $\Lambda$  indicates the multiplicity. It is equal to  $2 \cdot S + 1$  where  $S = \sum_i m_{s,i}$ .

Even though the exact calculation of the molecular energy taking into account vibrations and rotations is not possible, the exact solution can be approximated through some considerations. For small displacement  $x$  of the nuclei, the coulomb potential  $V(x)$  can be expanded. Neglecting terms higher than second order, the *harmonic potential* is obtained. As for any bounded potential, the eigenstates lead to a quantization of energies, in this case called vibrational numbers  $v$ . A more precise method consists of using the *Morse potential* which leads to the introduction of an *anharmonicity constant*  $\chi_e$ .

The simplest model of rotation, the rigid rotator, is shown in Sec. 2.2.4. If centrifugal distortion is considered, again limiting the model on small displacements, the energy is reduced by a quadratic term with the *centrifugal distortion constant*  $D_v$ . Combining these solutions, the energy of a vibrating and rotating diatomic molecule depending on the vibrational number  $v$  and the rotation number  $J$  reads [3]:

$$E(v, J) = \underbrace{\left(v + \frac{1}{2}\right)\hbar\omega}_{\text{harmonic vibr.}} - \underbrace{\left(v + \frac{1}{2}\right)^2\hbar\omega\chi_e}_{\text{unharmonic vibr.}} + \dots + \underbrace{hcB_vJ(J+1)}_{\text{rigid rot.}} - \underbrace{hcD_vJ^2(J+1)^2}_{\text{centrifugal dist.}} + \dots$$

The indices at the rotational constants  $B_v$  and  $D_v$  indicate their dependence on the vibration number  $v$ .  $\hbar = h/2\pi$  is the Planck constant,  $c$  the speed of light and  $\omega$  is the vibrational frequency depending on the force constant of the vibration and the masses of the moved atoms.

## 2.2 Approximations in atomic physics

Even the simplest molecule, the  $H_2^+$  ion consists of three particles. Therefore, the Schrödinger equation of a molecule cannot be solved analytically. Meanwhile, simplification of the problem can lead to results in good agreement with experimental observations. For vibrations and rotations a simplified description has been shown earlier in the text. The most important approximations are described in the following sections.

### 2.2.1 Born-Oppenheimer approximation

In order to calculate the energy of an electron in a molecular potential, one of the most important approximations was introduced by Born and Oppenheimer in the 1920s.

The nucleus in an atom is more than 1000 times heavier than the electrons around it. Born and Oppenheimer argued that the inertia of the electrons can be neglected in comparison to the nucleus. In other words, the fast electrons see the nuclei as almost

stationary. Therefore, we can split the wavefunction into a nuclear part (depending on the positions of the nuclei  $\mathbf{R}_i$ ) and an electronic part depending only on the distance of the electrons to the nuclei  $r_i$ . The positions of the  $\mathbf{R}_i$  are a constant parameter. The electronic part can then be calculated independently for different nuclear arrangements, and we combine them with the solution of the nuclear part afterwards.

$$\boxed{\psi_{mol}(r_i, R_i) = \psi_{elec}(r_i, \mathbf{R}_i) \times \psi_{nucl}(R_i)} \quad B.-O. \text{ approximation} \quad (2.2)$$

The solution allows us to construct potential energy curves displaying the energy versus the internuclear distance (see Fig. 5.9). The *Born-Oppenheimer approximation* is a very successful technique. Even in cases it fails to immediately give a good result, it is still used as a starting point, followed by corrections from electron-nucleon interaction.

### 2.2.2 Dipole approximation

The electromagnetic field of photon radiation can be described by plane waves with wave vectors  $k$ . At typical energies of photoionization or emission the wavelength of the field is much longer than the atomic radius. For small  $x = \mathbf{k} \cdot \mathbf{r}$  we can therefore expand the plane wave in a Taylor series:

$$e^{-ix} \approx 1 - ix + \dots \quad \text{for} \quad \lim_{x \rightarrow 0} e^{-ix} = 1$$

This 0<sup>th</sup>-order approximation called *dipole approximation* can be used if the wavelength of the electromagnetic field is long enough.<sup>3</sup> The *Transition dipole moment* gives the probability for an electronic transition between two states  $\Psi_e$  and  $\Psi_e'$ :

$$\boxed{P_M = \int \Psi_e'^* \boldsymbol{\mu}_e \Psi_e d\tau} \quad \text{Transition dipole moment} \quad (2.3)$$

The exact value is usually not interesting but instead one derives a general *orbital selection rule* for the transitions resulting in so called *forbidden transitions* with very low probability. Neglecting the spin part and using the above described approximations, we can summarize for the probability of a *vibronic transition*:

$$\begin{aligned} P &= \langle \Psi_v' \Psi_e' | \boldsymbol{\mu} | \Psi_v \Psi_e \rangle \\ &= \langle \Psi_v' \Psi_e' | \boldsymbol{\mu}_e | \Psi_v \Psi_e \rangle \\ &= \underbrace{\langle \Psi_v' | \Psi_v \rangle}_{P_{FC}} \underbrace{\langle \Psi_e' | \boldsymbol{\mu}_e | \Psi_e \rangle}_{P_M} \end{aligned}$$

The total *dipole operator* is  $\boldsymbol{\mu} = \boldsymbol{\mu}_e + \boldsymbol{\mu}_n$  but the nuclear part vanishes as  $\langle \Psi_e' | \Psi_e \rangle = 0$ . The Franck-Condon factor  $P_{FC}$  is described in the following.

### 2.2.3 Franck-Condon principle

The *Franck-Condon principle* is a semi-classical approximation, explaining the intensity of photoemission and absorption. It is based on the assumption that an electronic transition will occur much faster than nuclear motion, keeping the nuclear coordinates constant

<sup>3</sup>Non-dipole effects become important at high photon energies in the *keV* range.

during the process. In a picture showing graphs of the potential in dependence of the internuclear distance, the transition is drawn in the form of a vertical line between the states (*vertical transition*). The probability of a transition between two states is higher the more overlap the vibrational wavefunctions of the states have. In the quantum-mechanical description using operators (matrices) there is a matrix element representing each transition and its value quantifies the overlap. The principle also relies on the assumption of a possible separation of electron- and molecular wavefunction  $\Psi_v$  and  $\Psi_e$  (*Born-Oppenheimer approximation*). The total wavefunction can then be separated into  $\Psi_{\text{tot}} = \Psi_v \Psi_e \Psi_s$ , where  $\Psi_s$  is the spin part. The *Franck-Condon factor* describes the probability for the transition between the vibrational initial state  $\Psi_v$  and a final state  $\Psi'_v$ :

$$P_{FC} = \int \Psi'_v{}^* \Psi_v d\tau \quad \text{Franck-Condon factor} \quad (2.4)$$

However, the total *transition probability* is given by  $\langle \Psi_{\text{tot}}' | \mathcal{A} | \Psi_{\text{tot}} \rangle$  with  $\mathcal{A}$  as the operator containing all transitions, and the Franck-Condon factor is just one part, as demonstrated in Sec. 2.2.2. The contributions of selection rules can be much more important.

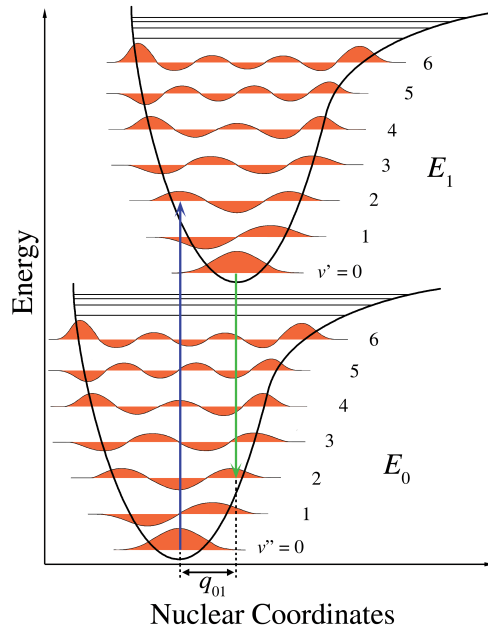


**Figure 2.1:** [51] In the Franck-Condon principle, an electronic transition occurs faster than the nuclear motion. The Probability of a transition at fixed distance  $q$  (*vertical transition*) depends on the overlap of the state functions involved.

### 2.2.4 Axial recoil approximation

In order to measure electron angular distribution in the molecular frame, we need to have information about the molecular axis at electron emission time. This information is obtained by detecting the recoil ions which are emitted in opposite directions after the breakup of the molecule. In this case, the momentum vector between the ions defines the molecular axis. Nevertheless, this is only true if we assume that the molecule remained in the same orientation in the laboratory, i.e. did not rotate significantly before we detect the fragments. This is called *axial recoil approximation*.

At low energies, we can regard a linear molecule as a *rigid rotator* around the center between its two ends. The *rotational energy* of a molecule in the rotational state  $J$  is then given by [13]:

$$E_{rot}(J) = \frac{J(J+1)\hbar^2}{2\mu \cdot R_e} \quad \text{Rotational energy} \quad (2.5)$$

Here  $\hbar$  is the Planck constant,  $R_e$  is the equilibrium distance of the outer atoms to the rotation center i.e. in the  $\text{CO}_2$  the length of the C–O bond. The reduced mass  $\mu$  is defined as:

$$\mu = \frac{m_1 \cdot m_2}{(m_1 + m_2)}$$

For  $J = 1$ , an equilibrium bond length of  $R_e = 2.2 \text{ bohr}$  [34] and with the weight of the oxygen atoms  $m_1 = m_2 = 16 \text{ amu}$ , we obtain an energy of  $0.84 \text{ meV}$ . The rotational energy can also be calculated by  $E_{rot} = B_e \cdot J(J+1)$  using experimentally measured rotational constants  $B_e$ . For  $\text{CO}_2$ , a measured value of  $B_e = 0.389 \text{ cm}^{-1}$  [5] delivers the same result. The rotational period can be obtained from:

$$T_{rot} = \frac{2\pi}{\hbar} \frac{\mu R_e^2}{\sqrt{J(J+1)}} \quad \text{Rotational period} \quad (2.6)$$

For  $J = 1$  the period is  $5.3 \cdot 10^{-12} \text{ s}$ . In comparison to that, photoabsorption and the subsequent transition of an electron to a higher orbital occur in the order of  $10^{-15} \text{ s}$  and  $10^{-16} \text{ s}$ , respectively. As the core-hole state decays in  $\sim 6\text{--}10 \cdot 10^{-15} \text{ s}$  [34, 30], the dissociation of the di-cation takes place fast enough, that no time is left for the molecule to perform significant rotation before dissociation. Later rotation of the ions after breakup can be neglected, as position changes do not affect the initial angle any more at long distance between the ions. I conclude that the *axial recoil approximation* holds for the dissociative states measured.

## 2.3 Photoionization

One of the observations leading to the break-through of the quantum description of Nature was the *photoelectric effect*. Experiments had shown that the energy of electrons emitted from a surface depends on the frequency  $\nu$ , or color of light. This did not comply with the classical theory by James C. Maxwell which predicted that the energy increases with the intensity of the light. In 1905, Albert Einstein explained the observation by describing light as quantized, only existing in energy partitions of  $E_\gamma = h \cdot \nu$ , the photons. The Planck constant  $h$  was later named after Max Planck who first introduced it in his theory of black body radiation. When light shines on a material, an electron absorbs one of these quanta and is emitted from the surface if the energy is higher than a certain value. This value is the binding energy in the material.

As in the photoelectric effect observed on surfaces, photoionization of a molecule is explained by the absorption of a photon by an electron, which is then emitted to the continuum. The kinetic energy of the electron is determined by the difference of photon energy  $E_\gamma$  and binding energy of the orbital. A photoelectron ejected from the  $K$ -shell has the energy  $E_{el}$ :

$$E_{el} = E_\gamma - E_k \quad \text{Photoelectron energy} \quad (2.7)$$

Above a certain threshold, the absorption of one photon can lead to emission of two electrons, which is called *double photoionization*. At ionization of valence electrons, coming from outer shells, two processes of double photoionization can be distinguished. The photoelectron ejected from the atom or molecule can interact directly with another electron (*Two-step one process*), or change the molecular potential. This sudden change in the potential leaves the second electron in an unbound state (*Shake-off process*).

At higher photon energies double ionization is dominated by the *Auger decay* described in the following section.<sup>4</sup>

### 2.3.1 Auger decay in the two-step model

Photoionization with ejection of a core level electron leaves the atom or molecule in a highly excited state. Subsequently, the inner shell vacancy will be filled up by an electron from a higher orbital. The excess energy will then be emitted either by radiation or by the emission of an additional electron leaving a valence or higher core orbital. This process of *double photoionization* is called *Auger decay*, named after one of its discoverers<sup>5</sup> P. V. Auger in 1925 [4] and is the dominant decay mechanism for core-ionized CO<sub>2</sub>.

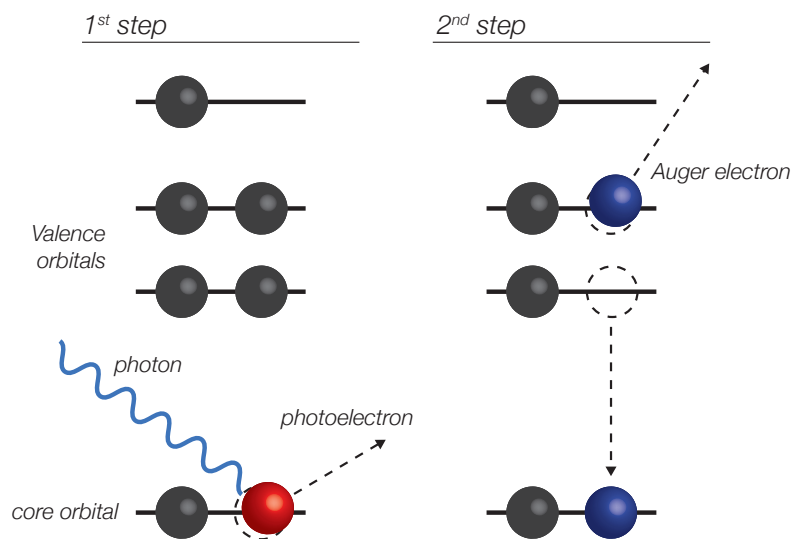


**Figure 2.2:** Schematic of the Auger decay mechanism. A photon ionizes an electron from the core level. The hole is filled up by an electron from a higher orbital while a valence electron is ejected from the atom, carrying the excess energy.

*Auger decay* is generally described as a two-step process in which the photoelectron leaves the molecule in an excited intermediate state which then decays in a second step via emission of the *Auger electron*. The theoretical description of the two-step model is based on the assumption that the absorption of the photon happens much faster than the Auger decay. The transition probability can then be described by separation into the

<sup>4</sup>It should be mentioned in the context of single photon absorption that a single electron can absorb multiple photons in high intensity laser fields.

<sup>5</sup>Lise Meitner described the effect already in a publication in 1922.

dipole transition from the ground state  $|\Psi_0\rangle$  to an intermediate state  $|\Psi_{im}\rangle$  and coulomb interaction of this state to the final state  $|\Psi_f\rangle$  [24, 16, 57]:

$$\langle\Psi_f|\boldsymbol{\mu}|\Psi_0\rangle = \langle\Psi_f|\mathbf{V}|\Psi_{im}\rangle \langle\Psi_{im}|\boldsymbol{\mu}|\Psi_0\rangle \quad \textit{Two-step model} \quad (2.8)$$

In this model, there is no dependence of the photoelectron on the Auger electron except for the projection of the orbital angular momentum of the intermediate state, which determines the angular momentum of the Auger electron.

The energy of the Auger electron  $E_{aug}$  can be calculated by:<sup>6</sup>

$$E_{aug} = E_k - (E_{im} - E_f) \quad \textit{Auger electron energy} \quad (2.9)$$

## 2.4 The carbon dioxide molecule

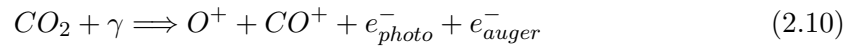
Carbon dioxide molecules consist of two oxygen atoms and one carbon atom in the middle. In relaxed geometry, the oxygen atoms are in line with the carbon, each at an equilibrium distance of 2.2 *bohr* [34] to the carbon. The geometry allows four different *vibrational modes* that can be excited (see Fig. 2.3). In asymmetric stretching, the carbon atom bounces between the oxygen atoms, shortening the C–O bond on one side and making it longer on the other. Symmetric stretch changes the C–O bond length on both sides equally. The two stretching modes conserve the linear geometry whereas the bending modes break this symmetry. In this vibration, the carbon atom leaves the linear axis between the oxygen atom perpendicularly. The bending can take place in two directions (d. horizontal and c. vertical bending), meanwhile, these two modes are energetically degenerated.

In the ground state the 16 electrons of the molecule occupy the following orbitals [12] (for notation description look in Table 2.1):

$$1\sigma_g^2 1\sigma_u^2 2\sigma_g^2 3\sigma_g^2 2\sigma_u^2 4\sigma_g^2 3\sigma_u^2 1\pi_u^4 1\pi_g^4 ({}^1\Sigma_g); 2\pi_u^0 5\sigma_g^0 4\sigma_u^0 \quad \textit{CO}_2 \textit{ ground state}$$

The  $2\sigma_g$  orbital is the carbon  $1s$  and the lowest unoccupied orbital is  $2\pi_u$ .

The *ionization threshold* for the C  $1s$  orbital lies at  $297.63 \pm 0.01$  eV [39]. At 312 eV, a *shape resonance* is located where intensity of photoelectron emission is enhanced. Usually, this is attributed to a temporary trapping of the photoelectron in the molecular potential or to the temporary transition of a  $1s$  electron to a valence-like orbital [12, 38]. The main dissociation channel after ejection of a core electron is the breakup of the  $\text{CO}_2^{++}$  into one oxygen and one  $\text{CO}^+$  ion:



There is also the possibility of a three-body breakup with one neutral atom, and there are several quasi-stable states of the  $\text{CO}_2^{++}$  with a lifetime of several  $\mu\text{s}$ , which sometimes do not dissociate before detection on the detectors (see Fig. 5.1).

## 2.5 Experiments on $K$ -shell photoionization of $\text{CO}_2$

In the past, carbon dioxide has been the subject of many single and double ionization experiments. Doubly charged  $\text{CO}_2^{++}$  ions were first observed in 1964. Since then, different

<sup>6</sup>The energy of electronic states in this work is set positive.

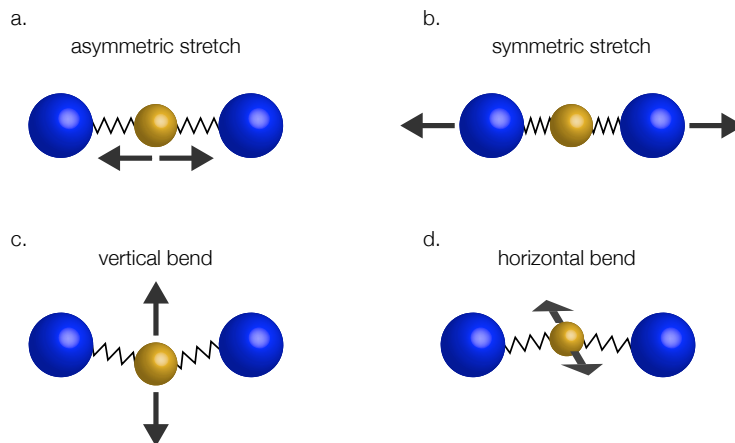


**Figure 2.3:** Figure of the  $\text{CO}_2$  molecule and its different vibrational modes: a. Asymmetric stretch - the carbon moves between the oxygen atoms; b. Symmetric stretch - lengths of the C–O bonds change equally on each side; c. and d. Bending modes of the C–O bonds in horizontal or vertical direction

methods have been applied to investigate decay mechanisms and the energetic structure [49].

Moddeman *et al.* [35] first investigated the Auger spectrum in the 1970s, although, at that time, the identification of vibrational structure was not yet possible. In the 1980s, theoretical results were used to analyze those spectra [1]. Hochlaf *et al.* [18] did calculations on the lowest states of the di-cation in the 1990s, and in 1995 Schmidbauer *et al.* [43] performed experiments with electron spectroscopy measuring partial cross sections and angular distributions near the C(1s) photoionization threshold. They could specify satellite states produced from conjugate shake-up<sup>7</sup>, but also fine structure which they attributed to multielectron excitations, suggesting that a one-electron description might not be sufficient in these regions. De Fanis *et al.* [11, 12] underlined this assumption with an experiment using the COLTRIMS technique. They were able to separate different mechanisms by selecting several angles between the polarization and the molecular axis and showed that interaction of photoelectrons with valence electrons (*PEVE*) shifts the energies obtained from single particle calculations. They attributed a broad resonance at 312 eV to this effect.

Caroll *et al.*[9] measured the lifetime of the core ionized  $\text{CO}_2$  with high precision and found longer lifetimes than predicted, raising the question of whether valence electrons from the oxygen atoms might play a role in Auger decay after the ionization of a carbon core electron. Hatherly *et al.* [17] used threshold electron spectroscopy to look at dynamics of the C(1s) satellites. In recent years Eland *et al.* [14] and Slattery *et al.* [50] performed different photoelectron coincidence spectroscopy experiments focusing on quasi-stable states. Partial cross sections and asymmetry parameters for  $K$ -shell photoionization were recently measured with high precision by Hoshino *et al.* [19], and in 2008, Püttner *et al.* investigated the Auger spectrum after carbon core-electron ionization in vibrationally

<sup>7</sup>In the *conjugate shake-up* process the photon transfers its angular momentum to a core electron which is promoted to a higher molecular orbital (dipole excitation), and a valence electron is emitted in monopole ionization. In *direct shake-up* dipole ionization of a core electron is followed by a monopole excitation of a valence electron.[12]

resolved measurements.

However, a recent experiment from Liu *et al.* [30] showed a new insight into angular distributions of the photoelectron which had not been observed in results reported by De Fanis in 2002 [11]. Liu *et al.* reported an asymmetry of the molecular frame photoelectron angular distribution (*MFPAD*) at energies of 312, which corresponds to a shape resonance of the C *K*-shell, and at 320 eV. This was very surprising as it was commonly assumed that the angular distribution of the carbon core electrons would be symmetric. The orbital has spherical symmetry and scattering in the linearly distributed molecule with equal distance to the oxygen atoms should be symmetric to the molecular axis. The authors attribute the effect to the interference of gerade and ungerade intermediate states populated after the first ionization step and suggest this as evidence for a breakdown of the usually applied *two-step model* (see 2.3.1). This interesting effect motivated us to perform a measurement of carbon *K*-shell photoionisation with subsequent Auger decay. We were interested in the angular distributions of the Auger electrons and whether they would show similar asymmetric effects.

## 3 Experimental Setup

In this experiment, CO<sub>2</sub> molecules were ionized at photon energies of 303–322.5 eV. After ejection of a C(1s) photoelectron and subsequent Auger electron emission, the molecules fragmented mainly into O<sup>+</sup> and CO<sup>+</sup> ions.

In order to detect the particles emerging from the reaction, *COLd Target Recoil Ion Momentum Spectroscopy (COLTRIMS)* was applied. By coincidence measurement of the positions and the *times-of-flight (TOF)* of the ions and electrons on separate detectors, it was possible to reconstruct the initial momenta of the particles.

In the present case, the high energy of the Auger electron inhibited the measurement of both electrons on the electron detector with acceptable resolution. In order to address this problem, a basic physical principle was applied: as a closed system, all four particles together have to fulfill momentum conservation.

$$\sum_i \vec{p}_i = 0 \quad \text{Momentum conservation}$$

Hence, measuring three of them, allows one to derive the fourth particle (see Equ. 4.15). However, a look at the actual momenta of the particles reveals the challenge in the measurement: as an electron is more than ten thousand times lighter than the fragment ions, the kick of the Auger electron on the center of mass of the particles is very small. In our reaction, the Auger electron had a momentum of  $\sim 5$  a.u. in comparison to ion momenta from coulomb explosion of  $\sim 90$  atomic units. Therefore, the momenta of the ions had to be measured with very high precision.

In order to obtain a sufficient resolution on the center of mass, a large part of the ion solid angle was sacrificed. An *electrostatic lens* was built into the spectrometer, compensating for the target uncertainty in the directions perpendicular to the time-of-flight direction. The lens, *time-focusing geometry* and a small electric field, narrowed the detection acceptance of the ions to an angle of  $\pm 21^\circ$  with respect to the spectrometer axis. All orientations of the electrons to the molecular axis were obtained, as the photoelectrons were measured with full  $4\pi$  angle. The spectrometer design is discussed in Sec. 3.3.

CO<sub>2</sub> molecules in a gas at room temperature have a thermal momentum spread in the order of the Auger momentum transfers. A description how this problem is addressed together with the properties of the gas target can be found in Sec. 3.2.

The intense light was produced in a synchrotron (see Sec. 3.5). The photon beam crossed the gas jet at a  $90^\circ$  angle in a vacuum chamber. Perpendicular to both axes, a static electric field and a magnetic field guided the photoelectrons and ions on *Multi-channel plates (MCP)* with *delay-line anodes* (see Sec. 3.4) providing time and position measurement on each side of the spectrometer. On page 22 a schematic of the principal parts is shown.

### 3.1 Vacuum system

In order to perform photoionization measurements, a high-vacuum environment is needed. Without sufficient vacuum, the interaction of the photon beam with the background gas would make it impossible to attribute detected particles to reactions from the target.

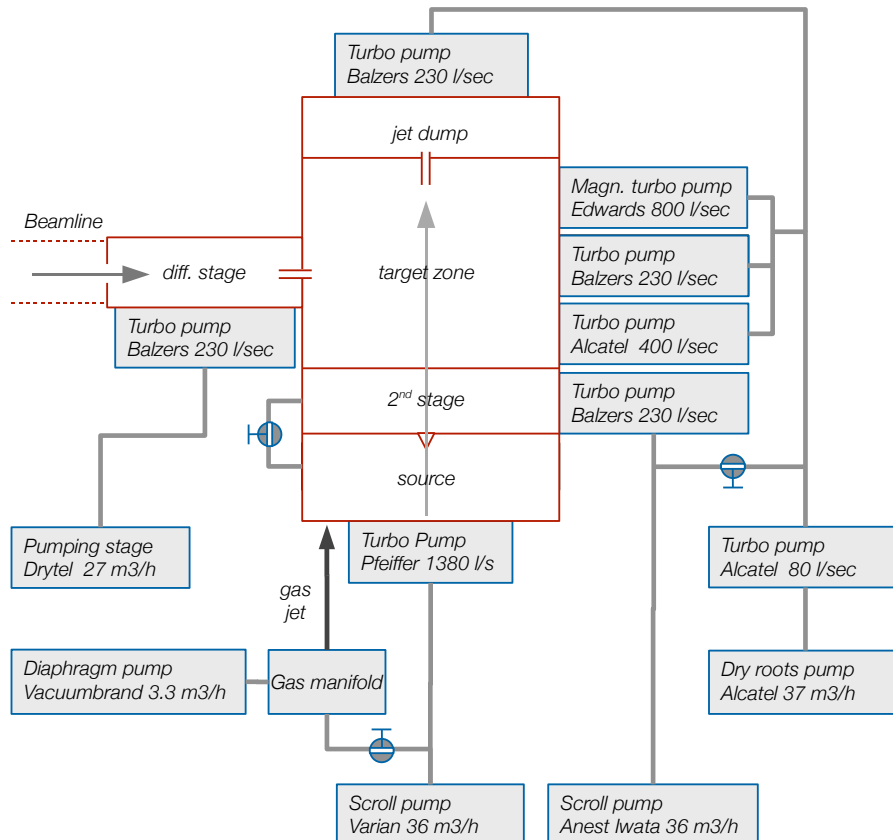


**Figure 3.1:** Schematic of the vacuum system of the experimental chamber. The chamber itself is separated into four zones, each directly connected to turbo pumps. The backing pressure is supplied by several scroll and roots pumps. Between the beamline and the chamber, a differential pumping stage bridges between the vacuum in the target zone ( $10^{-8}$  Torr) and the ultra-high vacuum in the beamline ( $< 10^{-10}$  Torr). For operation vacuum pressures see Table 3.1.

The vacuum system is separated into four different regions (see Fig. 3.1). The first stage contains the nozzle where the gas jet is injected into the system. The high gas load is pumped by a turbo pump with high throughput. A bypass to the second stage is needed for pumping down and venting. It can be closed leaving only the narrow skimmer (0.3 mm) as a connection between these regions. The second stage and the target zone are connected by a small pinhole of 0.5 mm diameter and another bypass which is connected to the backing pumps. The biggest part of the chamber, containing the reaction zone, is extended by a long arm housing the ion drift tube. Because of its large volume, the main chamber is connected to three turbo pumps. The jet dump, a long metal cylinder equipped with a turbo pump, collects the gas jet after crossing the spectrometer. Its small opening allows the gas jet to pass, but inhibits back flow into the reaction zone. The alignment of the jet can be controlled by the pressure rise in the jet dump (see Appendix 2). A differential pumping stage is mounted between the target zone and the beamline in order to bridge the ultra high vacuum of the beam line of about  $10^{-10}$  Torr and jet operation pressures of up to  $10^{-8}$  Torr in the chamber. We achieved the necessary vacuum in the differential stage by using a narrow cylinder of about 10 cm length as the only connection to the chamber, as well as a turbo pump and an additional aperture to the beamline. The backing pressure for the turbo pumps was provided by several scroll and diaphragm pumps. Usual vacuum pressures in the system are shown in Table 3.1.

**Table 3.1:** Operation pressures [Torr]

Jet pressure [psi]	0	10
jet dump	$1 \cdot 10^{-8}$	$3 \cdot 10^{-8}$
Target zone	$2 \cdot 10^{-8}$	$2 \cdot 10^{-8}$
Second stage	$7 \cdot 10^{-8}$	$6 \cdot 10^{-7}$
Jet source	$1 \cdot 10^{-6}$	$1 \cdot 10^{-4}$

## 3.2 Target

A major problem for measuring atomic and molecular reactions is created by the movement of the particles in a gas at standard temperatures.

For an *ideal gas* molecule at a given Temperature  $T_0$  the internal energy can be derived from the *Boltzmann distribution*. Each degree of freedom  $f$  for translation, rotation and vibration attributes with  $0.5 \cdot k_B T_0$  to the internal energy:

$$E = (f_{tr} + f_{rot} + f_{vib}) \cdot \frac{1}{2} k_B T_0 \quad \text{Internal energy} \quad (3.1)$$

where  $k_B$  is the Boltzmann constant. We can calculate the momentum of a particle with mass  $m$  from the kinetic energy in one direction:

$$p_i = \sqrt{m k_B T_0} \quad \text{Thermal momentum} \quad (3.2)$$

For a CO<sub>2</sub> molecule with a mass of 44 amu at room temperature of  $T_0 = 296$  K, a value of 8.70 a.u. is obtained. This movement from thermal energy is more than the recoil of the Auger electron on the center of mass. Hence, it is crucial the experiment to reduce the energy of the molecules.

One can reduce the internal energy by cooling the nozzle through which the gas flows. In the case of CO<sub>2</sub>, this was not possible for two reasons: firstly because CO<sub>2</sub> already freezes

at a temperature of 78.5° C and the risk of clogging the nozzle would be high. Secondly, it tends to build clusters of several molecules, which would decrease the resolution of the Auger electron. In the breakup of a (CO<sub>2</sub>)<sub>2</sub> dimer into CO<sup>+</sup>, O<sup>+</sup> and a neutral CO<sub>2</sub>, the neutral molecule would carry a varying amount of the Auger momentum, significantly decreasing the momentum resolution.

Another important issue is providing a small target. The width of the target crossed by the photon beam will create uncertainty of measurement which should be reduced as much as possible.

In this experimental setup, a narrow target and low internal energy is achieved by creating a *supersonic gas expansion*. In a sufficient vacuum environment, gas flowing from a vessel at pressure  $p_a$  to a second vessel at pressure  $p_b$  will expand isentropically if the condition  $p_a > 2.1 \cdot p_b$  is fulfilled [33]. During the expansion, the whole enthalpy, the internal energy as well as the energy transferred from the pressure at the nozzle, is converted into a directed motion of the particles. This happens by a successive transfer of energy between the particles to the translation direction. Finally, an interaction free zone called *zone of silence* builds up where the particles move at supersonic velocity. By cutting out a part of the gas from this region, we obtain a focused jet.

We can now try to estimate the specifications of the supersonic gas jet. Meanwhile, one has to consider that molecular beams are more complex than simple atomic models and that approximations like the one of an *ideal gas* might not always give accurate results.

If we take into account that the expansion only cools the jet to a finite value, the target temperature  $T_{jet}$  can be approximated by [21, 33]:

$$\boxed{T_{Jet} \simeq \left(\frac{f}{2} + 1\right) \frac{T_0}{S^2}} \quad \text{Supersonic jet temperature} \quad (3.3)$$

$T_0$  is the temperature of the nozzle and  $S$  is the *Speed ratio*. In addition to the factor  $f/2$  from the internal energy, the pressure adds another factor of 1, derived from the gas equation  $pV = nk_B T$ . A higher pressure does not raise the temperature, as the particle number  $n$  rises equally.

The jet velocity  $v$  can be obtained from Equ. 3.1 [21]:

$$\boxed{v_{jet} = \sqrt{\left(\frac{f}{2} + 1\right) \frac{k_B}{m} \cdot (T_0 - T_{jet})}} \quad \text{Jet velocity} \quad (3.4)$$

The speed ratio is given by the ratio of the jet speed of particles of mass  $m$  to their velocity spread. In order to estimate the speed ratio of our apparatus, a formula generated from experimental data is applied [8].<sup>1</sup>

$$\boxed{S_{||} = 5.4(P_0 d)^{0.32}} \quad \text{Speed ratio (molec. beams)} \quad (3.5)$$

Here  $P_0 d$  is the product of applied gas pressure and the nozzle diameter in [Torr · cm]. Equation 3.5 can only give an estimate for the actual speed ratio of the CO<sub>2</sub> jet. In gases like CO<sub>2</sub> and H<sub>2</sub>, vibrational and rotational excitations change the relaxation dynamics.

<sup>1</sup>The formula is derived for molecules with less activity of vibrational modes like N<sub>2</sub> or CH<sub>4</sub> for which the authors claim to approach actual values by 10 %.

The internal temperature of the gas jet differs between the jet direction and the directions perpendicular to the jet. In the latter, the temperature is reduced by the geometry, which inhibits particles with large transversal momentum from reaching the target zone.

With the distances of the geometry, the speed ratio and the expected thermal momentum spread, the momenta of the molecules in the jet can be calculated.

$$p_{\perp} = \sqrt{f m k_B T_0} \cdot \frac{(d_n + d_p)}{l_p} \quad \text{Jet momentum transversal} \quad (3.6)$$

$$p_{\parallel} = \sqrt{f m k_B T_0} \cdot \left(2\sqrt{\ln(2)}\right) \frac{1}{S} \quad \text{Jet momentum parallel} \quad (3.7)$$

Here,  $l_p$  its distance to the nozzle,  $d_n$  is the diameter of the gas nozzle, and  $d_p$  is the diameter of the pinhole defining the final jet size.

If the jet is adjusted carefully, almost the whole gas flow will reach the jet dump. Target density can then be estimated from the pressure rising in the jet dump [21, 56].

$$\rho = \frac{N_A}{22.4} \cdot \frac{\Delta p_d L_d}{v_{jet} \cdot \frac{\pi}{4} d_t^2} \quad \text{Target density} \quad (3.8)$$

$N_A$  is Avogadro's constant,  $\Delta p_d[\text{bar}]$  and  $L_d[\text{ls}^{-1}]$  the pressure rise and the pumping power in the jet dump.<sup>2</sup>

In Fig. 3.2, a schematic of the gas expansion system is shown. The gas was injected in the source by a nozzle of 30  $\mu\text{m}$  diameter. A narrow, precisely machined cylinder called *skimmer* (0.3 mm diameter) cut out a directed part of the gas from the zone of silence (blue oval area in Fig. 3.2). An additional pinhole of  $\sim 0.5$  mm defined the final jet diameter in the reaction zone of  $\sim 1.7$  mm, where it was crossed by the photon beam.

The mass of  $\text{CO}_2$  is 44 *amu* and there are 3 translational, 2 rotational and 3 vibrational degrees of freedom (see Fig. 2.3).<sup>3</sup> Equation 3.5 leads to a value of 6.2 for the terminal speed ratio. Inserting the speed ratio and the geometry values in Equ. 3.7 and 3.6 we obtain  $p_{\parallel} = 6.57$  *a.u.* and  $p_{\perp} = 0.36$  *a.u.*. The momentum uncertainty in the z-direction does not match the observed value of  $\sim 3.8$  *a.u.* (see Fig. 4.10). A value of 10–11 produces better results and both sets of values are shown in Table 3.2. In the TOF direction, the focus of the photon beam was smaller than the jet size (see Sec. 3.5.1). Therefore, the molecules had a reduced momentum spread from thermal energy according to the overlap with the photon beam. The focus size was estimated to be  $\sim 160$   $\mu\text{m}$ , which results in an improvement by a factor of 10 in TOF direction. An approximate target diameter of  $d_t = 1.7$  mm and a rise in the jet dump of  $\Delta p_D = 2.4 \cdot 10^{-8}$  Torr at 230 l/s pumping speed lead to the results shown in Table 3.2. More detailed informations on molecular beams and supersonic gas jets can be found in an article from D. Miller [33] and in a book from H. Pauly [36].

<sup>2</sup>The units  $(\text{l} \cdot \text{bar} \cdot \text{s})^{-1}$  are left out in the formula

<sup>3</sup>The two bending modes of  $\text{CO}_2$  show point symmetry and are therefore degenerated.

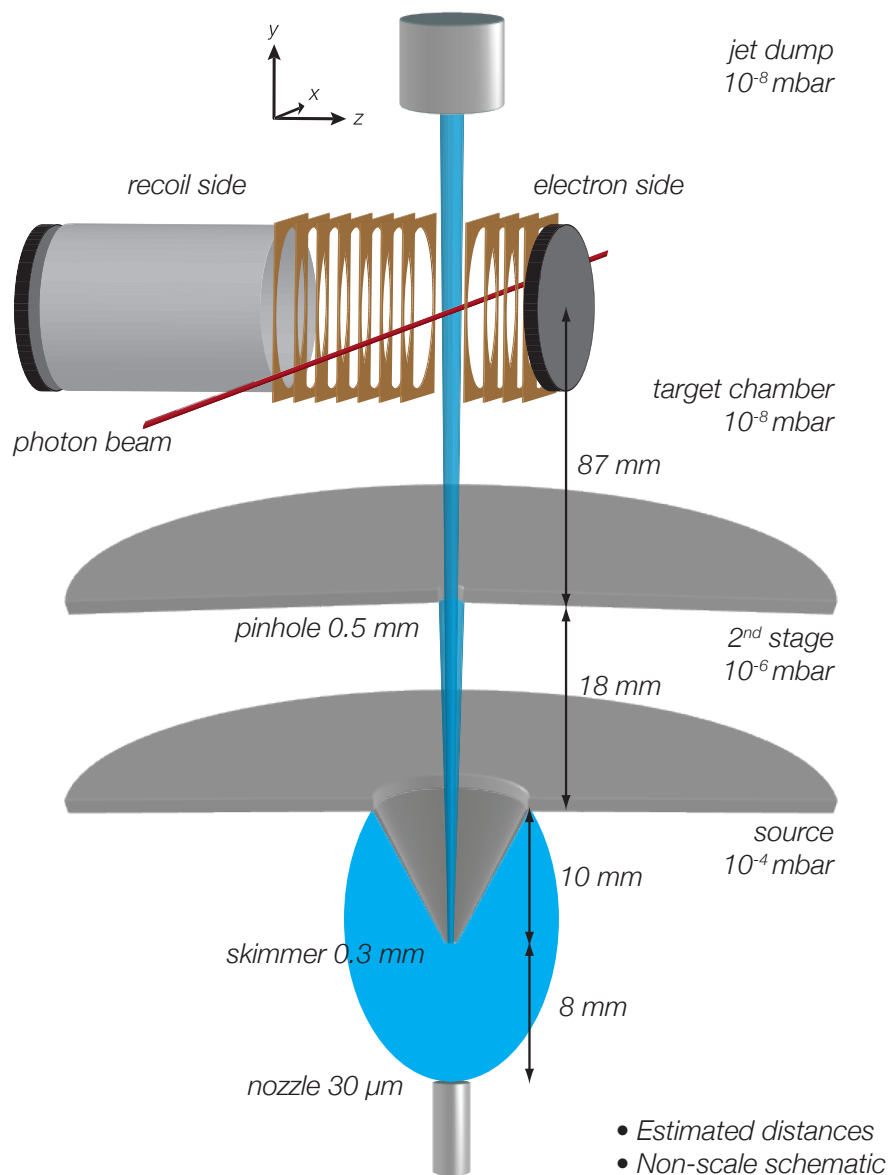


**Figure 3.2:** Schematic drawing of the setup inside the experimental chamber. The gas flows through a nozzle in the 1<sup>st</sup> stage. The skimmer cuts out a narrow supersonic jet from the *zone of silence*. In a 2<sup>nd</sup> stage it passes a pinhole which again cuts out a part and inhibits background gas from flowing into the target chamber. In the reaction zone inside the spectrometer, the gas jet is crossed perpendicularly by the photon beam and is pumped out subsequently in the jet dump.

**Table 3.2:** Jet properties for  $\text{CO}_2$  at  $T_0 = 296\text{K}$ . The values in the first column are obtained from a speed ratio of 10.8, which was estimated from the resulting momentum spread. The values in parentheses are calculated with the empiric formula (Equ. 3.5) for molecular beams.

$p_{jet}$		10	$psi$
$S$	Speed ratio	10.8	(6.2)
$v_{jet}$	Speed	517	(493) $ms^{-1}$
$T_{jet}$	Temperature	12.7	(38.3) $K$
$\rho$	Target density		$1.7 \cdot 10^{11} \text{ cm}^{-3}$
$p_{beam}$	$x$ -momentum spread	0.36	(0.36) $a.u.$
$p_{jet}$	$y$ -momentum spread	3.78	(6.57) $a.u.$
$p_{TOF}$	$z$ -momentum spread	0.04	(0.04) $a.u.$

### 3.3 Spectrometer

The *spectrometer* is a central part of a COLTRIMS experiment, creating the electric field which guides the ions and electrons to the detectors. The reaction zone is located inside the spectrometer where the photon beam hits the gas jet of  $\text{CO}_2$  molecules (see Fig. 3.2 and 3.4). The electric field, directs the positively charged ions to the recoil ion detector, whereas the low energetic electrons are captured by a homogeneous magnetic field and fly on spiral trajectories to the electron detector in the opposite direction.

It was crucial for the success of this experiment to achieve a high resolution of the ion momenta. The electric field principally defines the resolution that can be obtained. Lowering the electric field leads to a larger spread in time-of-flight and higher resolution, but one loses solid angle linearly, because ions with large transversal momentum will miss the detector. Meanwhile, the photoelectrons have to be detected with full solid angle, so the field has to be strong enough to turn around electrons that start in the direction of the ion detector. In order to be able to measure the small momentum transfer of the Auger electrons on the recoil ions, we applied a low electric field (15.3 V/cm) and used a three dimensional focusing geometry, consisting of an *electrostatic lens* in the ion acceleration region and a field free drift region.

On the electron side, a homogeneous electric field accelerated the electrons until they reached a field free drift region, which was built about twice as long as the acceleration region. In this geometry, particles starting from different distances in the target zone will hit the detector at the same time, reducing in this way uncertainty of the target position in TOF direction. The fraction of drift region to acceleration region of  $\sim 2:1$  is called *time focusing* or *Wiley-McLaren geometry*. On the recoil side, the field step created by the electrostatic lens increased the acceleration of the ions and shifted the actual time focussing point. In order to obtain time focusing, the drift length had to be extended, which resulted in an especially long recoil side of the spectrometer.

#### 3.3.1 Electrostatic lens

In order to reduce the momentum uncertainty from the target extension in the detector directions (perpendicular to the TOF), we added an *electrostatic lens* to the recoil ion side.

In the same way as an optical lens can focus light from different positions onto one single point, an electrostatic lens can focus ions starting from different positions in the

interaction zone to one position on the detector. The idea is technically realized by creating an inhomogeneous electric field whose potential lines are bent convexly like the shape of an optical focusing lens. The ions flying through the lens cross these lines orthogonally which results in a bent trajectory. This method reduces the degrading influence of the jet size in the interaction zone significantly, approximately by a factor of 5–6 [46].

Figure 3.3 shows a simulation of the ion trajectories in the setup. It is important that the recoil ion detector is positioned at the focal point of the lens. The strength of the lens and the length of the recoil acceleration and drift regions have to be adjusted until the foci of time and space focusing match. For ideal focusing abilities, the lens would be positioned in the reaction zone. This is not possible, because momenta from electrons flying in the field of the lens could not be reconstructed any more. The strength of the electric field defines how far the photoelectrons will fly in the recoil direction before they turn around, and the lens cannot be positioned closer than this point. The distortion of the electric field (see green lines in Fig. 3.3) was decreased by inserting copper plates with smaller holes between the reaction zone and the lens. The homogeneous electric field is created

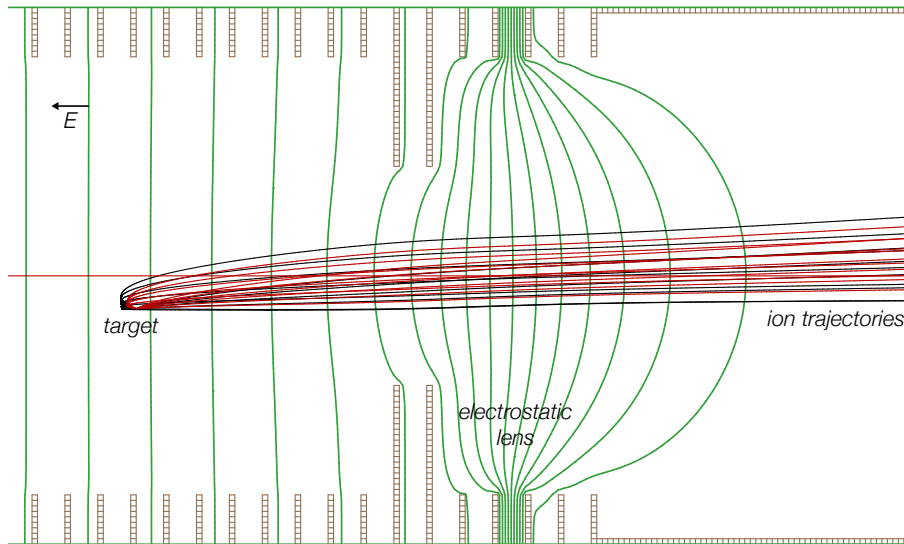


**Figure 3.3:** Simulation of the spectrometer created with a simulation program called SIMION. The black and red lines are trajectories of ions bent in the strong field of the *electrostatic lens*. Lens and geometry are adjusted in a way, that ions starting from different positions within a certain area in the target region can be focused onto one point on the detector.

by identical resistors between the evenly separated plates. By inserting a high resistor between two copper plates we form the inhomogeneous field of the lens on the recoil side. The necessary strength of the field had roughly been simulated before. A precise lens calibration was performed by tuning through different resistances. We set the photon beam at two different positions and searched for the resistance value where the beam spot would remain on the same position of the detector. The voltage applied over a resistance of 9.92 MOhm was 85 V, resulting in a maximum field strength of  $\sim 170$  V/cm. The homogeneous electric field in the interaction zone and on the electron side was  $\sim 15.3$  V/cm.

Electrostatic lenses have been used earlier in ion TOF spectroscopy. Recently, Schöffler et al. [47] showed that the method can be used successfully in experiments with molecules in COLTRIMS setups.

## 3.3.2 Geometry and resolution

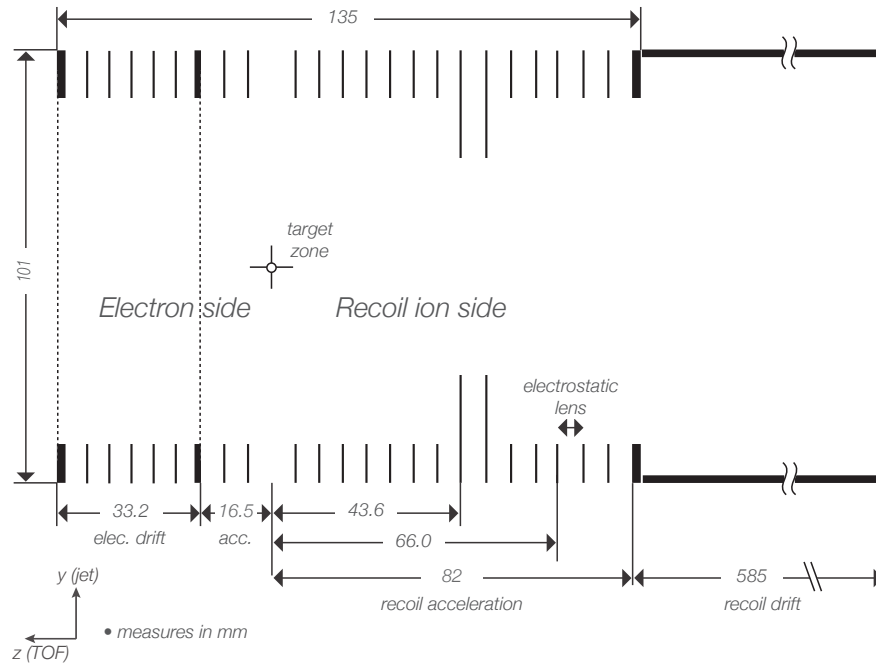


**Figure 3.4:** Drawing of the *spectrometer* (cut along the TOF-axis). The detectors are positioned at both ends of the spectrometer. The dotted lines represent meshes, the thin solid lines copper plates and the thicker solid lines aluminum holding plates. The target zone where the photoionization takes place is marked with a cross.

Figure 3.4 shows the geometry of the spectrometer. In this experiment we used 80 mm diameter MCPs (see Sec.3.4). The copper plates (100 mm x 100 mm) had a centered hole of 80 mm diameter, and each plate was separated by a 5 mm ceramic spacer from its neighbour. The frame consisted of ceramic rods on which the plates were stuck together. The acceleration region of the electron side measured 16.5 mm from the target to the mesh which separated it from the drift region. The electron drift region was 33.2 mm long and the electron MCP was fixed about 4 mm behind the last mesh (250  $\mu\text{m}$ , 80 % transmission). As described earlier, the high resolution in time-of-flight (TOF) direction was achieved by a long acceleration region. The first plate of the electrostatic lens had a distance of 66 mm to the target, and the total acceleration region of the recoil side was 82 mm from the target to the mesh. An aluminum tube enclosed the drift region of 585 mm. The center of the axis of the drift tube was set 10 mm above the center axis of the spectrometer in order to compensate for the calculated jet offset of 8-12 mm from the jet velocity.

In Table 3.3, the time and position parameters for the ions are shown. SIMION was used for simulation of the electric and magnetic fields in the spectrometer. The program provided errors of  $\Delta TOF = 1.4 \text{ ns}$  and  $\Delta xy = 0.25 \text{ mm}$  (FWHM) of particles starting from a target of 2 mm width in every direction in an electric field of  $|\vec{E}| = 15 \text{ V/cm}$ . The conversion to momentum uncertainty was performed from the ratio of momentum to time interval in TOF direction and to distance on the detector. The uncertainty from target temperature was neglected here. However, obtained values are averages, the resolution of the lens depends on the position and the local resolution can be better or slightly worse.

The resolution of the electrons was simulated with a program called MrSimulizer! which solves the equation of the electron trajectories and calculates the propagation of uncertainty.

In Fig. 3.5, the color scale represents the resolution of the electron energy in eV at different electron energies and emission angles in the laboratory. The resolution on the electron detectors was defined by the spacial target extension (1.7 mm). In time-of-flight direction the electronics provide a resolution of 0.1–0.5 ns. The resulting uncertainties in momentum are shown in Table 3.4.

**Table 3.3:** Spectrometer simulation for  $CO^+$  and  $O^+$  ions from a target of  $2 \cdot 2 \cdot 2 \text{ mm}^3$  diameter at  $|\vec{E}| = 15 \text{ V/cm}$ .  $TOF_0$  corresponds to ions without initial momentum.

Ion	$TOF_0$ [ $\mu\text{s}$ ]	TOF factor [ $a.u./ns$ ]	Position factor [ $a.u./mm$ ]
$CO^+$	21.1	0.136	1.11
$O^+$	16.1	0.137	0.83
Average resolution		0.2 a.u.	0.3 a.u.

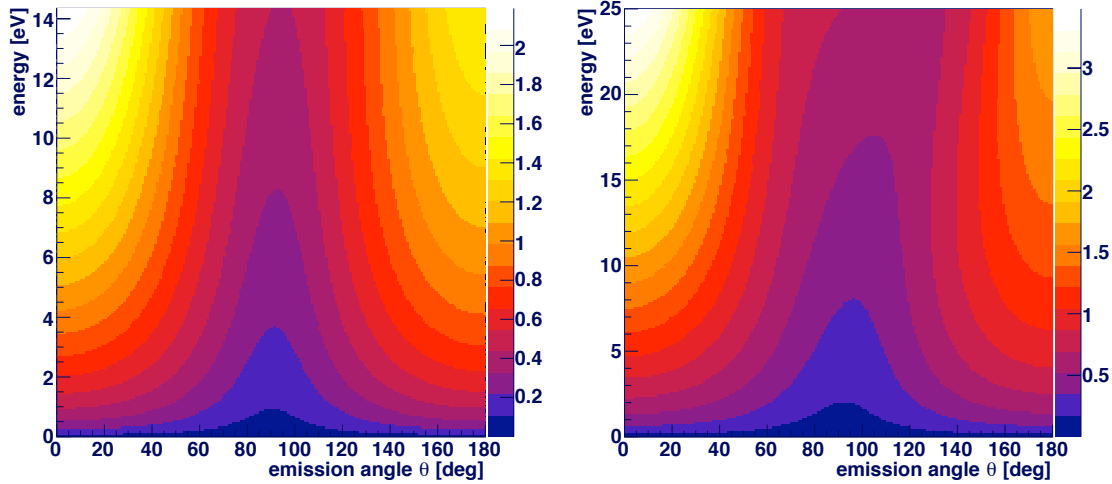


**Figure 3.5:** Histograms of the simulated electron energy resolution at  $|\vec{B}| = 8.5 \text{ Gauss}$  (left) and  $|\vec{B}| = 9 \text{ Gauss}$  (right); An angle of  $\theta = 0^\circ$  corresponds to emission along the time-of-flight axis towards the detector and  $90^\circ$  to an ejection in the jet-direction.

### 3.4 Detectors and readout electronics

The detectors consist of two parts delivering the time and position information. The momentum in time-of-flight direction was obtained from a *multi-channel plate (MCP)*, and the position information was sent by the *delay-line anode*.

A MCP consists of thousands of narrow tubes. When a particle hits the MCP inside the tubes, electrons are emitted. A very strong electric potential of about  $1kV$  applied to the plate drives the electrons through the tubes while they hit the walls several times, each time producing more electrons. Usually one puts two plates together in order to provide a sufficient amplification. The tube axis is at an angle to the TOF-axis, which enhances electron ejection. Back-flow of electrons is decreased by placing the plates at a non-matching tube direction, i.e. blocking the direct pathway of the electrons.

**Table 3.4:** *Simulation of the electron resolution with MrSimulizer! at an electric field of  $|\vec{E}| = 15.3 \text{ V/cm}$ , assuming a spatial target extension of  $\Delta y = 0.2 \text{ mm}$  and  $\Delta z = 0.16 \text{ mm}$ . The detector resolution was  $0.250 \text{ mm}$  and the accuracy of time measurement was  $0.5 \text{ ns}$ .*

$e^-$ energy [eV]	$ \vec{B} $ [G]	$\Delta\mathbf{p}$    TOF [a.u.]	$\Delta\mathbf{p}$ $\perp$ TOF [a.u.]	$\Delta\mathbf{p}$ anti   TOF [a.u.]
14.3	8.5	0.40	0.17	0.32
26.8	9.0	0.50	0.22	0.35

Positioned behind the MCP, the *delay-line anode* provides the position coordinates. A frame holds two pairs of closely winded copper wires, each for one direction in space. When an electron cloud emerges from the back of the MCP stack, the position on the anode can be calculated from the runtime of the signal in the wire and the size of the detector (see Sec. 4.1). Further technical information about MCPs and delay-line anodes can be found in [20, 56, 40].

### 3.4.1 Signal acquisition and conversion

The short signal pulse sent from the detectors is hidden in a very high voltage needed to run the MCPs. Therefore, the small signal (50–100 mV) a particle produces has to be decoupled from the high voltage applied (up to several kV). This is done by using high pass filters consisting of a condensator which only high frequency pulses can pass and a resistor to create the connection. The filters are contained in *decoupling boxes* with high-voltage and NIM-standard connectors as well as potentiometers for signal tuning. The signal height is increased in fast amplifiers modules. A device called *constant fraction discriminator (CFD)* serves as a standard to detect pulses independent of their signal height or width. For detailed information see e.g. [28].

### 3.4.2 Time measurement

In order to obtain the times-of-flight or the runtime of a signal in the anode wire, the time between signals has to be measured with very high accuracy. The *time-to-digital converter (TDC)* is an electronic module which can determine time differences in several channels with better than 1 ns accuracy. The memory of the TDC is organized like a bi-directional shift register, collecting data up to 16 hits per channel. The TDC stores data collected in every channel until it is full and discards the first recorded hits once it receives more hits than the channel can store. Depending on the running mode, one can control which events in reference to the *trigger* signal shall be stored. The memory of the TDC is then written to a hard drive. Usually, it is built on a PCI card which is plugged in a slot of the data acquisition PC.

A TDC (TDC8HP see [40]) in common start mode was used with a resolution of 25 ps. The data from a 40  $\mu\text{s}$  interval before the trigger signal was stored.

### 3.4.3 Operation specifications

Data was only recorded when two ions and one electron were detected in coincidence. The electron opened a 1  $\mu\text{s}$  gate in time for the bunchmarker of the beamline in order to store three bunchmarker signals. Another electron gate was set delayed with sufficient width in order to contain the recoil ions with TOFs of about 14.5–16  $\mu\text{s}$ . The recoil signal was

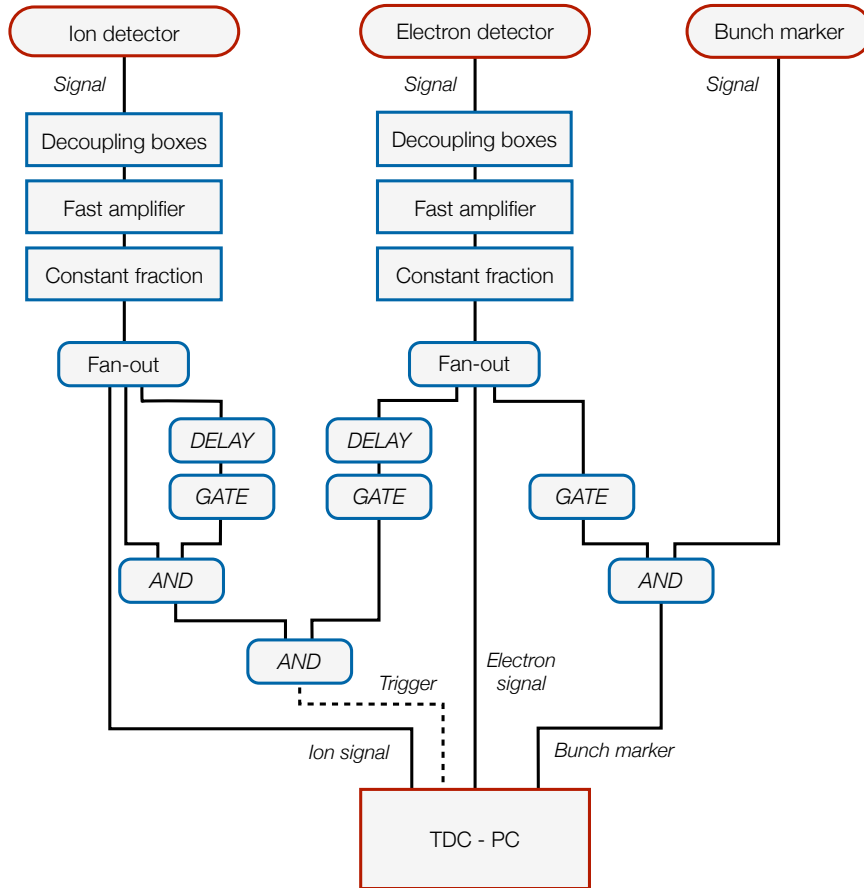


**Figure 3.6:** Schematic of the electronic connections. The detectors and the spectrometer were connected to high-voltage power supplies providing the electric potential at each point. The signals were extracted from the voltage by *decoupling boxes*, amplified and converted into a standard pulse in the constant fraction discriminator. The coincidence set-up sent a *trigger* signal to the *TDC* when at least one electron and two ions were detected in a certain interval (see Fig. 3.7).

duplicated and delayed by about  $2.5 \mu\text{s}$  and opened a time gate longer than the maximal time spread of the ions which was about  $7 \mu\text{s}$ . This signal, the unmodified recoil signal and the electron gate were combined by logical ‘and’ modules resulting in a setting which would trigger the TDC only if at least one electron and two ions are detected.

The data was stored to a PC in list-mode format. Each trigger corresponds to one event. In later data analysis, the data were controlled for every event, whether the stored data matched a double photoionization reaction or were due to random coincidences. In this way, millions of events were stored which contained the full kinematic information about the reaction.

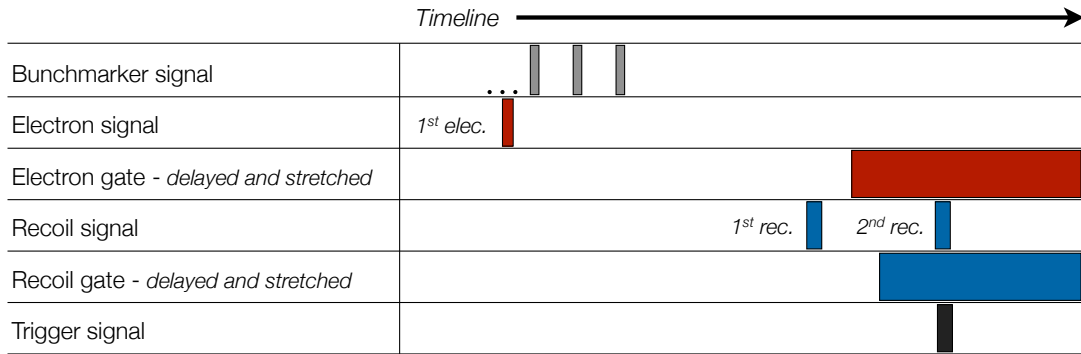


**Figure 3.7:** Schematic of the coincidence logics. The trigger signal is given if a second recoil signal arrives in the time gates opened by the electron hit and the first recoil hit.

**Table 3.5:** Detector count rates at 312 eV photon energy, horizontal polarization

	21 mA	44.6 mA
<b>Ring current</b>	<b>21 mA</b>	<b>44.6 mA</b>
Slit setting	70/100	40/100
Electrons	32 kHz	40 kHz
Ions	4 kHz	4.6 kHz
Coincidence	180 Hz	227 Hz

### 3.5 Synchrotron light source

Visible light from red to violet has photon energies in the range of  $\sim 1.5\text{--}3 \text{ eV}$ . As ionization of the carbon  $1s$  shell requires a photon energy of more than  $297 \text{ eV}$ , a special light source was needed. A *Synchrotron* produces light in a broad range of eV–keV energies. In a Synchrotron facility, an electron (or positron) beam is accelerated and circulates at relativistic velocity in a large ring. The electron packets emit highly focused light at each acceleration point. The photon beam reaches the experimental end stations through several beamlines tangential to the ring.

This experiment was performed at beamline 11.0.2 at the *Advanced Light Source (ALS)* in Berkeley, California, USA. The electron beam has an energy of 1–1.9 GeV in a ring of 200 m circumference. In multi-bunch mode, several electron packages circulate in the ring, and light is emitted every 2 ns. In this case, it would not be assured that the particles

detected in the measurement were produced from the same reaction i.e. coming from the same molecule. Therefore the experiment was performed during two-bunch mode when only two electron packets circulate in the ring at an interval of  $328.226 \text{ ns}$  (radio frequency of  $499.642 \text{ MHz}$ ). A signal called the *bunch marker* is sent continuously in the same interval as the electron bunches, which is needed as a reference time for TOF measurement (see Sec. 4.1). As electrons interact continuously with background particles in the ring, the beam intensity decreases exponentially and the lifetime is limited to  $\sim 60 \text{ min}$  for an injection at a  $40 \text{ mA}$  beam current.

The light at beamline 11.0.2 is extracted by an Elliptical Polarization Undulator (EPU5) covering an energy range of  $71\text{--}3000 \text{ eV}$  at  $1.9 \text{ GeV}$  electron energy [26]. Horizontal, vertical, circular and elliptical polarization of light can be selected by changing the phasing of the magnet rows in the undulator. The photon flux is estimated to be  $10^{12}\text{--}10^{13} \text{ ph/s}$ . The photon energy can be selected by a monochromator with two different gratings of  $1200 \text{ l/mm}$  or  $150 \text{ l/mm}$ . The beam position can be moved with bending magnets in horizontal and vertical direction, and horizontal and vertical slits provide the possibility of reducing the beam intensity. A technical drawing of beamline 11.0.2 can be found at [59]. A detailed description of synchrotron light and the ALS facilities can be found in [56].

### 3.5.1 Focus adjustment

The calculation of the initial momenta of the ions and electrons will only be correct if all particles start at a well defined point in the interaction zone. However, the target is not a singularity, but a volume of a certain size. A finite target volume will lead to an uncertainty of the calculated momenta.

Time- and space-focusing geometry (see Sec. 3.3) can reduce this error, but it is necessary to make the target zone as small as possible. This can be done by confining the area where photons hit the gas jet. The size of the beam is defined by the geometry of the jet expansion (in this case by the distance and width of the pinhole) and usually this is not easily improvable. The other possibility to reduce this area is to minimize the focus size of the photon beam as much as possible.

Usually, phosphor screens in front of and behind the spectrometer were used in order to estimate where the focus of the photons in the spectrometer was minimal. This was just a rough estimation as neither the exact distance of the screens to the gas jet was known, nor could the size of the spot be precisely checked on the screen itself. Also, the two independent measurements (looking at each phosphor screen) produced an increased error. Therefore, a tool was designed which makes it possible to measure the spot size exactly in the target region, without having to interpolate between two points.

There are several difficulties in measuring the spot size directly in the target zone: first, the specific position is hard to access as the vertically fixed copper plates in the spectrometer are only  $1 \text{ cm}$  apart from each other at this point. The horizontal ceramic rods holding the copper plates also inhibit the option of just pushing a measurement device into the spectrometer. The position above the skimmer, where the gas jet comes out, is critical to any pollution, as it could clog the tiny hole of the skimmer under the spectrometer. The phosphor screens tend to lose their coating, and for this reason, a phosphor screen would not be suitable as an optical indicator. Finally, the mechanism of moving the measurement device into the target zone and taking it completely out of the way of the photon beam for measurement has to be very reliable and work in vacuum.

The described difficulties were addressed by constructing a small arm holding a scintillator which is fixed perpendicularly to a rod. A flexible copper cable connects the rod to a rotational feedthrough which can be manipulated from the outside of the chamber. The scintillator is screwed with a little plate on the arm, while it is secured from breaking by

rubber (*Viton*) pads. When turned into the spectrometer, a small distance holder on the arm touches the ceramic spacers inside the spectrometer and ensures a perfect positioning of the device in the reaction zone. The used parts are non-magnetic and the system is isolated by ceramic spacers to the spectrometer.

With the new measurement setup it was possible to turn the scintillator into the interaction region in the spectrometer. A high magnification camera was pointed on the scintillator in order to adjust the focus to its minimum right where the photon beam crossed the gas jet. The absolute spot size could not be measured because the scintillator resolution was too small. At an exit slit setting of  $100 \times 100 \mu m$  the spot size was estimated to be not larger than  $160 \mu m$  in horizontal direction and  $200 \mu m$  in vertical direction.

The mechanism proved to be very reliable under vacuum conditions. An important improvement would be the replacement of the scintillator material with better optical properties in the range of the used synchrotron energy. A further upgrade could be the use of a wire on the scintillator. The photo current measured in the wire would probably give a precise information about the focus position.

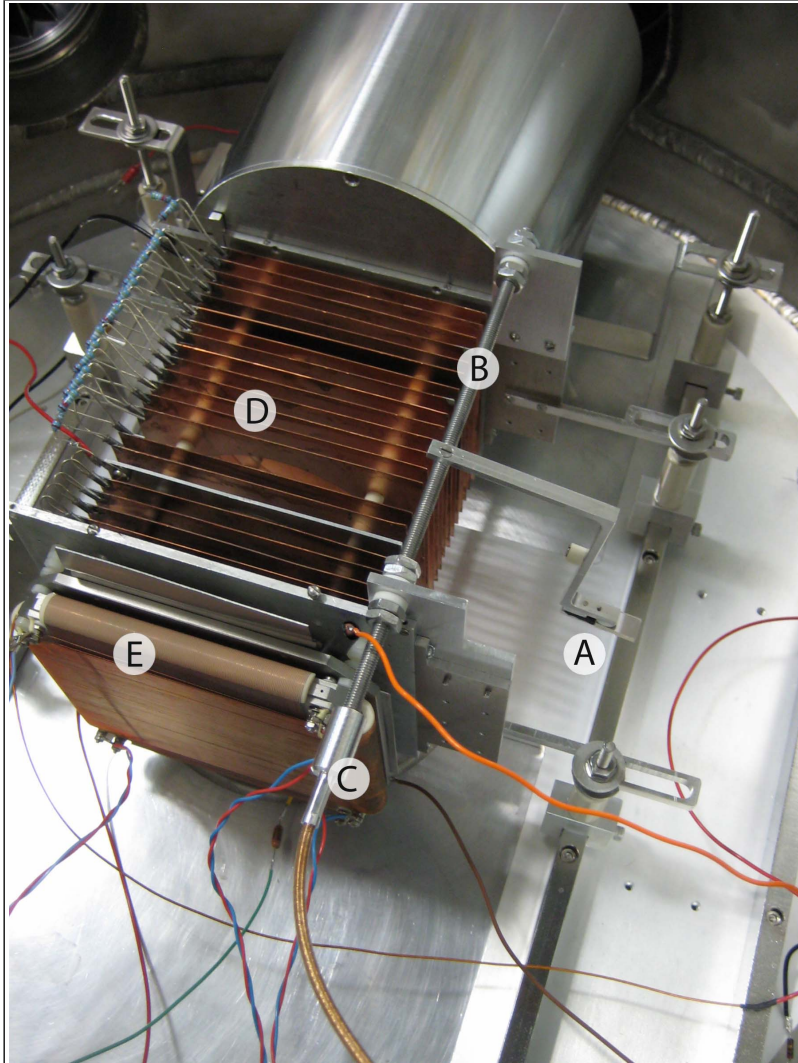


**Figure 3.8:** Photo of the spectrometer with the mechanics for focus adjustment. The scintillator (A) is fixed on a small arm which is screwed perpendicularly to a long rod (B). A cap (C) on the rod connects it to a copper wire which establishes the control by a rotational feedthrough from outside of the chamber. The light comes from the left crossing the gas jet in the middle of the spectrometer (1 cm gap below (D)) at a  $90^\circ$  angle to the spectrometer axis. On the lower end of the spectrometer the electron detector is mounted. The copper wires of the Delay-line Anode are labelled with (E).

## 4 Data Analysis

In a COLTRIMS experiment, every set of particles stored, which is called event, can be attributed to the reaction of a single molecule. In contrast to other experimental techniques, the orientation of the molecular axis, as well as the momenta of the electrons emitted from the molecule can be reconstructed not only as a statistical average, but for each event. By collecting several hundred thousands to millions of events in list-mode files, we obtain the statistical significance for an observed effect.

Several steps are needed in order to obtain the full momentum information of all particles. The real time-of-flight (TOF) and the positions of the particles on the detectors have to be derived from the data. The initial momenta can be reconstructed from this information. Several steps of calibration have to be performed and corrections for disturbing effects have to be included. In this experiment, the main difficulty was the use of an electrostatic lens which made a position dependent correction necessary. After calibration, the momenta provide the possibility to look at physical dependencies, such as the emission intensity of the electrons at different angles to the molecular axis.

The analysis was performed with a C++ program which has been developed in our group. The program was divided into three parts.

1. Data readout
2. Calibration and corrections
3. Physical calculations

The data were processed subsequently in the three parts. Conditions on time-of-flight and momentum conservation filtered out random coincidences from the real events. After each step, only the results were stored to a new file which reduced the amount of data used in the next step. First, the raw data from the list-mode files were transformed into TOFs and positions on the detectors. The momentum calculation and several corrections were performed in the second step, and the calculation of angles between the particles was performed in the last step. The results were visualized with the ROOT program-package developed at CERN. In the following, the different parts of the analysis are described.

### 4.1 Data readout

In the first step, the recorded data labelled with channel numbers are assigned to the signal source from the detectors. The pre-sorter algorithm checks for missing information that sometimes can be reconstructed by consistency considerations: if one of the two signals of a delay-line anode layer is missing, the position on the layer can still be obtained through the known runtime on the layer.

All data from the TDC channels written to the hard drive are time information. These times have to be transformed into positions on the detector and times-of-flight of the particles. Later, the momenta of every particle can be calculated from this information. The *delay-line anode* provides the position signal in the detector directions, in the following labelled as  $\vec{x}$  and  $\vec{y}$ . The difference of the signals from both sides of the anode layer carries the position information. The conversion factor of the anode time difference  $t_{d,x}$  to the

actual position  $x$  of a particle on the detector can be adjusted from the size of the layer  $l_x$  and the spread of the differences  $t_x^{dint}$ .

$$x = t_{d,x} \frac{l_x}{t_x^{dint}} \quad (4.1)$$

In practice, the fixed size of the detector is used to adjust the conversion factor until the calculation results in a correct detector size. The sum of the time signals from both ends of the layer should remain constant, independent of the position at which the electron cloud hits the anode, as wire length and signal speed do not change. In reality, however, this is rarely the case, and the time sum has to be shifted depending on the position to ensure a constant time sum over the whole detector range.

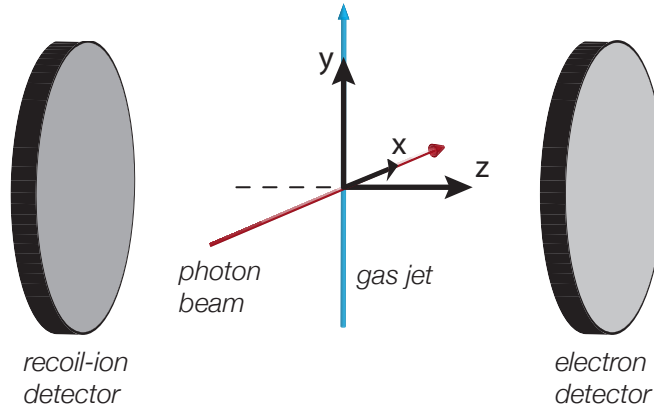


**Figure 4.1:** Coordinate system defined in the experiment. The time-of-flight axis corresponds to the  $z$ -axis, the gas jet is oriented in the  $y$ -direction and the photons move along  $x$ . We have no possibility of reconstructing the direction of the photons, as they do not affect the measured particles significantly.

The signal for the time-of-flight direction, along the axis of the spectrometer which is defined as  $\vec{z}$ , is sent by the MCP. The time stored by the TDC is defined by the interval between the last trigger and the hit signal and a constant offset from runtime in the electronics. Therefore, this time alone is random, and a reference time is needed. This signal is provided by the bunch marker, a signal provided by the synchrotron in the constant interval of two electron bunches (see Sec. 3.5).

Two to three bunch marker times were stored for each electron hit. The photoelectrons had a TOF of 15–40  $ns$  and the interval between two bunches was 328  $ns$ . The second closest time was used in case that one signal was cut by the electronics. This signal was obtained from the bunch marker time modulo(328) and subtracting one bunch marker interval. The obtained time is accurate up to an offset, which can be eliminated by the gyration period (see Sec. 4.2.1).

$$\boxed{t_e^{TOF} = t_e^{TDC} - t_{bunch}} \quad \text{Electron TOF} \quad (4.2)$$

In order to obtain the recoil TOF, the TDC time of the electrons was used as a reference point leaving only the TOF of the electron to add:

$$\boxed{t_{rec}^{TOF} = t_{rec}^{TDC} - t_e^{TDC} + t_e^{TOF}} \quad \text{Ion TOF} \quad (4.3)$$

Several different breakup channels exist for double photoionization of  $\text{CO}_2$  (see Sec. 5.1). The analysis focused only on the dominant breakup channel where the molecular ion fragments into two ions:



This channel was selected by limiting on an interval of the ion time sum and time difference around the breakup line in the PIPICO (Photo-ion photo-ion coincidence; see Fig. 5.1). As the  $\text{O}^+$  ion consistently hit the detector before the  $\text{CO}^+$  ion, the shorter time-of-flight could be assigned to the oxygen ion. The last and the penultimate ion times from the TDC array were used, discarding additional hits stored in the TDC.

The coincidence measurement of one electron and two ions ensured that in principle, every stored event contained enough information. Nevertheless, there were often random electrons and recoil ions recorded. These signals had to be separated from the ‘real’ data by setting certain conditions. The electrons were selected by controlling, whether using the electron TDC time would shift the recoil time sum in the right interval (see Equ. 4.3).

With some probability, Auger electrons were detected when emitted towards the electron detector and reached it before the photoelectron. Because of the minimal time difference between Auger electron and photoelectron ( $\sim 8 \text{ ns}$ ), the Auger would also provide a correct time sum of the recoil ions. Therefore, a second electron was searched among the recorded TDC times and the distinction was performed later in the code (selection from photoelectron TOF). However, in the case of Auger detection, it was likely that the dead time of the detector would inhibit the detection of the photoelectron.

## 4.2 Momentum calculation

### 4.2.1 Time zero and magnetic field

The bunch marker provided a reference signal for the photons triggering the reaction. It is a periodic signal linked to the electron bunches, hence, the bunch marker has an offset to the point in time when the photon hits the molecule. The absolute time zero can be obtained by looking at the *wiggle or fish spectrum*. Figure 4.2 shows the electron radius versus its TOF. The histogram exhibits a bow-like structure which is called a wiggle. The homogeneous magnetic field accelerates moving electrons always perpendicular to the  $z$ -direction which forces them onto a spiral trajectory. After the gyration period  $T_{gyr}$ , an electron has performed exactly one circle and reaches the same position independent of the starting direction. The electron TOF is shifted until the interval from  $t_0$  to the first node equals one gyration period.

$T_{gyr}$  depends on the magnetic field  $|\vec{B}|$ , mass  $m$  and charge  $q$ . The field can be calculated from:

$$\boxed{|\vec{B}| = 2\pi \cdot \frac{m}{q} \cdot \frac{1}{T_{gyr}}} \quad \text{Magnetic field} \quad (4.5)$$

Wiggle spectra were recorded in a separate run with low electric field in order to obtain several nodes. Therefore, the calculated magnetic fields and the time zero point were not exactly the same as in the real measurement, and they had to be adjusted slightly in later calibration.

### 4.2.2 Electron momentum

When an electron hits the detector, it possesses momentum from the reaction but also momentum absorbed from the electric field. In TOF-direction the magnetic field does not

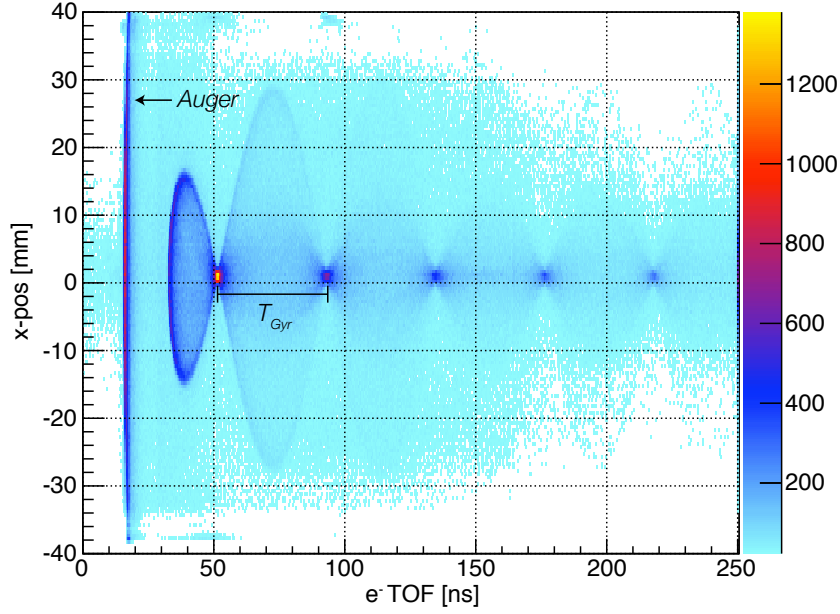


**Figure 4.2:** *Fish spectrum* showing the electron TOF versus x-position on the detector. This data is recorded for calibration of the magnetic field in a separate run at lower electric field. The time offset is adjusted by shifting the TOF to the extrapolated value of the zeroth node. The vertical line at the lowest TOF are the Auger electrons.

affect the momentum  $p_z$  of the electrons. The movement of the electron in the  $z$ -direction, with acceleration length  $s_a$  and drift length  $s_d$  is described by the following equation [21]:

$$\begin{aligned} s_a + s_d &= v_a t_a + \frac{1}{2} a t_a^2 + t_d (v_a + a t_a) \\ &= \frac{p_z}{m} t + \frac{1}{2} \frac{(t^2 - s_d^2)}{\left(\frac{p_z}{m}\right)^2 + s_a q |\vec{E}|} q |\vec{E}| \end{aligned} \quad (4.6)$$

The total TOF is the sum of acceleration time and drift time  $t = t_a + t_d$ , and  $v_a$  is the initial velocity. The exact solution is given by

$$p_z = m \left( -\frac{1}{3} z + \frac{|A+B|}{A+B} \cdot |A+B|^{\frac{1}{3}} + \frac{|A-B|}{A-B} \cdot |A-B|^{\frac{1}{3}} \right) \quad (4.7)$$

where  $z$ ,  $A$  and  $B$  are:

$$\begin{aligned} z &= \frac{1}{2} \frac{q |\vec{E}|}{m} t - \frac{(s_a + s_d)}{t} \\ A &= -\frac{C}{54} \quad B = \sqrt{\frac{1}{4} \cdot \frac{1}{27^2} \cdot C^2 + \frac{1}{27} \cdot \left( \left( 2 \frac{q |\vec{E}|}{m} s_a - \frac{1}{3} z^2 \right)^3 \right)} \\ C &= 2z^3 - 18z \cdot s_a \frac{q |\vec{E}|}{m} + 27 \left( \left( \frac{q |\vec{E}|}{m} \right)^2 s_a t - \frac{s_d^2}{2} \frac{q |\vec{E}|}{m t} - 2s_a (s_a + s_d) \cdot \frac{q |\vec{E}|}{m t} \right) \end{aligned}$$

As the analytical solution is rather long, an iterative method is used to derive  $p_z$  from the equation of motion 4.6 (see [44] for a detailed description).

In the detector directions  $p_x$  and  $p_y$ , the electric field does not influence the particles. Instead the magnetic field forces the electrons into a circular motion at angular frequency  $\omega = \frac{q}{m}|\vec{B}|$ . The equations of motion read:

$$x(t) = \frac{p_x}{m\omega} [\cos(\omega t) - 1] + \frac{p_y}{m\omega} \sin(\omega t) \quad (4.8)$$

$$y(t) = \frac{p_x}{m\omega} \sin(\omega t) + \frac{p_y}{m\omega} [1 - \cos(\omega t)] \quad (4.9)$$

The solutions of the initial momenta in the x-y plane are:

$$\boxed{p_x = \frac{m(b \cdot x - a \cdot y)}{a^2 + b^2}} \quad \text{Electron } x\text{-momentum} \quad (4.10)$$

$$\boxed{p_y = \frac{m(-a \cdot x - b \cdot y)}{a^2 + b^2}} \quad \text{Electron } y\text{-momentum} \quad (4.11)$$

$$a = \frac{1 - \cos(\omega t)}{\omega} \quad b = \frac{\sin(\omega t)}{\omega}$$

### 4.2.3 Ion momentum and electric field

On the recoil side, as on the electron side, a spectrometer with *time-focusing* geometry was built (see Sec. 3.3). Nevertheless, the electrostatic lens changed the electric field on the ion side significantly and made a calculation assuming a homogeneous field unreliable. Instead the linear approximation could be applied: in a setup using time-focusing geometry, small changes in the starting point do not effect the total TOF. This is due to the minor difference in energy particles gain in the acceleration region after starting from different origins in the interaction region. One can extend this principle to certain spectrometers: if the initial energy of an ion is small in comparison to the total energy it gains in the accelerating electric field ( $E_0 \ll E_{acc}$ ), one can describe the initial momentum by a linear function of the TOF  $t$ .

$$\boxed{p_z = F_z \cdot (t - t_0)} \quad \text{Ion } z\text{-momentum} \quad (4.12)$$

The TOF spectrum of an ion shows two peaks, one for an ion flying directly towards the detector and one for flying away from the detector. The initial condition  $p(t_0) = 0$  is given exactly in the middle of both peaks (see Fig. 4.3).

The absolute value of the factor  $F_z$  is estimated by comparing the *KER* to a literature value from Mathur *et al.* [32]. This factor, represents the force of the electric field and one can calculate the value for the field  $|\vec{E}|$  with the charge  $q$  of an ion:

$$\boxed{|\vec{E}| = \frac{F_z}{q}} \quad \text{Electric field} \quad (4.13)$$

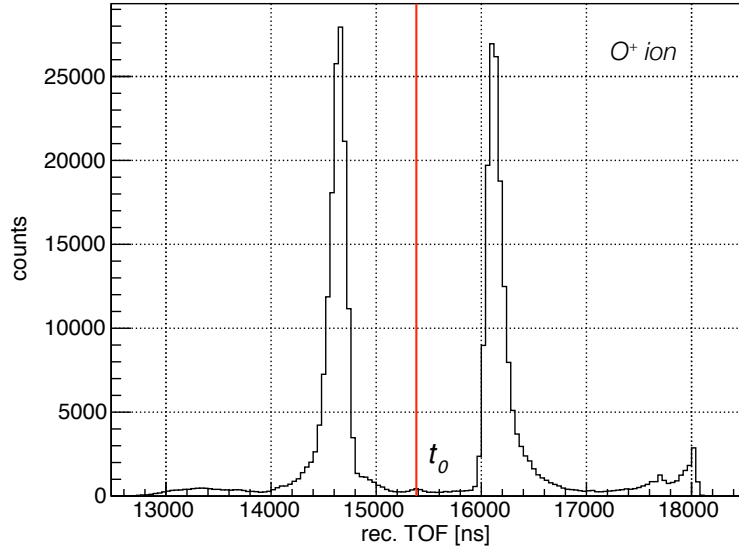


**Figure 4.3:** TOF of the oxygen ion. The middle of the two peaks for emission towards (low TOF) and away (high TOF) from the detector defines the zero point for recoil momentum calculation (see Equ. 4.12).

Assuming that the electric field around the interaction region is sufficiently homogeneous, we can use the obtained value of  $|\vec{E}| = 15.3 \text{ V/cm}$  for the calculations of the electron side.

In the detector directions, the ions are not accelerated by the electric field, nor does the magnetic field affect the ions significantly because of their large mass, and we can calculate the momentum of an ion from its position and TOF. Nevertheless, the lens does have a certain influence which is taken into account by introducing an additional factor  $C_{xy}$ . In the x- as in the y-direction, the momentum for an ion of mass  $m$  and TOF  $t$  reads:

$$p_x = \frac{x}{t} m \cdot C_{xy} \quad \text{Ion } x\text{-momentum} \quad (4.14)$$

After calculation of the momenta, it has to be confirmed that the independently obtained momenta for electrons and ions are consistent. The correct assignment of the channels during the experiment has to be verified by the physical quantities. As in most cases, it can be checked from momentum conservation. The momentum vectors calculated from the two different detectors have to point in the same direction. This can be controlled by looking at the sum-momentum of the ions plotted versus the electron momentum. At correct assignment, a diagonal line is obtained as an indicator for momentum conservation.

### 4.3 Calibration and corrections

The apparatus of an experimental setup will never match exactly the predicted values. There are uncertainties in the measurement, i.e. the length of the spectrometer, as well as effects not taken into account by the formulae such as external and distorted fields. In order to obtain correct absolute results, external data of well investigated phenomena are needed. If they were measured with higher precision, the values can be compared with data from the present experiment. Photons, photoelectrons and ions, as independently measured, needed a calibration with data from the literature.

### 4.3.1 Photon energy calibration

The calibration of the photon energy was performed with a fixed gas cell at the beamline. For energies around 300 eV, a scan of the  $\pi^*$ -resonance of CO was performed. Stolte *et al.* [53] reported a value of 287.4 eV. In comparison with our measurement of 289.56 eV, a beamline offset of  $\Delta E = 2$  eV was determined. At energies around 300 eV, using a grating with 150 l/mm and an exit slit opening of 100  $\mu\text{m}$ , the beamline provides a resolution of 0.42 eV.

### 4.3.2 Electron energy and momentum

The best way of assuring that the plotted momenta of the particles are correct is to check them for physical consistency. This was done by looking at the momentum bowls of the electrons and ions. As the maximal momentum of the photoelectrons is restricted by the photon energy (see Equ. 2.7), the electrons should be distributed on a sphere in momentum space. At most times, the momentum bowl is not round after calculation which is due to a mismatch of the parameters. The momentum bowl is a very sensitive control parameter and therefore it was the ultimate choice for calibration. The calculated parameters for electric field, magnetic field and time-zero were changed slightly in order to make the momentum bowl's shape round. Additionally, factors were introduced in order to stretch the directions in reference to each other and to shift the position until the momentum bowl for the photoelectron was round and centered to zero in every direction.

For absolute calibration, the measured energy was compared with a value of the carbon K-shell hole of  $297.63 \pm 0.01$  eV published by Prince *et al.* [39]. A small correction by one factor was applied on all momentum directions in order to shift the electron energy to this value.

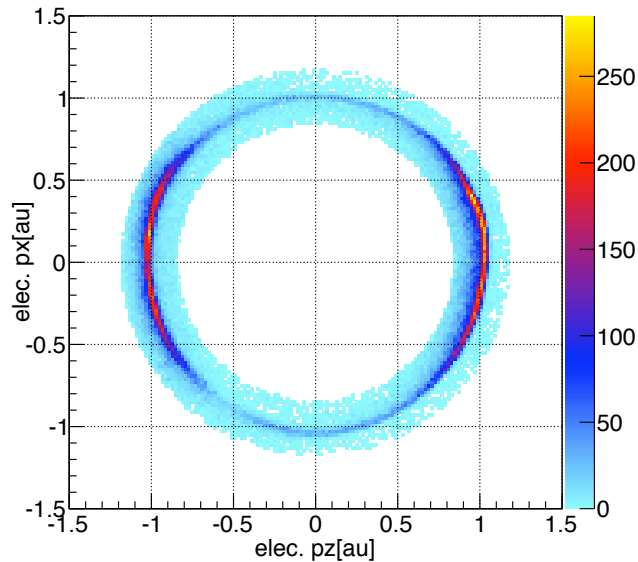


**Figure 4.4:** Photoelectron momentum in  $x$ - $z$  plane (energy restricted to the C(1s) mainline). A slice through the momentum bowl produces the observed ring. At a wrong adjustment of parameters like the magnetic field,  $t_0$  or the electric field, its shape is distorted. The pronounced intensity along the  $z$ -axis shows the preferred emission of the photoelectrons along the molecular axis at 312 eV photon energy (compare MFPAD in Fig. 5.5).

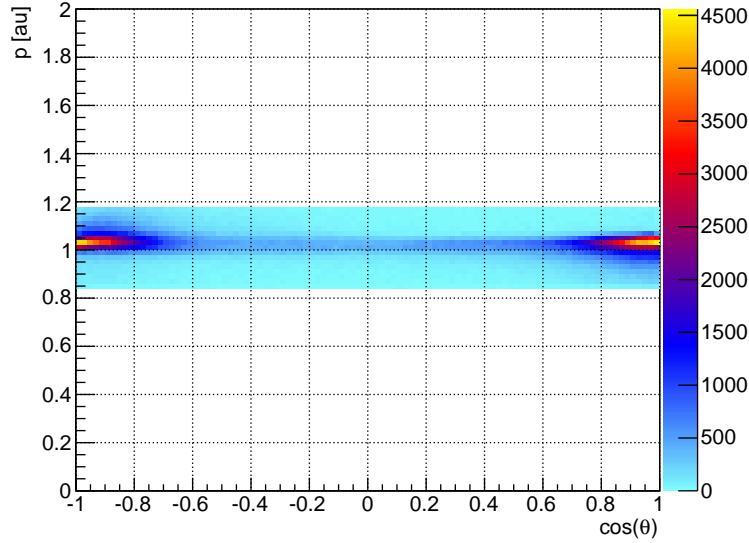


**Figure 4.5:** Photoelectron  $\cos(\theta)$  to TOF-axis (energy restricted to the C(1s) mainline). For correct adjustment of the experimental parameters, the plot shows a horizontal line and is therefore used to control these settings.

There is also a small effect due to *post collision interaction* changing the energy slightly and causing a tail to lower kinetic energies. After Auger decay, the ion changes from singly charged to doubly charged applying suddenly more force on the slowly escaping photoelectron. This slowing down of the photoelectron can be observed in an energy shift to lower kinetic energies.

### 4.3.3 Ion energy and momentum

The importance of resolution on the ion side made a geometry necessary in which only ions within an angle of  $\pm 21^\circ$  with respect to the TOF axis could hit the detector. Ions not emitted around the TOF direction missed the detector and were not detected. This resulted in a selection of molecular breakups roughly aligned to the TOF axis. The center of mass of the  $\text{CO}_2^{++}$  ion was moved by the momentum transfer from the Auger electron. This momentum transfer shifted each recoil ion slightly and produced an imprint of the Auger momenta on the sum  $p_{sum} = p_{rec1} + p_{rec2}$  of the recoil ion momenta. Taking into account the small momentum transfer the photoelectron causes on the center of mass, momentum conservation determines the Auger electron by the following equation:

$$\boxed{\vec{p}_{Aug} = -(\vec{p}_{ph} + \vec{p}_O + \vec{p}_{CO})} \quad \text{Auger electron momentum} \quad (4.15)$$

The momentum bowl of the Auger electrons is obtained from the combination of recoil ion sum-momentum and the photoelectron bowl, which is a useful proof of correct momentum calculation on the recoil detector. Factors and shifts were defined in order to obtain a constant radius of the bowl in every direction and to set the bowls centered to zero.

The momentum transfer of the photoelectron on the center of mass is visible in Fig. 4.6 (a). The photoelectron, which is mainly emitted along the z-axis (see Fig. 4.4), splits the Auger electron momentum into two displaced rings. Including the photoelectron reveals the Auger electron momentum shown in 4.6 (b). This clearly demonstrates the impressive resolution on the recoil ions and that the applied method works.

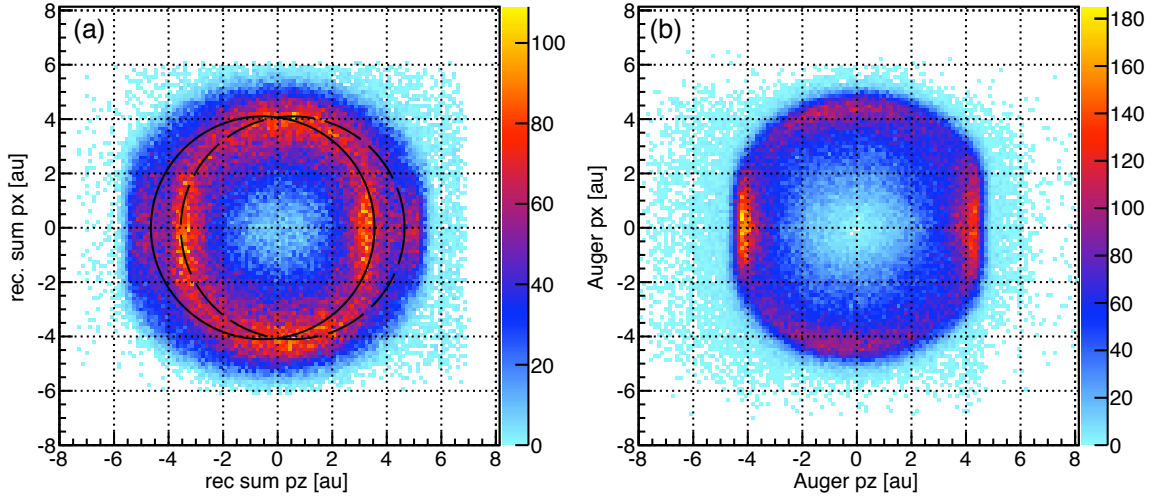


**Figure 4.6:** Recoil momentum (a) and Auger momentum (b) in x–z-plane. In (a), one can see two rings, each shifted horizontally from the center in the z-direction by  $\pm 1$  a.u.. This effect is caused by the photoelectron pushing the ions when ejected from the molecule (compare with Fig. 4.4). Subtracting the photoelectron momentum reveals the Auger electron momentum distribution, as shown on the right.

The *Kinetic Energy Release (KER)* is defined by the energy of the coulomb potential between the recoil ions at breakup time. This potential is transformed into ion kinetic energy and can be calculated from their relative momenta:

$$E_{KER} = \sum_{i=1}^3 \frac{(p_{1,i} - p_{2,i})^2}{8 \cdot \mu} \quad \text{Kinetic Energy Release} \quad (4.16)$$

Here  $p_{1,i}$  and  $p_{2,i}$  are the momenta of the first and second ions in the directions  $i = \{x, y, z\}$ ;  $\mu$  is the reduced mass (see Equ. 2.2.4). The absolute calibration was done by comparing the kinetic energy release with a measured value from Sharma *et al.* [49] who found a KER distribution around 6.17 eV.

## 4.4 Additional corrections

### 4.4.1 Electrostatic lens effects

Similar to an optical lens, an electrostatic lens can have some unwanted defects. In theory, the lens should not affect the momenta neither in the detector direction, nor in the TOF direction. Nevertheless, if one looks at the recoil sum-momentum of each direction versus the detector position, they usually do not remain constant over the whole detector, but show some quadratic behaviour.

In the present experiment, the dependency in each direction was different, and the momenta had to be corrected in each direction independently. In order to correct the lens effects, a grid of correction values read out from plots was used to interpolate the correction

value for every event.<sup>1</sup> The interpolation performed a linear weighting of the closest values in a three dimensional grid ( $x, y, p_{sum\ i}$ ). The momentum of each ion was shifted with half of the obtained correction value, assuming that the effect of the lens was about the same for the first and the second ion. A mathematical description of the interpolation function is noted in Appendix 1. It was derived from the function  $E104$  of the *KERNLIB* library [29].

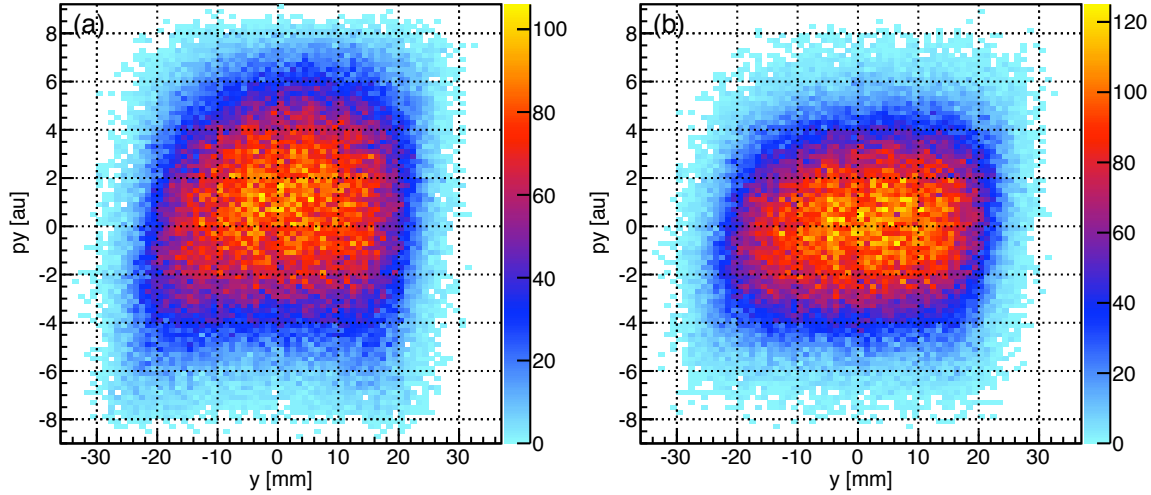


**Figure 4.7:** Ion sum momentum versus detector position in the  $y$ -direction. Plot (a) exhibits the influence of the electrostatic lens in a curved shape. In (b), the interpolation has mostly corrected this effect.

The correction by selected values was only performed for the ion momenta  $p_{sumx}$  and  $p_{sumy}$ . For  $p_{sumz}$ , dependency on one direction was small, yet lens effects would become clearly visible looking at the dependency of  $p_{sumz}$  on the radius, as effects of the single directions added up. This error was corrected by shifting each ion momentum  $p_{i,z}^{old}$ ,  $i = 1, 2$  with a quadratic function of the radius  $r_1$ . The factor  $A$  was obtained by quadratic fitting of selected values.

$$p_{i,z} = p_{i,z}^{old} - \frac{1}{2}A \cdot (r_1)^2 \quad \text{Lens correction for } p_z \quad (4.17)$$

#### 4.4.2 Time dependent drifting effects

The data recording is a long process, sometimes taking several days at one specific energy in order to have enough statistics. In order to use one set of calibration settings, it has to be controlled whether the parameters remain constant during the acquisition of a data file. The position of the target is one parameter which may vary. Small differences in temperature can cause the jet position to move and therefore change the target position. The event counter defines the number of the recorded event, thus, it can be used as a clock.

In this experiment, a shift in the jet position which effected the offset significantly was observed at some energies (see Fig. 4.8). In order to use only one calibration for the

<sup>1</sup>The tables containing the correction points were obtained by reading out the upper and lower value of the momentum at the detector positions  $x = \{-36, 30, 24, 12, 0, 12, 24, 30, 36\}$  sliced in  $y$ -direction at the same values. The table had  $2 \times 9 \times 9 = 162$  entries.

whole file of several hundred thousand events, a function was written to correct the time dependencies. The code calculated the average of the distribution of the affected parameter incrementally, providing a continuous shift value. If the distribution of the parameter is not symmetrical around its maximum, the average method returns a value different from the desired center position of the distribution. It was reasonable to assume that the shape of the distribution did not change; therefore, an initial offset of the average of the desired zero point was included.

The average of a given parameter  $v$  at event number  $i$  is calculated on an interval  $\delta$ . The initial offset is  $v_0$ . The corrected value  $v_i^{cor}$  is calculated from  $v_i^{old}$  with the following function:

$$v_i^{cor} = v_i^{old} + v_0 - \left( \sum_{j=i-\delta-1}^i v_j \cdot \frac{1}{\delta} \right) \quad \text{Time drift correction} \quad (4.18)$$

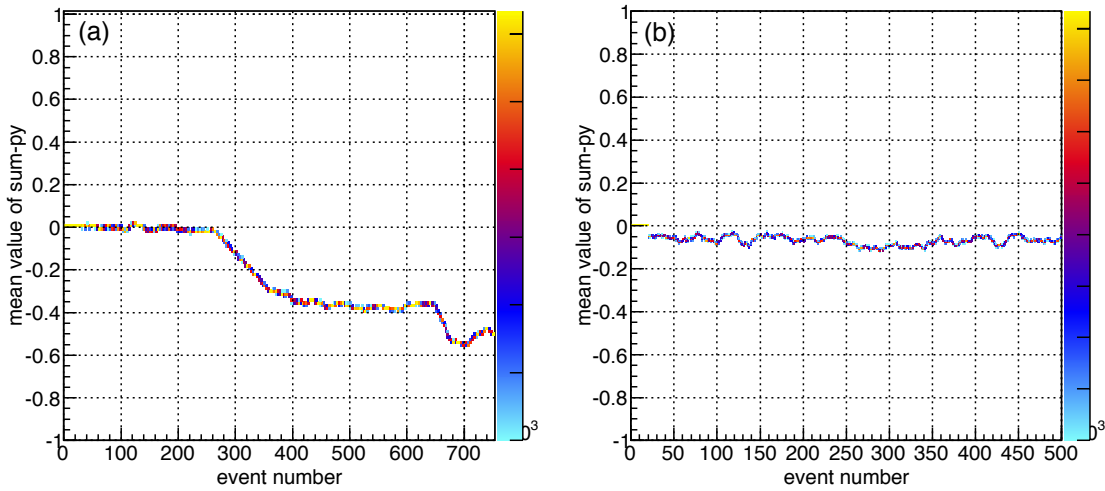


**Figure 4.8:** Mean value of the recoil momentum sum against event number before (a) and after time-drift correction (b). One can see that the shift of the jet position in time, apparent in (a), is successfully compensated by the function. Due to the rough averaging the function performs at each step, a small offset from the mean value to the intended zero of sum-py is made. The two graphs show the same interval, yet the event number in (b) does not match the one in (a) as there are some events sorted out by conditions.

## 4.5 Error analysis

The uncertainties in a measurement can be estimated in two ways. A propagation of uncertainty can be calculated with the errors and the resolution of the components of the experimental setup. In Sec. 3.3 uncertainties of the momentum measurements have been quantified in this way. However, it is more reliable to derive the errors from the data by looking at the obtained spectra: errors broaden a distribution around the true value. Usually, the error is defined as the *full width at half maximum (FWHM)* of a Gaussian-like distribution. While analyzing spectra, one has to consider that most lines contain a broadening which is not produced from experimental errors, but which is due to the lifetime of the hole state. If a state has a finite lifetime, it will decay after a random time, and the *Heisenberg uncertainty principle* for energy causes a certain width.

$$\boxed{\Delta E \cdot \Delta t \geq \frac{\hbar}{2}} \quad \text{Heisenberg uncertainty principle} \quad (4.19)$$

Additionally, information about the structure of the investigated peak is necessary, as the observed peak could contain substructure from vibrational levels.

### 4.5.1 Experimental uncertainties

At 300 eV, uncertainty of the photons obtained from the beamline is 0.42 eV. The FWHM of the photo main line at 312 eV is 1.6 eV (see Fig. 5.2) containing a width due to the natural lifetime of the the C1s core hole state of 100 meV [9]. Vibrational substructure is located at 165 meV from the main-line [19]. The calculated resolution of the electron momenta has been shown in Table 3.4. The resulting uncertainties in angular measurement are shown in Table 4.1.

**Table 4.1:** *Estimated uncertainties of the electron emission angle for ejection in different directions in the laboratory; the errors are obtained from geometrical calculation using the simulated uncertainties in the momenta shown in Table 3.4.*

$e^-$ energy [eV]	$ \vec{B} $ [G]	$\Delta\phi$ for $\vec{z}$	$\Delta\phi$ for $\vec{x}$ and $\vec{y}$	$\Delta\phi$ for $-\vec{z}$
14.3	8.5	$\pm 4.8^\circ$	$\pm 11.3^\circ$	$\pm 9.0^\circ$
26.8	9.0	$\pm 4.6^\circ$	$\pm 10.7^\circ$	$\pm 7.5^\circ$

A mayor importance in our experiment was the resolution of the recoil ion momenta which are related to the kinetic energy release (see Equ. 4.16). The relatively short lifetime of the doubly charged ions produced a natural width of the KER distribution larger than the resolution. Figure 4.9 shows the KER distribution of N<sub>2</sub> from breakup after double-photoionization at  $\gamma = 419$  eV [46, 47]. The setup used in this experiment had a very similar geometry on the recoil-ion side and similar fields to the present setup, and the estimated resolution of 50 meV should be comparable.

The lack of information about the natural width and the vibrational structure inhibits an absolute quantification of the error of the Auger electron momentum from the FWHM value. Still, Fig. 4.10 displays the relative resolution in different directions. In the x-direction the peaks show widths of 1.2 and 1 a.u., in the z-direction 0.9 and 1.5 a.u. FWHM and in the y-direction 3.7 and 4.2 a.u. FWHM. The high error in y, the direction of the jet, is due to the thermal energy uncertainty as discussed in Sec. 3.2.

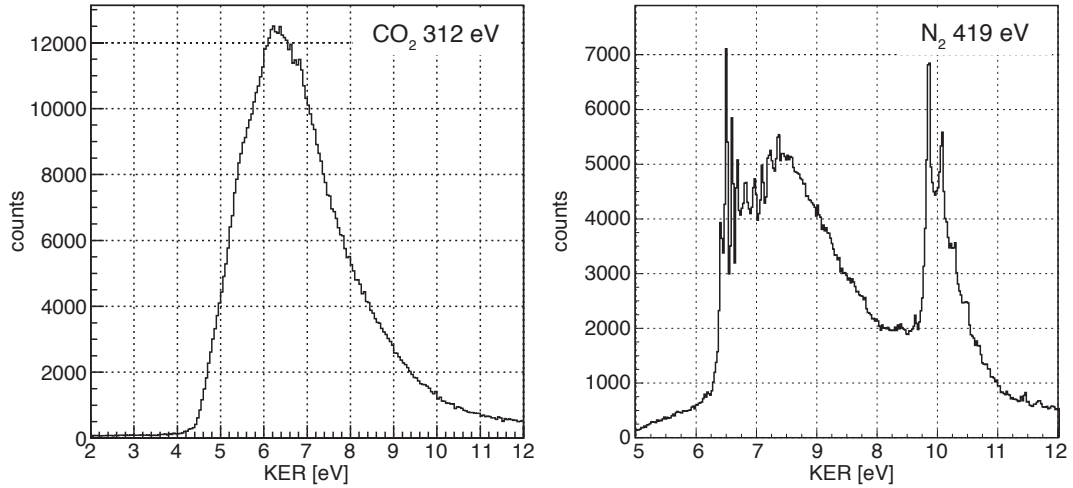


**Figure 4.9:** KER distributions after double-ionization of  $\text{CO}_2$  at 312 eV and  $\text{N}_2$  at 419 eV photon energy. The setup used for  $\text{N}_2$  was comparable to the present, having an almost identical recoil-side geometry with an electrostatic lens and similar fields [46, 47]. The vibrational structure visible in the  $\text{N}_2$  data provides the estimate of  $\sim 50$  meV KER-resolution of the setup.

The estimated error from jet temperature (Table 3.2) and the simulated spectrometer resolution (Table 3.3) have been shown in Sec. 3.2 and 3.3. The angular resolution calculates from the geometry to  $\pm 2.3^\circ$  for Auger electrons emitted in the jet-direction and to  $\pm 22.3^\circ$  for emission orthogonal to the jet.

#### 4.5.2 Statistical errors

Errors shown in the graphs are calculated by the square root of the value. For an experiment with  $n$  repetitions, the accuracy of a measurement increases with  $\sqrt{n}$ . This is due to the *central limit theorem*. It shows that a series of independent and identically distributed random variables converges for large numbers to the *normal distribution*. In an experiment, this means that if we measure a physical quantity, e.g. the time-of-flight  $t$ , where each measurement is independent and each follows the same physical rules (identical probability distribution  $P(t)$ ), the statistical error of a specific result  $t = a$  which was obtained  $N$ -times is defined by  $\sqrt{N}$ . The scaling of the statistical error of a specific value  $\sigma_a$  with the square root of the number of repetitions is shown in Appendix 3.

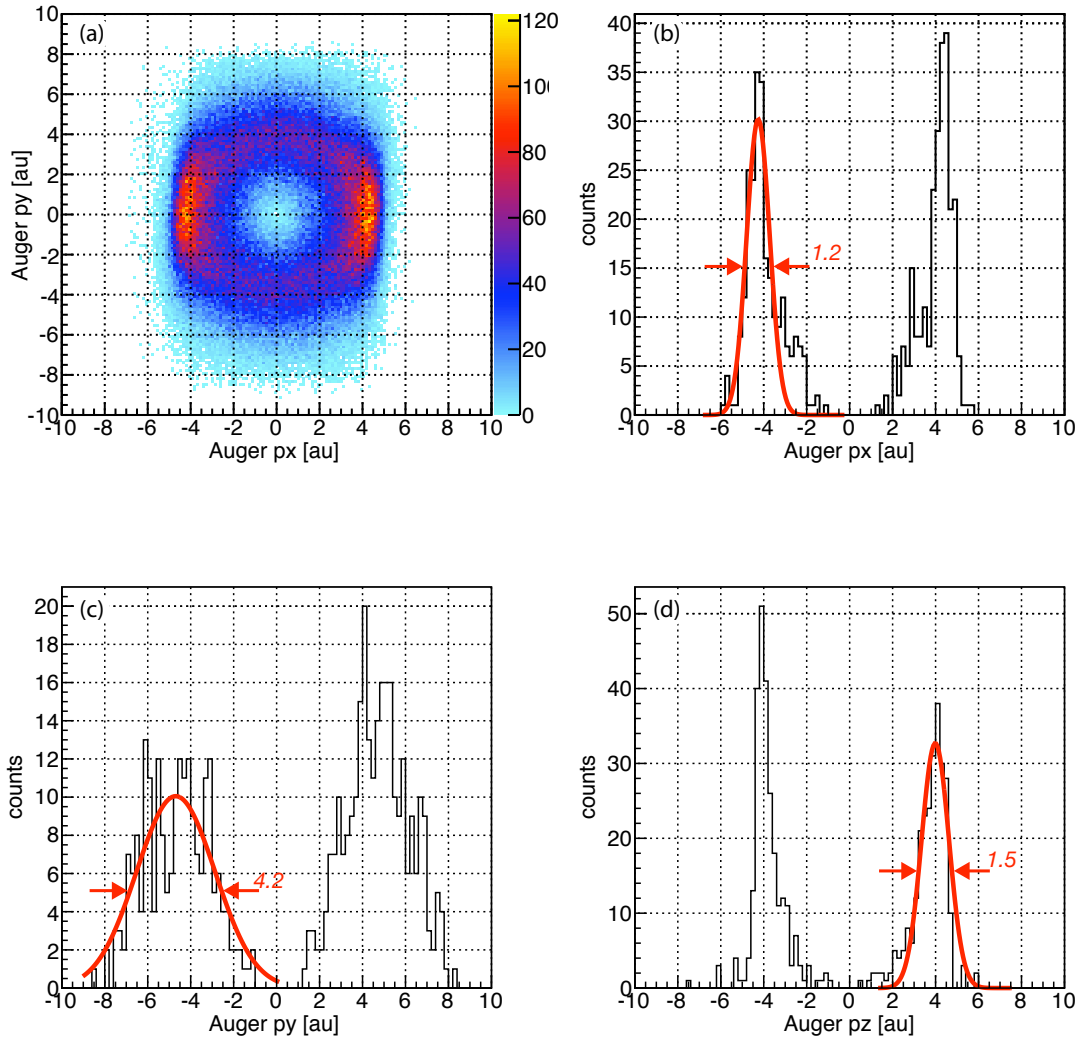


**Figure 4.10:** Auger electron momentum in x-z plane (upper left) and cuts from the momentum bowl. The plots contain counts from small patches cut out of the momentum bowl: e.g.  $px$  contains only counts within  $3^\circ$  angle around the x-y and x-z plane. The one-dimensional histograms give an estimate of the relative resolution in all directions. Target temperature makes the resolution in y-direction more than 4 times worse than in z-direction: FWHM is 1.2 and 1 a.u. in  $px$ , 3.7 and 4.2 a.u. in  $py$  and 0.9 and 1.5 a.u. in  $pz$ .

## 5 Results and Conclusions

In this experiment of double photoionization of  $\text{CO}_2$ , the main focus was on the investigation of a recently discovered asymmetry in the photoelectron angular distributions. Additionally to the photoelectron, we reconstructed the fixed-in-space Auger electron angular distribution in order to look for correlation effects between the two electrons. We confirm earlier results showing an asymmetry of the photoelectron angular distribution along the molecular axis after ionization of the  $\text{C}(1s)$  orbital. The high statistics and high resolution measurement unveils new asymmetric features in the photoelectron angular distribution which change as a function of the kinetic energy release (KER).

### 5.1 Breakup channels

In our measurement we did not detect only the breakup channel we planned on investigating but several other ions. The coincidence logics (requiring at least one electron and two ion hits) was mainly intended for reducing the amount of data measured. Still, the two detected particles can be any ions with positive charge that reach the detector within the time-frame defined by the electronic logic gates. Thus, there can be different ions from  $\text{CO}_2$  breakup as well as ions from background gas found in our data. We can attribute a ratio of charge to mass for each time-of-flight:

$$t_{rec} \propto \sqrt{\frac{q}{m}} \quad \text{Recoil ion time-of-flight} \quad (5.1)$$

Sometimes several ions match this ratio. In Fig. 5.1 one can see the time-of-flight of the first versus the second detected ion, where each point represents a detected ion pair. Capital letters are assigned to some of the observed features in the histogram. In the analysis we selected only the breakup channel into two positive ions  $\text{O}^+$  and  $\text{CO}^+$  (A). The two more intense islands along the line are the combinations  $\text{O}^+$  towards,  $\text{CO}^+$  away from the detector and vice versa. Intensity between these island is very low because there were no ions with low kinetic energy release and ions starting perpendicular to the detector were not detected (see Sec. 3.3). Towards the diagonal line in the histogram, there is a V-structure labelled with (B) which is due to *metastable states* of the  $\text{CO}_2^{++}$ -ion. For these states lifetime is long enough, so that they can dissociate during their flight towards the recoil ion detector. *Three-body breakups* appear at shorter TOFs marked with (D) for breakup into  $\text{C}^+ + \text{O}^+ + \text{O}$  and (C) for  $\text{C} + \text{O}^+ + \text{O}^+$ . In these cases, we do not see narrow lines any more, as one particle is not detected, carrying a part of the total momentum. This blurs the narrow line of momentum conservation in the picture. The short lines above labelled with (E) are separated exactly by the interval of the electron bunches and are caused by wrong bunch marker assignment. At  $25.5 \mu\text{s}$  TOF (F), the singly charged  $\text{CO}_2^+$ -ion hits the detector and produces a horizontal line in the spectrum when it is detected in coincidence with a random ion.

The spectrum of the photoelectron energy is shown in Fig. 5.2. The mainline from direct ejection, without further electron interaction, is located at 14.4 eV electron energy. Vibrational substructure (see [19]) in the main peak could not be resolved, whereas we can see peaks from satellite electrons (see page 15) at low energies. They correspond to the assignments  $\sim 2 \text{ eV} \equiv \text{S}_1$  and  $\sim 3.2 \text{ eV} \equiv \text{S}_4$  in Schmidbauer *et al.* [43].

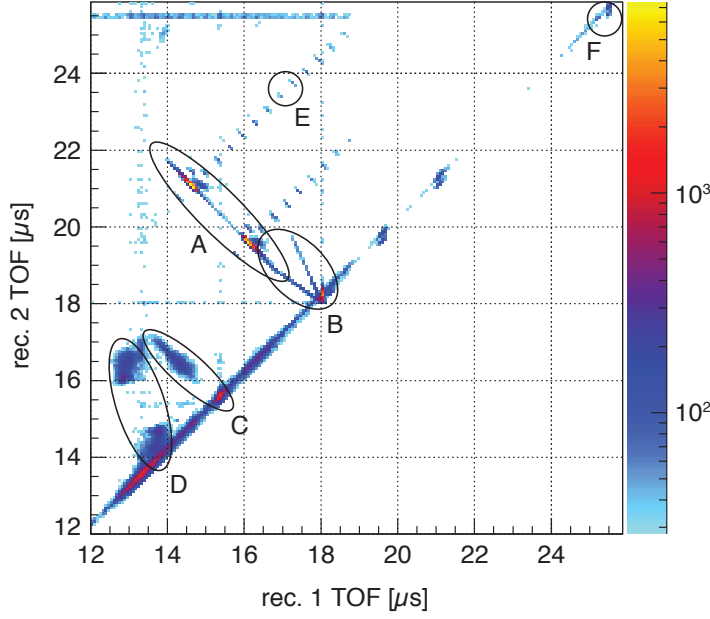


**Figure 5.1:** First versus second ion TOF. Also called *PIPICO* for *Photo Ion Photo Ion Coincidence*. Dissociation into  $O^+ + CO^+$  is labelled with (A). The additional V-structure (B) lying over the direct breakup of  $CO_2^{++}$  can be attributed to *metastable states* of the di-cation. For this decay ions break up during flight to the detector. The data contains three-body breakup into  $C + O^+ + O^+$ , marked with (C), and  $C^+ + O^+ + O$  (D). The equispaced lines (E) are due to wrong bunch marker assignment. (F) corresponds to the  $CO_2^+$  ion TOF.

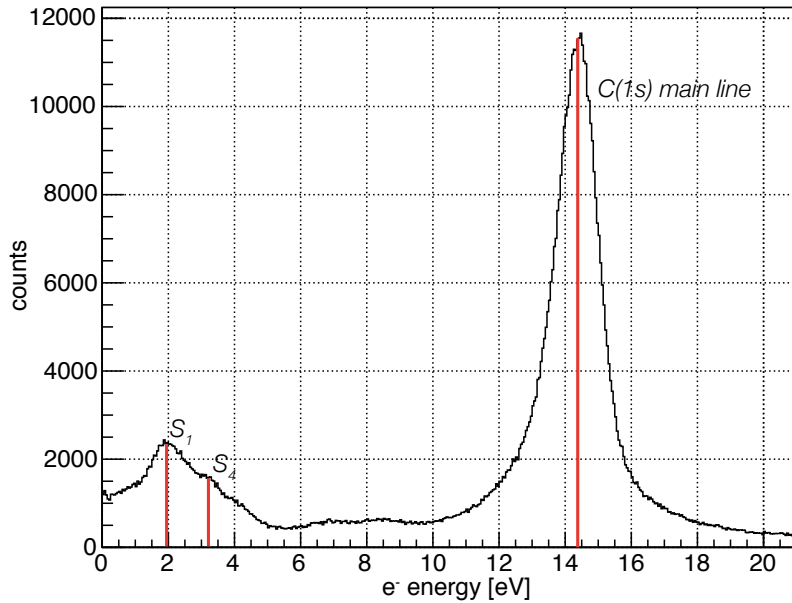


**Figure 5.2:** Electron energy distribution at  $\gamma = 312$  eV and horizontal polarization. The main photoelectron line is located at 14.4 eV. We can see intensity from satellite electrons at low energies ( $\sim 2$  eV  $\equiv S_1$  and  $\sim 3.2$  eV  $\equiv S_4$  in [43]).

## 5.2 Photoelectron angular distributions

Recently Liu *et al.* [30] measured C(1s) photoelectron angular distributions in the molecular frame (MFPAD) of CO<sub>2</sub>. They found an asymmetry of the MFPAD with respect to the O<sup>+</sup> and CO<sup>+</sup> fragments. The effect only appeared at the photon energies 312 eV, where a shape resonance is located, and at 320 eV, giving rise to the assumption that resonance enhancements play a role in causing the asymmetry.

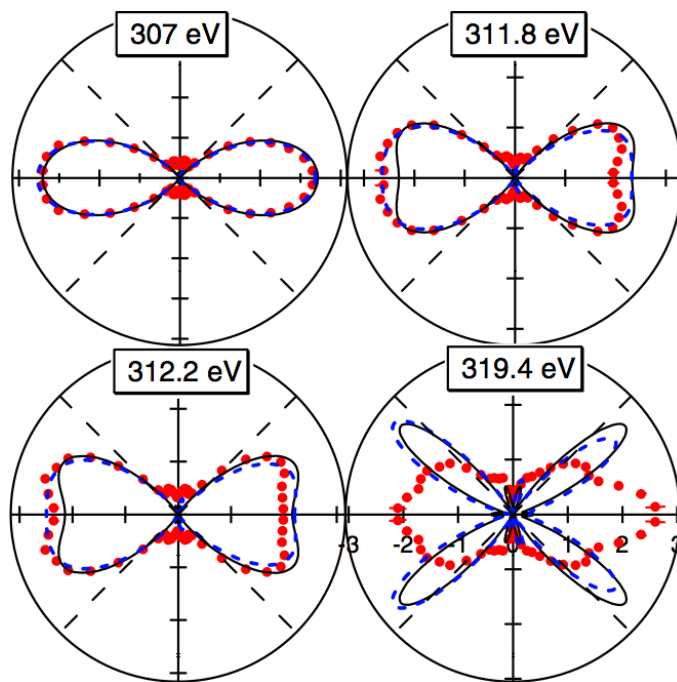


**Figure 5.3:** Molecular frame photoelectron angular distribution (MFPAD) measured by Liu *et al.* [30]. The surprising finding of asymmetric distributions with respect to the O<sup>+</sup> and CO<sup>+</sup> ions (horizontal in this plot) at 312 and 320 eV motivated this experiment. The solid and dashed lines show numerical calculations.

This observation is surprising for at least two reasons. Firstly the carbon dioxide molecule is linear with the carbon atom placed between the oxygen atoms. In the ground state the bond length between the carbon and both oxygen atoms is equal, around 2.2 a.u. [34]. The C(1s) orbital is almost spherical-symmetrical and diffraction of the electron wave at the oxygen atoms at equal distance should produce a symmetric electron angular distribution with respect to the center of mass.

Secondly, Liu *et al.* argued that the observed asymmetry provides evidence for a breakdown of the well established two-step model. Here, the process of photoionization with subsequent Auger decay is regarded as two independent steps (see Sec. 2.3.1). First the core electron is ejected from the molecule leaving it in an excited state. In a second step the core hole is filled by a valence electron, and another electron from an outer shell is ejected, usually carrying higher energy than the photo electron. Being doubly charged, the molecule dissociates via coulomb explosion. This model would not hold if there is a mixing of the intermediate states, as this would mean that the knowledge of the intermediate state does not define the final Auger state and we could not treat them as independent any more.

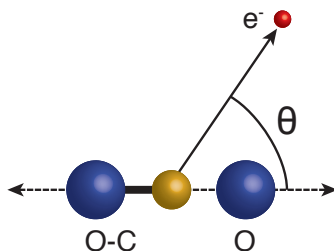


**Figure 5.4:** The angle between the electron and the molecular axis is called  $\theta$ . The orientation of the molecular axis was restricted to an angle of  $\pm 21^\circ$  to the  $z$ -axis in the laboratory.

Measured photoelectron MFPADs for linear polarized light at  $h\nu=303$ , 312 and 320.5 eV are shown in Fig. 5.5. These results are in excellent agreement with previous experiments [42, 30], and data are within the error bars of these earlier measurements. At the shape resonance at 312 and at 320.5 eV photon energy, the results confirm the asymmetry effect reported by Liu *et al.*. The photoelectron angular distribution shows higher intensity in the direction where the  $\text{CO}^+$ -ion flies after dissociation. We should recall at this point, that the asymmetric breakup into a  $\text{CO}^+$ -ion and an  $\text{O}^+$ -ion occurs after emission of the photoelectron and the Auger electron. Hence, the observed asymmetry shows a definite link between the initial ionization step and the final bond breakage which survives the intermediate Auger decay. Below the shape resonance, there is no asymmetry observed.

At low energies, p-wave contribution dominates clearly showing strong peaks along the molecular axis. Nevertheless, we were able to separate small contributions from higher order angular momenta, producing small peaks around perpendicular orientation to the molecular axis, which were not resolved in the previous works. In the following, we show that these additional lobes allow to unveil the mechanism producing the asymmetry. At higher energies, additional partial waves cause more complex distributions.

For circular polarized light at 312 eV, the asymmetry is much reduced as compared to linear polarization. This is also consistent with the results from Liu *et al.*, since the transition matrix element for circular light is a coherent superposition of those for linear light parallel ( $\Sigma$ ) and perpendicular ( $\Pi$ ) to the molecular axis. The asymmetry is only visible in the  $\Sigma$ -channel and is therefore much reduced for circular light.

### 5.3 Processes affecting MFPADs

As a possible explanation for the observed asymmetry, Liu *et al.* speculated that different C–O bond lengths of the individual molecule at the instant of photoabsorption could cause such an effect. In the vibrational ground state, the nuclear wave function is symmetric. However the measurement of a single photoionization event at an individual molecule can find the molecule at asymmetric bond length. In such a case, the symmetry is broken by different C–O bond lengths on each side, and subsequent Auger decay makes it more likely for the longer bond to break. The MFPAD itself will be asymmetric, since the photoelectron wave is multiply scattered in an asymmetric potential. Liu *et al.* presented calculations for different bond lengths which produce similar asymmetries. This speculative interpretation was confirmed by more elaborate theoretical work by Miyabe *et al.* [34], also considering the potential energy surfaces on which the asymmetric fragmentation proceeds. Nevertheless, independent experimental evidence for the proposed scenario was missing.

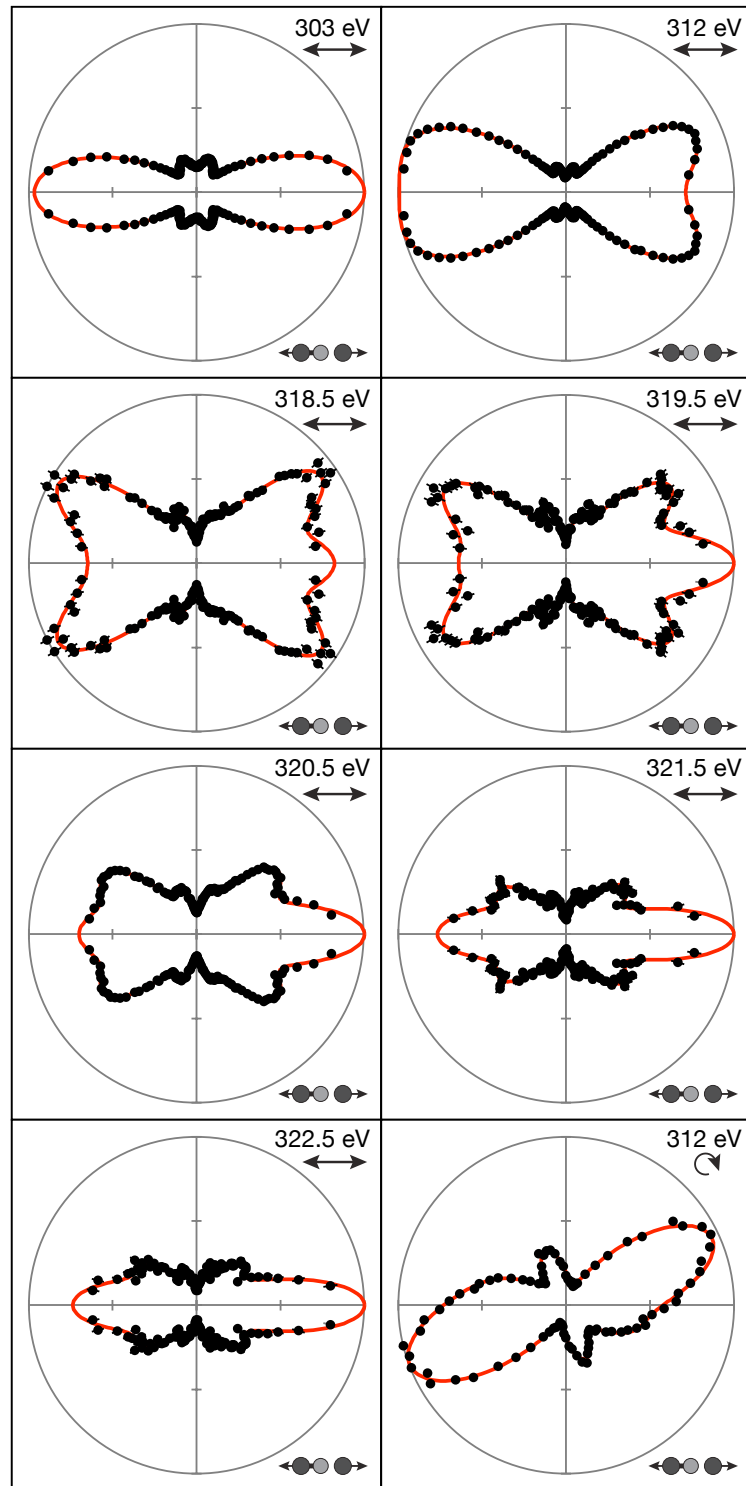


**Figure 5.5:** *MFPADs* at energies of 303–322.5 eV above the carbon  $K$ -shell threshold with horizontal polarization and at 312 eV with circularly polarized light. The molecular axis is horizontal in the plots with the  $0^+$  ion to the right. The angular distributions at 312 and 320.5 eV, where shape-resonances are located, show a higher intensity for emission towards the  $CO^+$ -ion. At circular polarization, the effect is weaker due to a higher contribution of the  $\Pi$ -transition perpendicular to the molecular axis. The solid lines are fits of the data with spherical harmonics up to  $l=5$ .

The present measurement does not only confirm the asymmetry observed by Liu *et al.*, but in addition it gives a direct experimental proof for the proposed mechanisms by relating the MFPAD to the measured kinetic energy release (KER) of the fragments.

In the following, three alternatives are discussed as a possible cause for the asymmetric angular distribution as suggested by Liu *et al.*: post collision interaction, initial state correlation and bond length asymmetry. Since in this experiment in addition to the photoelectron, the Auger electron and the KER are measured in coincidence, these hypotheses can be tested directly.

### 5.3.1 Post collision interaction

*Post collision interaction (PCI)* describes the coupling of the fast Auger electron to the much slower photoelectron in the final state. In the present case, one could imagine that Auger decay from a valence orbital breaks the initial symmetry and leads to a preferred breakup of the bond from which the electron was ejected. If the Auger electron interacts with the photoelectron after emission, the originally symmetric photoelectron angular distribution would be modified and inherit some of the asymmetry of the Auger emission. In a recent work on neon 1s photoionization followed by Auger decay [25], it has been shown that PCI can play an important role at low photoelectron energies. We can check the influence of this mechanism directly by inspecting our MFPADs for different Auger electron emission direction. If the asymmetry in the MFPAD were due to the imprint of asymmetric Auger decay, it should disappear for Auger emission perpendicular to the molecular axis, as in this case both directions along the molecular axis are affected equally. The blue line in Fig. 5.6 (a) shows the data for this geometry where the influence of PCI is switched off. Clearly, the asymmetry is still present, showing that another mechanism than PCI is responsible for the symmetry breaking. Fig. 5.6 (b) reveals, however, that PCI does exist but it is not the cause for the asymmetry. The ringlike distribution shows emission intensity at all angles between photo and Auger electron. There is a small but significant suppression of flux for both electrons emitted in the same direction (see [25]). This suppression of flux for parallel emission does influence the MFPAD also when the Auger electron is selected parallel or antiparallel to the CO<sup>+</sup>-O<sup>+</sup> axis as shown by the red and green line in Fig. 5.6 (a) (compare curves at  $\cos(\theta) = 1$ ).

### 5.3.2 Initial state correlation

*initial state correlation* are now discussed as a possible cause of the asymmetry. This model is based on the assumption that the single orbital picture is incomplete, neglecting an important part of electron correlation. In the two-step model as introduced above, one considers the photoelectron ejection from the C(1s) orbital and independent of that subsequent relaxation. This happens via Auger transition between well defined molecular orbitals. Electron correlation in the bound state does mix orbitals. It might also couple photoelectron and Auger electron similarly as PCI does via electron-electron interaction in the continuum state. With our experiment, we are able to look at dependencies between photoelectron and Auger electrons. The data did not provide any evidence for important correlation or dependency of photoelectrons and Auger electrons (see Fig. 5.7) beyond what is shown in Fig. 5.6 (b). This is also expected, since the energy difference between the involved orbitals is rather big. For small energy spacings, like the g/u splitting of N<sub>2</sub> or Ne<sub>2</sub> such couplings are big and lead to spectacular changes of the MFPAD as a function of the Auger emission angle [47, 23, 60]. Similarly, intermediate resonances have been reported to lead to large asymmetries [31]. In the present case of CO<sub>2</sub>, there are no such resonances involved.

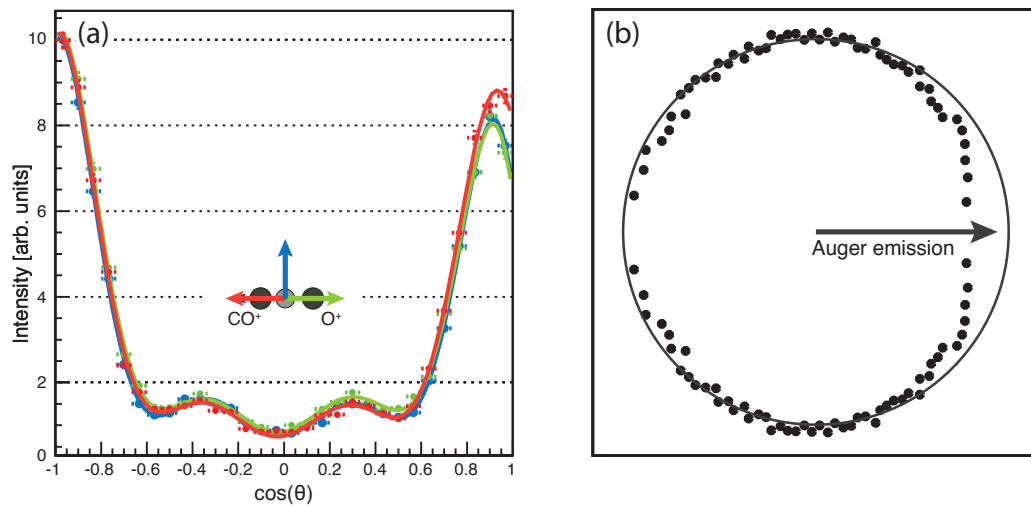


**Figure 5.6:** (a) MFPADs for fixed Auger ejection angles ( $\gamma=312$  eV, horiz. polariz., normalized to the maximum): red line - Auger emission towards  $\text{CO}^+$ ; green line - Auger emission towards  $\text{O}^+$ ; blue line - Auger emission perpendicular to the molecular axis. The blue distribution proves that PCI does not cause the asymmetry along the molecular axis. Figure (b) shows a polar plot of the photoelectron intensity for varying angle between photoelectron and Auger electron. The arrow represents the direction of the Auger electron, which is fixed in this plot to the right.

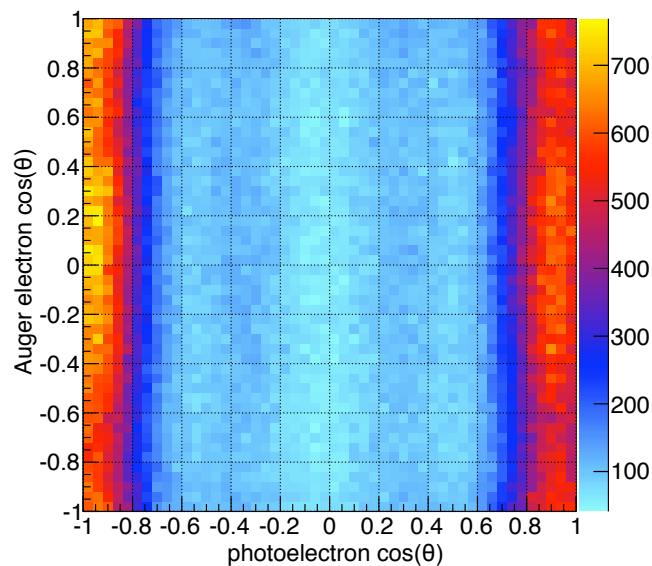


**Figure 5.7:** Comparison of emission intensity of the photoelectron and Auger electron at  $\cos(\theta)$  to the molecular axis. The plot does not exhibit a dependence of the two parameters. The photoelectron distribution does not change its shape at different  $\cos(\theta)$ -values of the Auger electron. The variations in intensity at different Auger angles are displayed more clearly in Fig. 5.6 (b).

### 5.3.3 Vibrational modes

The third possibility of causing an asymmetric MFPAD is an asymmetry in the molecular geometry at the instant of photoelectron ejection, as outlined in Sec. 5.2. On average, carbon dioxide is a linear molecule, and both C–O bonds have the same length. However, asymmetric stretching of the molecular bonds provides a distribution of bond lengths where only the peak represents a symmetric molecule (see Fig. 2.3 on page 15). In cases when the ejection of the photoelectron occurs at non-equal C–O bond length, the interference pattern of the electron wave diffracted in the asymmetric molecular potential will be asymmetric. Since the Auger decay is on the same time scale (Auger lifetime:  $\sim 6$  fsec [9]) as the asymmetric stretch motion (quarter period 3.55 fsec [34]), the asymmetric bond length at the instant of photoabsorption could finally lead to a preferred side for the bond breakage after Auger emission.

Our approach to prove molecular distances as the result of asymmetric MFPADs is to seek for differences in the angular distributions as a function of the kinetic energy release. The KER is the sum of the kinetic energies of all ions after breakup due to the coulombic potential between the charged ions (see Equ. 4.16). Its distribution reflects the transition of the core-hole state to the final state and depends on the internuclear distance at breakup time. In this sense, the KER can be used as a measure of the internuclear distance. Nevertheless, we have to consider that several repulsive final states are populated, and the measured KER distribution is always a mixture of the different final state distributions. Different KERs can therefore be due to different internuclear distances and dissociation along different  $\text{CO}_2^+$  potential energy surfaces. The measurement of internuclear distance by detecting the KER is based on the *reflection approximation*<sup>1</sup> (see e.g. [15]). It has been pioneered in coulomb explosion imaging in ion beams [55] and is routinely used with strong laser fields today (see e.g. [27]). We apply this idea here to measure the internuclear distance for each single event with a precision much better than the width of the nuclear ground state wave function. The coincident detection of KER and electron momentum allows to select, from the ground state wave function, a subsample of molecules which had a particular internuclear distance at the instant of the electronic transition. This technique was demonstrated previously for coherent Rutherford scattering [45]. For photo-doubleionization of  $H_2$  with the same technique, it has been shown that correlated electron emission [58] and electron refraction [22, 2, 48] depend on the internuclear distance [54].

In the data, a small but significant dependence of the asymmetry with respect to the KER can be found. Fig. 5.8 demonstrates the observed changes. The kinetic energy release is shown in (f) with three regions marked. In (a), the photoelectron angle to the molecular axis is plotted for KER values of 6.5, 8.5 and 10.5 eV, but only small variations are visible. However, a closer look at the  $\cos(\theta)$  range of -0.6–0.6 at these KER values in Fig. 5.8 (b)–(d) the small f-wave lobes shows the variations: from KER 6.5 eV to 10.5 eV, these two peaks around orthogonal emission from contributions of angular momentum  $l=4$  exhibit a switching of the asymmetry. The intensity is higher for photoelectron emission at negative  $\cos(\theta)$  for KER values below 9 eV, whereas the peak at positive  $\cos(\theta)$  becomes higher above this value. The graph in (e) displays the changes for the whole range of KER for the main peaks at emission along the molecular axis (solid line) and for the small f-wave peaks (dashed line). A decrease in the asymmetry for the emission along the molecular axis from 20 % to about 10 % can be observed for rising KER together with a switching of the asymmetry of the f-wave lobes.

<sup>1</sup>This method is a theoretical approximation for calculation of *Franck-Condon factors*, involving the replacement of the continuum wavefunction by a normalized  $\delta$ -function at the classical turning point of the upper state in the transition.

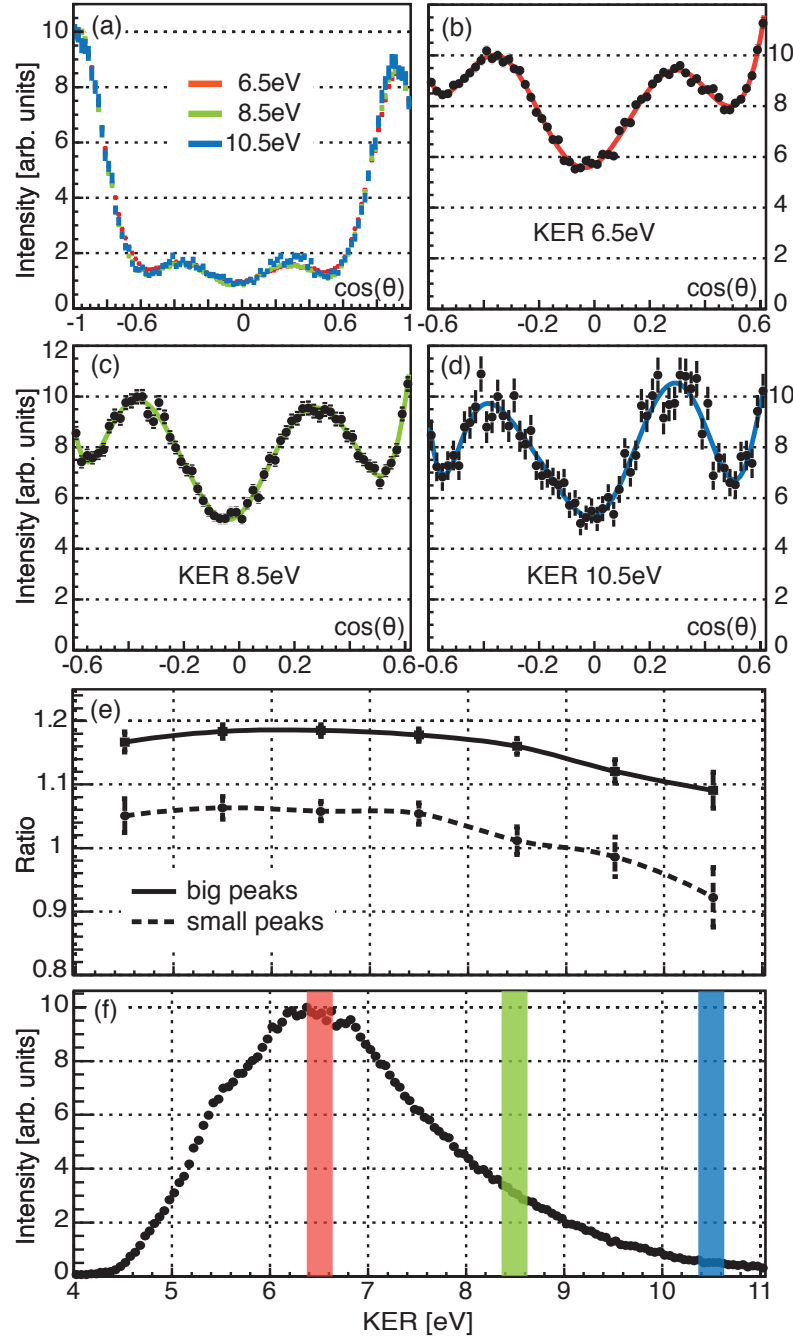


**Figure 5.8:** MFPADs for different kinetic energy releases (KER) ( $\gamma=312$  eV, horiz. polariz.). In (a)–(d), the cosine of the angle to the molecular axis is plotted. Positive values correspond to the direction of the  $\text{O}^+$ . In panel (a) we can see only small changes in the MFPAD for different KERs. However, a closer inspection of the small lobes from f-wave contributions (b),(c),(d) reveals a swapping of the asymmetry from the  $\text{CO}^+$  to the  $\text{O}^+$  side at higher KER. (e) shows the ratio of the maximum of left to right peak as a function of KER. The solid curve represents the ratio of the main peaks, while the dotted line represents the small features at  $\cos(\theta) = \pm 0.35$ , illustrating the evolution of the asymmetry with the molecular bond length. (f) shows the KER spectrum, regions chosen for the data in (b),(c) and (d) are marked in the particular color.

In the theoretical model calculated by Miyabe *et al.* [34], such a shift for different bond lengths is predicted as well.

In order to obtain the effect from asymmetric molecular geometry, the doubly charged  $\text{CO}^{++}$  ion has to dissociate promptly into the  $\text{CO}^+$  and  $\text{O}^+$  fragments. Miyabe *et al.* [34] propose the  $3^1\Pi$  state as the populated that that leads to asymmetric dissociation (see Fig. 5.9). We conclude that indeed asymmetries in the initial geometry of the molecule create the observed asymmetric MFPAD.

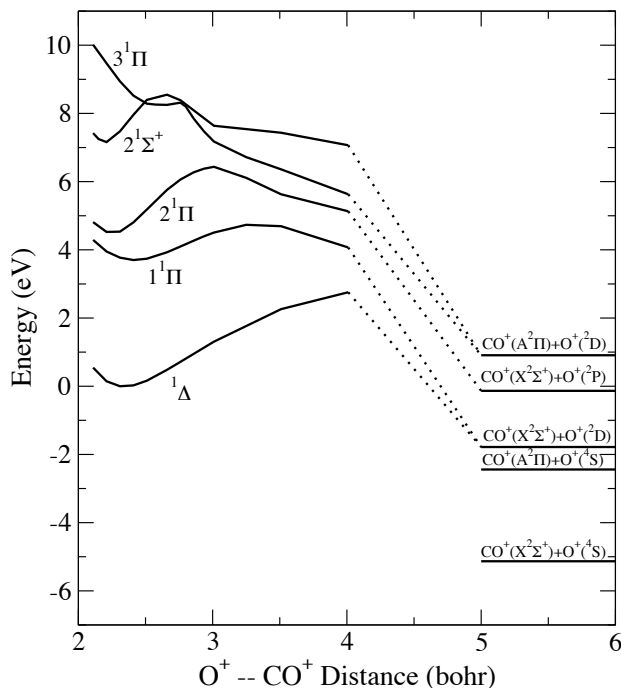


**Figure 5.9:** Potential energy curves of the  $\text{CO}_2^{++}$  ion from calculations by Miyabe *et al.* [34]. They propose the  $3^1\Pi$  state as the pathway leading to asymmetric dissociation, as it is the only singlet state that has a small potential barrier at equilibrium distance (2.2 a.u.).

## 5.4 Auger electron angular distributions

In this work the first Auger electron angular distributions of fixed-in-space  $\text{CO}_2$  are presented. Such angular distributions are known to be a rich source of information on the states involved as well as on the molecular potential from which the Auger electrons escape. The shape of the initial and final state orbital is imprinted onto the Auger angular distribution [61, 7, 41]. As a consequence, the angular distributions for  $\Sigma$  and  $\Pi$  transitions are preferentially along or perpendicular to the bond. In addition, the multiple scattering of the Auger electron in the molecular potential leads to interference effects in the angular distributions of the Auger electron [57, 61].

Therefore, one might expect that an asymmetry would be present in the Auger angular distribution, like it is seen in the MFPAD in Fig. 5.5. Since the bond breakage is directly associated with the emission of the Auger electron, any correlation of its angular distribution with the site at which the C–O bond breaks can be expected to be even stronger than for the photoelectron.

Nevertheless, our measured angular distributions shown in Fig. 5.11 display only a rather weak asymmetry. The angular distribution in general is close to isotropic. Our data do not exhibit a significant dependence of this small asymmetry on the photon energy (see Fig. 5.10). They rather indicate that it is the shape resonance which enhances the asymmetry effect, and for electron energies of photo- and Auger electrons much above the shape resonance, the asymmetries are rather small.

The Auger electron angular distribution contains contributions from  $\Sigma$ - and  $\Pi$ -states. The mixing of these states changes however with the KER, as seen in Fig. 5.11. At low kinetic energy releases, the distribution is almost isotropic with equal intensity of Auger electron emission along and perpendicular to the molecular axis. At KER values of 6–9 eV, a weak asymmetry along the molecular axis can be observed which is likely to reflect the effect observed in the MFPADs. Above KER=6 eV, there are rising contributions from higher order angular momentum, yielding small lobes around  $\cos(\theta) = \pm 0.35$  as seen in the MFPAD. At larger KER, the distribution exhibits significantly more intensity along the molecular axis, indicating a stronger contribution of  $\Sigma$ -states.

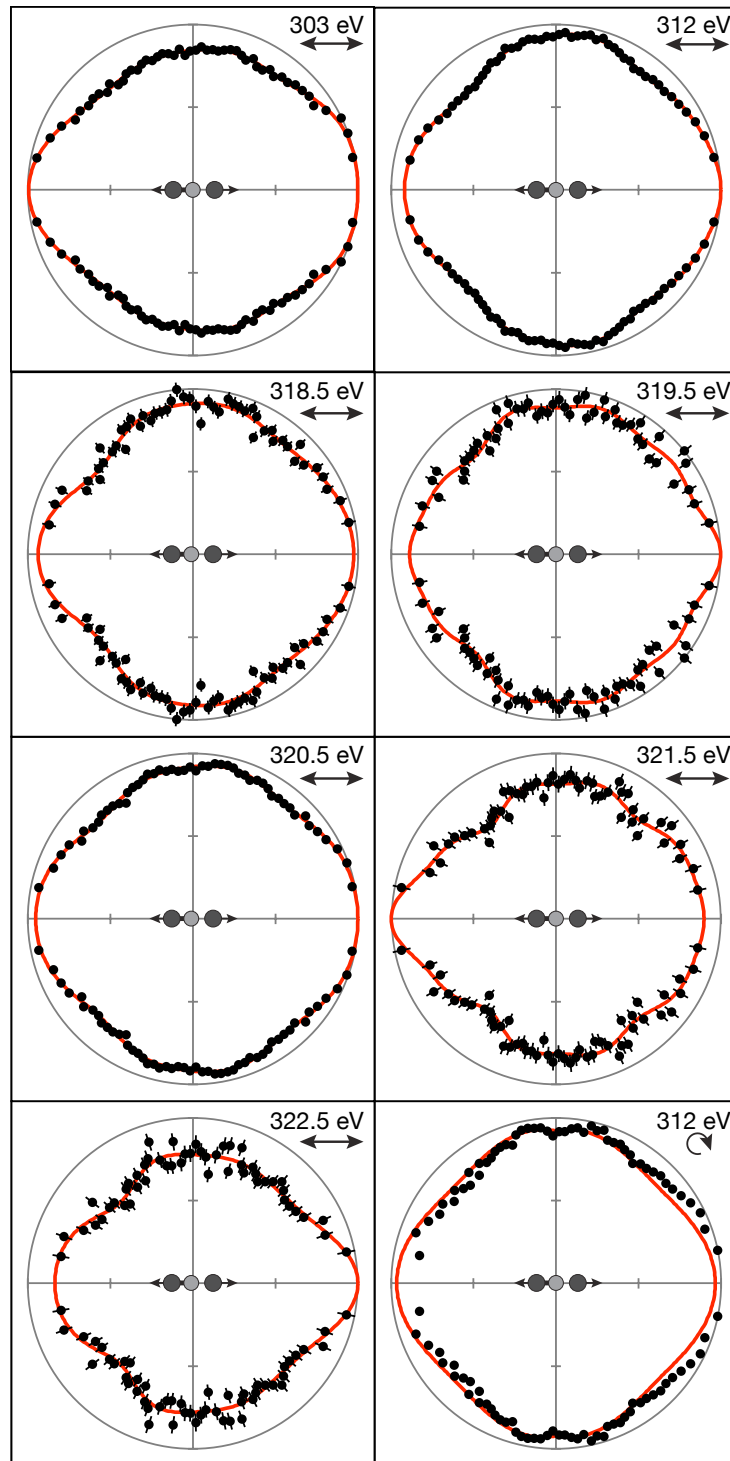


**Figure 5.10:** Auger electron angular distributions with at photon energies of 303–322.5 eV with horizontally polarized light and at 312 eV with circular polarization. The solid lines are fits of the data with spherical harmonics up to  $l=5$ . There is no significant asymmetry with respect to the  $\text{CO}^+$  and  $\text{O}^+$  ions observed as in the MFPADs. The distributions are nearly isotropic at all energies and contributions of partial waves from different angular momenta change only slightly.

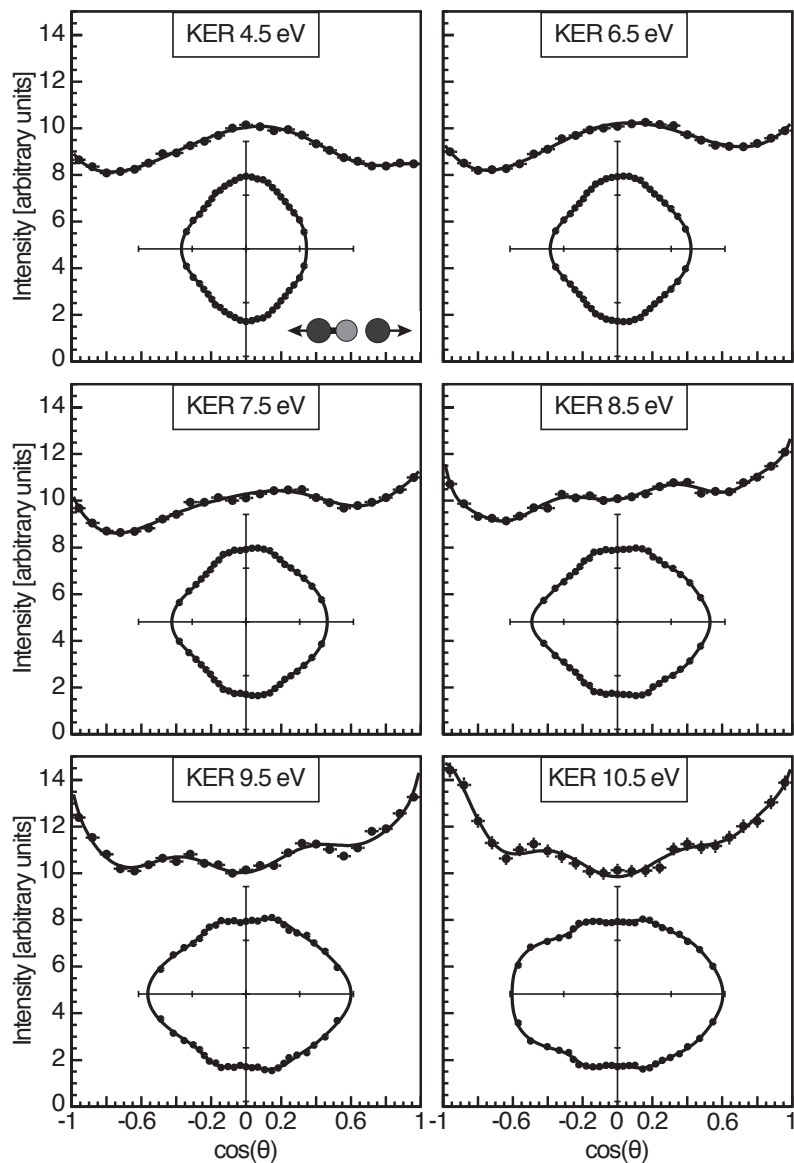


**Figure 5.11:** Auger electron angular distributions for different KER at 312 eV photon energy with horizontal polarization. The insets show the distribution as a polar plot where the molecular axis is fixed horizontally. The distribution reflects the selection of Auger final states for different KER. At lower KER, mainly  $\Pi$ -states contribute whereas  $\Sigma$ -states gain more weight at higher KER, shifting intensity to Auger electron emission along the molecular axis. Intensity is normalized to  $\cos(\theta) = 0$ . The solid lines are fits by spherical harmonics up to  $l=5$ . The KER regions have a width of  $\pm 1.5$  eV.



# 6 Summary and Outlook

## 6.1 Summary

In the present work a kinematically complete experiment of two-step double photoionization of  $\text{CO}_2$  followed by fragmentation into  $\text{CO}^+ + \text{O}^+$  has been presented. Using COLTRIMS technique, we measured the photoelectrons and the ionic fragments after carbon core-hole ionization. Improvements in the momentum resolution on the recoil ions, especially the use of an electrostatic lens, allowed us to reconstruct the momenta of all particles, including the Auger electron. Our photoelectron angular distributions reach an unprecedented level of precision. Auger electron angular distributions of  $\text{CO}_2$  are reported for the first time.

The main focus in this experiment was on an asymmetry of the photoelectron angular distribution first reported by Liu *et al.* [30]. The angular distribution of the photoelectron emitted from the central carbon  $1s$  shell shows an asymmetry with respect to the  $\text{O}^+$  and  $\text{CO}^+$  fragments. Inspecting MFPADs at different kinetic energy releases, we provided direct experimental evidence that varying C–O bond lengths cause this asymmetry. The high resolution measurements revealed new details in the MFPADs produced by higher angular momenta.

Initial state correlation effects, as seen in experiments with other molecules, were not observed. The Auger electron angular distributions in the molecular frame are nearly isotropic and do not show a strong structure. Slightly varying distributions in dependence of the kinetic energy release were attributed to varying contributions of electronic states with different symmetry.

Our data show clearly a link between photo and Auger electron in form of post-collision interaction (PCI), as well as a dependence of photo and Auger electron on the nuclear motion and on asymmetries in the dissociation. The details revealed in our study are only partly matched by theoretical calculations which calls for a unified theoretical treatment of photoemission, Auger decay and nuclear motion.

## 6.2 Outlook

The high resolution on the ions cannot be beaten with presently available techniques which makes this set of data unique. A further subject of investigation could be the analysis of three-body breakup channels obtained in the experiment. The geometry of  $\text{CO}_2$  at fragmentations into  $\text{O}^+ + \text{C}^+ + (\text{O})$  and  $\text{O}^+ + (\text{C}) + \text{O}^+$  could be compared to investigations of three-body breakup in ion-molecule collisions.

An additional view of the reaction would be the separation of vibrational levels of the photoelectron. In this measurement, the energy resolution of the electrons and the photons was not sufficient for separating different vibrational modes of the molecule. A new experiment with improved electron resolution could provide this information.

A high resolution measurement of the Auger electron energy as well as the KER would allow the determination of the doubly excited states the Auger was ejected from. In this case, it would be possible to see the geometry of the states involved and we could proof the assumption that the dependence of the Auger electron angular distribution on the KER is due to a mixing of Auger states.

Nevertheless, a significantly improved resolution of the Auger electron energy together with photoelectron and KER measurement is not possible at this time. Only a bigger setup would allow us to decrease the electric field and improve hereby the resolution. Another way of improving the resolution of the Auger electrons would be a completely new setup, where we measure the Auger electrons directly on a big electron detector and build a small recoil side. The setup would provide full solid angle of the ions and the photoelectrons, but only a small solid angle of Auger electrons. The Auger electron resolution would be much improved in the position directions, but the resolution in TOF direction would be very small.

The impact of vibrational modes on the angular distributions of photo and Auger electrons should be investigated in other systems as well. One should find similar asymmetry effects in linear molecules after core hole ionization at the central atom. In asymmetric molecules, there might be an impact of molecular modes which has not been taken into account in the theoretical descriptions so far.

# Photo and Auger Electron Angular Distributions of Fixed-in-Space CO<sub>2</sub>

Diplomarbeit von Felix Paul Sturm

## Zusammenfassung

In der vorliegenden Arbeit wird ein kinematisch vollständiges Experiment zur Zwei-Stufen-Doppelphotoionisation von CO<sub>2</sub> mit anschließender Fragmentation in CO<sup>+</sup> und O<sup>+</sup> vorgestellt. Unter Nutzung der COLTRIMS Technik wurden die Photoelektronen sowie die ionischen Fragmente nach K-Schalen-Ionisation gemessen. Verbesserungen in der Impulsauflösung der Rückstoßionen, besonders durch den Einsatz einer elektrostatischen Linse, ermöglichten die Rekonstruktion aller Teilchen einschließlich des Augerelektrons. Die gemessenen Winkelverteilungen der Photoelektronen erreichen ein bisher unerreichtes Niveau an Genauigkeit. Augerelektronen-Winkelverteilungen von CO<sub>2</sub> werden zum ersten Mal überhaupt präsentiert.

Das Hauptaugenmerk dieses Experiments war auf eine Asymmetrie in der Photoelektronen-Winkelverteilung gerichtet, von der erstmals durch Liu *et al.* [30] berichtet worden war. Die Winkelverteilung der vom zentralen Kohlenstoff-1s-Orbital emittierten Photoelektronen zeigt eine Asymmetrie zur Richtung der CO<sup>+</sup> bzw. der O<sup>+</sup> Fragmente. Durch Untersuchung der Photoelektron-Winkelverteilungen im molekülfesten Koordinatensystem (MFPAD) bei verschiedener kinetischer Energie der atomaren Fragmente (KER) konnten direkte experimentelle Hinweise dafür gefunden werden, dass variierende C–O-Bindungslängen die beobachtete Asymmetrie verursachen. Unsere hochauflösenden Messungen zeigen ferner neue, durch höhere Drehimpulse hervorgerufene Details in den MFPADs.

Hinweise auf eine Korrelation der Anfangszustände, wie in anderen Experimenten mit Molekülen beobachtet, wurden nicht gefunden. Die Winkelverteilungen der Augerelektronen im molekülfesten Koordinatensystem zeigen keine ausgeprägte Struktur, sondern sind annähernd isotrop. Leichte Änderungen der Winkelverteilungen in Abhängigkeit vom KER werden sich ändernden Beiträgen verschiedener elektronischer Zustände mit unterschiedlicher Symmetrie zugesprochen.

Unsere Daten zeigen einen deutlichen Zusammenhang zwischen Photo- und Augerelektronen in Form von *Post-Collision Interaction (PCI)*, sowie eine Abhängigkeit beider von der Kernbewegung und Asymmetrien in der Dissoziation. Die in dieser Arbeit aufgedeckten Details legen eine vereinheitlichte theoretische Behandlung von Photoemission, Augerzerfall und Kernbewegung nahe.



# Appendix

## 1 Three-dimensional linear interpolation

Let  $\mathbf{X}(\mathbf{x}, \mathbf{y}, \mathbf{z})$  be the point where the interpolation is to be performed and  $\mathbf{f}(\mathbf{a}_i, \mathbf{b}_j, \mathbf{c}_k)$  the obtained correction values. Let  $\mathbf{a}_1, \mathbf{a}_2, \dots$  be the tabulated grid line positions of  $x$ ,  $\mathbf{b}_1, \mathbf{b}_2, \dots$  the tabulated lines of  $y$  and  $\mathbf{c}_1, \mathbf{c}_2, \dots$  the lines of  $z$ .

Let  $\mathbf{i}, \mathbf{j}$  and  $\mathbf{k}$  be the subscripts  $\mathbf{a}_i \leq \mathbf{x} < \mathbf{a}_{i+1}$ ,  $\mathbf{b}_j \leq \mathbf{y} < \mathbf{b}_{j+1}$  and  $\mathbf{c}_k \leq \mathbf{z} < \mathbf{c}_{k+1}$ .

$$t = \frac{(x - a_i)}{(a_{i+1} - a_i)}$$

$$g_{j,k} = (1 - t)f(a_i, b_j, c_k) + tf(a_{i+1}, b_j, c_k)$$

$$g_{j+1,k} = (1 - t)f(a_i, b_{j+1}, c_k) + tf(a_{i+1}, b_{j+1}, c_k)$$

$$g_{j,k+1} = (1 - t)f(a_i, b_j, c_{k+1}) + tf(a_{i+1}, b_j, c_{k+1})$$

$$g_{j+1,k+1} = (1 - t)f(a_i, b_{j+1}, c_{k+1}) + tf(a_{i+1}, b_{j+1}, c_{k+1})$$

$$u = \frac{(x - b_j)}{(b_{j+1} - b_j)}$$

$$h_k = (1 - u) \cdot g_{j,k} + u \cdot g_{j+1,k}$$

$$h_{k+1} = (1 - u) \cdot g_{j,k+1} + u \cdot g_{j+1,k+1}$$

$$v = \frac{(z - c_k)}{(c_{k+1} - c_k)}$$

$$\mathbf{f}(\mathbf{x}, \mathbf{y}, \mathbf{z}) = (1 - v) \cdot h_k + v \cdot h_{k+1} \quad (\text{Interpolated correction value})$$

## 2 Vacuum data

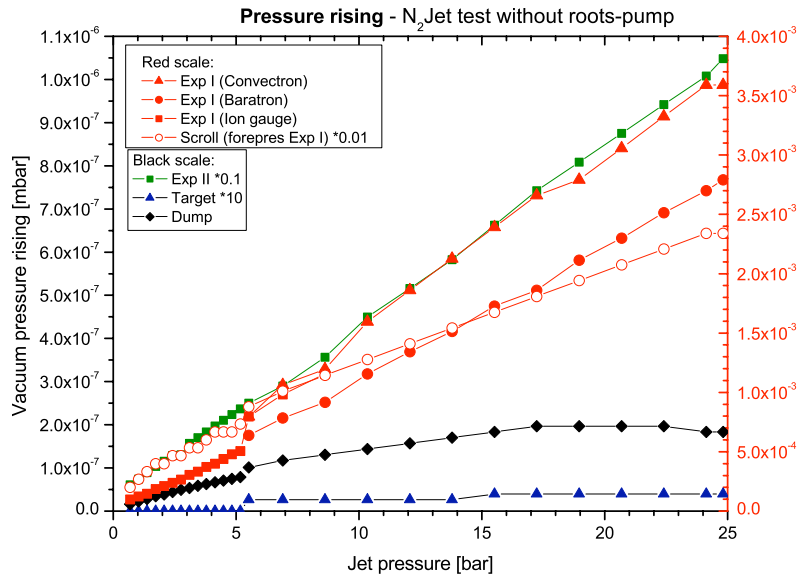


**Figure 1:** Rising of the vacuum pressures for different driving pressures of the gas jet. The red solid dots show measurements using different gauges as the monitored range is in between the ranges for convectron and ion gauges.

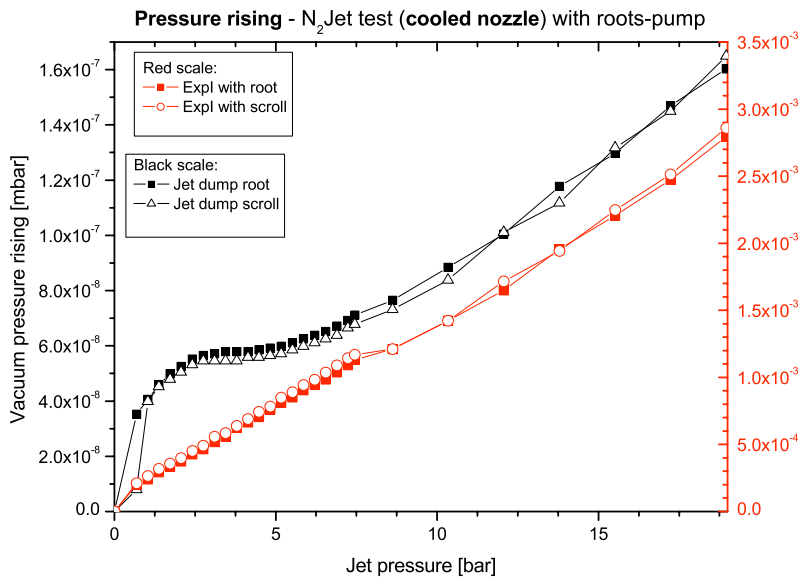


**Figure 2:** Vacuum pressure rising in the jet dump at different driving pressures of the jet. The measurement was performed in order to check whether the use of an additional roots pump connected to the turbo pump in the source would increase vacuum quality. The solid dots are obtained using the roots pump, the hollow markers represent data where only a scroll pump was used. The black lines show the pressure rising in the jet dump. Above  $\sim 7$  bar driving pressure, the supersonic jet collapses, indicated by a linear rise in the jet dump after saturation.

### 3 Statistical errors

Let  $P(x)$  be a probability distribution of independent values  $x_1, x_2, \dots, x_i$  and  $\langle x \rangle = E$  the expectation value. We define the sum  $S = \sum_{i=1}^N x_i$ . The expectation value of  $S$  is then:<sup>1</sup>

$$\langle S \rangle = \sum_{i=1}^N \langle x_i \rangle = N \cdot E$$

The variance as a measure for the error is defined as:  $Var(x) = \sigma_x^2$

$$\begin{aligned} \sigma_x^2 &= \langle (x - \langle x \rangle)^2 \rangle \\ &= \langle x^2 \rangle - 2\langle x \rangle \langle x \rangle + \langle x \rangle^2 = \langle x^2 \rangle - \langle x \rangle^2 \\ &= \langle x^2 \rangle - E^2 \end{aligned}$$

$$\begin{aligned} Var(S) &= \langle S^2 \rangle - \langle S \rangle^2 \\ &= \langle \sum_{i,j} x_i x_j \rangle - N^2 E^2 \\ &= \langle \sum_{i=1}^N x_i^2 \rangle + \sum_{i,j \ i \neq j} \langle x_i \rangle \langle x_j \rangle - N^2 E^2 \\ &= \sum_{i=1}^N (\sigma_x^2 + E^2) + (N^2 - N)E^2 - N^2 E^2 \\ &= N\sigma_x^2 \end{aligned}$$

We see that the error  $\sigma_a$  of the variable  $a = \frac{S}{N}$  (the measurement of value  $a$ ) depends on the error of each measurement  $x_i$  by:

$$\sigma_a = \frac{1}{\sqrt{N}} \cdot \sigma_x$$

---

<sup>1</sup>For reference see [6] and [37].

## 4 The chamber at BL 11.0.2

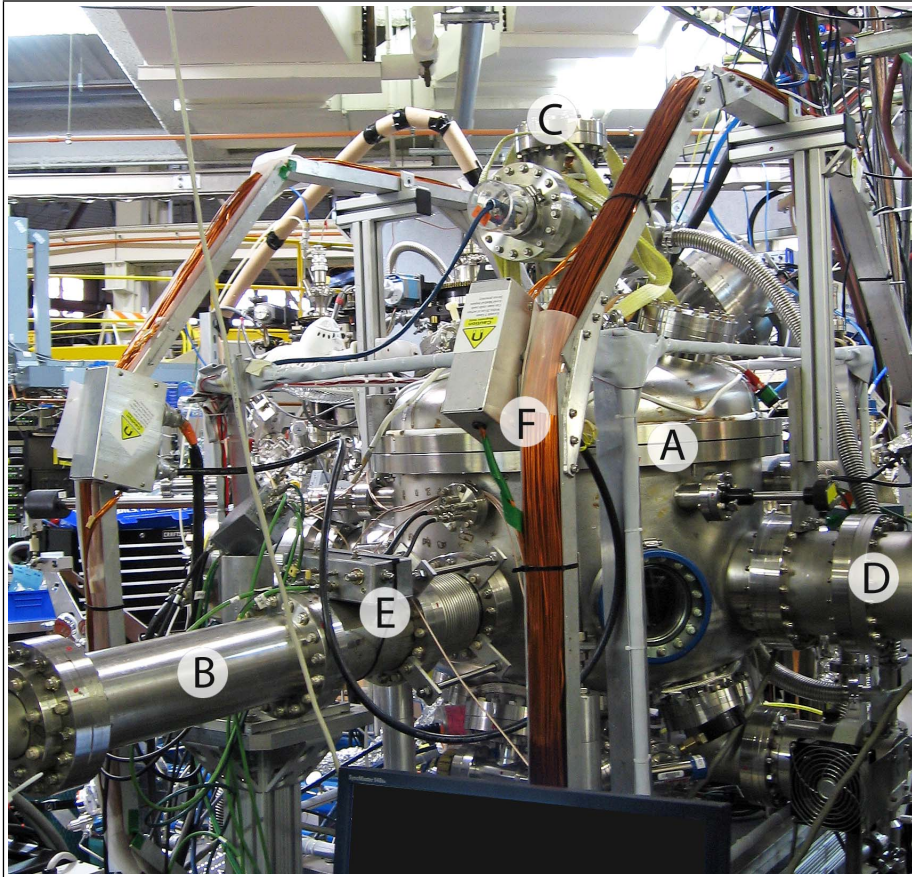


**Figure 3:** Photograph of the *COLTRIMS* setup at beamline 11.0.2 at the *Advanced Light Source (ALS)*. Coming from behind the apparatus, the photon beam crosses a differential pumping stage, reaches the reaction zone in the chamber (A) and is finally blocked in (B). The gas jet is injected at the lower part of the chamber and travels vertically up until it reaches the jet dump (C). At (D), we can see the extension of the chamber containing the long drift tube of the recoil side. A *decoupling box* (see Sec. 3.4.1) is labelled with (E) and right beside it, one of the big Helmholtz-coils creating the magnetic field for guiding the electrons is marked with (F). The gray wire frame (between (F) and (A)) is an additional spool compensating outer fields.

## 5 Atomic Units

In order to simplify calculations, a different unit system is common in atomic physics. Conversion factors can be found in the following table.

dimension	formula	SI units
mass	$m_e$	$9.10938 \cdot 10^{-31}$ kg
charge	$e$	$1.60218 \cdot 10^{-19}$ C
length	$a_0$	$5.29177 \cdot 10^{-11}$ m
velocity	$v_0$	$2.18769 \cdot 10^6$ m s <sup>-1</sup>
time	$a_0/v_0$	$2.41888 \cdot 10^{-17}$ s
momentum	$m_e v_0$	$1.99285 \cdot 10^{-24}$ kg m s <sup>-1</sup>
angular momentum	$\hbar = a_0 m_e v_0$	$1.05457 \cdot 10^{-34}$ kg m <sup>2</sup> s <sup>-1</sup>
frequency	$v_0/(2\pi a_0)$	$6.57969 \cdot 10^{15}$ Hz
angular frequency	$v_0/a_0$	$4.13414 \cdot 10^{16}$ Hz
energy	$e^2/(4\pi\epsilon_0 a_0)$	27.2116 eV = 1 hartree
action	$\hbar = e^2/(4\pi\epsilon_0 v_0)$	$1.05457 \cdot 10^{-34}$ J s
electric field	$e/(4\pi\epsilon_0 a_0^2)$	$5.14221 \cdot 10^{11}$ V/m
magnetic field	$\hbar/(e a_0^2)$	$2.35052 \cdot 10^5$ T
intensity	$1/2 c \epsilon_0 (e/(4\pi\epsilon_0 a_0^2))^2$	$3.50953 \cdot 10^{16}$ W/cm <sup>2</sup>

constant	formula	SI units	atomic units
Planck's constant	$h$	$6.62608 \cdot 10^{-34}$ J s	$2\pi$
elementary charge	$e$	$1.60218 \cdot 10^{-19}$ C	1
electron mass	$m_e$	$9.10938 \cdot 10^{-31}$ kg	1
proton mass	$m_p$	$1.67262 \cdot 10^{-27}$ kg	1836.15
atomic mass unit	$amu = \frac{1}{12} m(^{12}C)$	$1.66054 \cdot 10^{-27}$ kg	1822.89
velocity of light	$c$	$2.99792 \cdot 10^8$ m/s	137.04
influence constant	$\epsilon_0$	$8.85419 \cdot 10^{-12}$ As/(Vm)	$1/(4\pi)$
induction constant	$\mu_0 = 1/(c^2 \epsilon_0)$	$4\pi \cdot 10^{-7}$ Vs/(Am)	$4\pi/137.04^2$

From [52].



# Bibliography

- [1] H. Ågren. On the interpretation of molecular valence Auger spectra. *The Journal of Chemical Physics*, 75:1267, 1981. URL <http://link.aip.org/link/?JCPA6/75/1267/1>.
- [2] D. Akoury, K. Kreidi, T. Jahnke, T. Weber, A. Staudte, M. Schöffler, N. Neumann, J. Titze, L. P. H. Schmidt, A. Czasch, O. Jagutzki, R. A. C. Fraga, R. E. Grisenti, R. D. Muino, N. A. Cherepkov, S. K. Semenov, P. Ranitovic, C. L. Cocke, T. Osipov, H. Adaniya, J. C. Thompson, M. H. Prior, A. Belkacem, A. L. Landers, H. Schmidt-Bocking, and R. Dörner. The Simplest Double Slit: Interference and Entanglement in Double Photoionization of H<sub>2</sub>. *Science*, 318(5852):949–952, 2007. doi: 10.1126/science.1144959. URL <http://dx.doi.org/10.1126/science.1144959>.
- [3] P. W. Atkins. *Molecular quantum mechanics*. Oxford University Press, Oxford/New-York, 3rd edition, 1997.
- [4] P. Auger. The effect of a photoelectric compound. *Journal de Physique et le Radium*, 6:205–U12, 1925. ISSN 0368-3842.
- [5] D. Beck and H. Förster. Rotationsanregung in molekularen Stößen. *Zeitschrift für Physik A Hadrons and Nuclei*, 240(2):136–152, 1970. URL <http://www.springerlink.com/content/m1v48q201417k060/fulltext.pdf>.
- [6] U. Bissbort. Statistical mathematics. personal discussion, April 2009.
- [7] S. Bonhoff, K. Bonhoff, and K. Blum. Angular distribution of auger electrons emitted by co molecules. *J. Phys. B*, 32(5):1139–1149, 1999. URL <http://stacks.iop.org/0953-4075/32/1139>.
- [8] G. Brusdeylins and H. Meyer. Speed ratio and change of internal energy in nozzle beams of polyatomic gases. In *Rarefied gas dynamics; Proceedings of the Eleventh International Symposium, Cannes, France, July 3-8, 1978*, volume 2, 1979.
- [9] T. X. Carroll, J. Hahne, T. D. Thomas, L. J. Sæthre, N. Berrah, J. Bozek, and E. Kukk. Carbon 1s core-hole lifetime in co<sub>2</sub>. *Phys. Rev. A*, 61(4):042503, Mar 2000. doi: 10.1103/PhysRevA.61.042503. URL <http://dx.doi.org/10.1103/PhysRevA.61.042503>.
- [10] C. Cohen-Tannoudji, B. Diu, and F. Laloë. *Mécanique quantique*, volume 1. Hermann, éditeurs des sciences et des arts, 1973, tirage 1998.
- [11] A. De Fanis, N. Saito, A. A. Pavlychev, D. Y. Ladonin, M. Machida, K. Kubozuka, I. Koyano, K. Okada, K. Ikejiri, A. Cassimi, A. Czasch, R. Dörner, H. Chiba, Y. Sato, and K. Ueda. Symmetry-dependent multielectron excitations near the c 1s ionization threshold and distortion of the shape resonance in co<sub>2</sub>. *Phys. Rev. Lett.*, 89(2):023006, Jun 2002. doi: 10.1103/PhysRevLett.89.023006. URL <http://dx.doi.org/10.1103/PhysRevLett.89.023006>.

- [12] A. De Fanis, N. Saito, K. Okada, M. Machida, I. Koyano, A. Cassimi, R. Dorner, A. Pavlychev, and K. Ueda. Satellite excitations due to internal inelastic scattering in the K-shell photoemission from CO<sub>2</sub>. *J. Electron Spectrosc. Relat. Phenom.*, 137(Sp. Iss. SI):265–269, JUL 2004. ISSN 0368-2048. doi: 10.1016/j.elspec.2004.02.061. URL <http://dx.doi.org/10.1016/j.elspec.2004.02.061>.
- [13] W. Demtröder. *Experimentalphysik 3. Atome, Moleküle und Festkörper*. Springer-Verlag, 2005.
- [14] J. H. D. Eland. Complete double photoionisation spectra of small molecules from tof-pepeco measurements. *Chemical Physics*, 294(2):171 – 186, 2003. ISSN 0301-0104. doi: DOI:10.1016/j.chemphys.2003.08.001. URL <http://dx.doi.org/10.1016/j.chemphys.2003.08.001>.
- [15] E. A. Gislason. Series expansions for franck-condon factors. i. linear potential and the reflection approximation. *J. Chem. Phys.*, 58(9):3702–3707, 1973. doi: 10.1063/1.1679721. URL <http://link.aip.org/link/?JCP/58/3702/1>.
- [16] R. Guillemin, E. Shigemasa, K. Le Guen, D. Ceolin, C. Miron, N. Leclercq, P. Morin, and M. Simon. Dynamical angular correlation in molecular auger decay. *Phys. Rev. Lett.*, 87(20):203001, Oct 2001. doi: 10.1103/PhysRevLett.87.203001. URL <http://dx.doi.org/10.1103/PhysRevLett.87.203001>.
- [17] P. Hatherly, J. Riu, M. Stankiewicz, F. Quinn, and L. Frasninski. Dynamics of the shake-up satellites of C 1s excited carbon dioxide studied by threshold electron spectroscopy. *Journal of Physics B: Atomic, Molecular and Optical Physics*, 35(3): 77–84, 2002. URL <http://www.iop.org/EJ/article/0953-4075/35/3/103/b20313.html>.
- [18] M. Hochlaf, F. Bennett, G. Chambaud, and P. Rosmus. Theoretical study of the electronic states of CO. *J. Phys. B: At. Mol. Opt. Phys*, 31(10):2163–2175, 1998. URL <http://stacks.iop.org/0953-4075/31/2163>.
- [19] M. Hoshino, K. Nakagawa, T. Tanaka, M. Kitajima, H. Tanaka, A. De Fanis, D. Mistrov, X. Brykalova, A. Pavlychev, T. Hatamoto, et al. Vibrationally resolved partial cross sections and asymmetry parameters for oxygen K-shell photoionization of the CO<sub>2</sub> molecule. *Journal of Physics B: Atomic, Molecular and Optical Physics*, 39(17):3655–3663, 2006. URL <http://www.iop.org/EJ/abstract/0953-4075/39/17/021>.
- [20] O. Jagutzki, V. Mergel, K. Ullmann-Pfleger, L. Spielberger, U. Spillmann, R. Dörner, and H. Schmidt-Böcking. A broad-application microchannel-plate detector system for advanced particle or photon detection tasks: large area imaging, precise multi-hit timing information and high detection rate. *Nucl. Instrum. Methods Phys. Res., A*, 477(1-3):244–249, 2002. URL [http://www.atom.uni-frankfurt.de/web/publications/detector\\_development/](http://www.atom.uni-frankfurt.de/web/publications/detector_development/).
- [21] T. Jahnke. *Interatomic Coulombic Decay*. PhD thesis, Goethe Universität Frankfurt am Main, 2005. URL <http://www.atom.uni-frankfurt.de/web/publications/files/TillJahnke2005.pdf>.
- [22] K. Kreidi, D. Akoury, T. Jahnke, T. Weber, A. Staudte, M. Schöffler, N. Neumann, J. Titze, L. P. H. Schmidt, A. Czasch, O. Jagutzki, R. A. C. Fraga, R. E. Grisenti, M. Smolarski, P. Ranitovic, C. L. Cocke, T. Osipov, H. Adaniya, J. C. Thompson,

- M. H. Prior, A. Belkacem, A. L. Landers, H. Schmidt-Böcking, and R. Dörner. Interference in the collective electron momentum in double photoionization of  $\text{H}_2$ . *Phys. Rev. Lett.*, 100(13):133005, 2008. doi: 10.1103/PhysRevLett.100.133005. URL <http://link.aps.org/abstract/PRL/v100/e133005>.
- [23] K. Kreidi, T. Jahnke, T. Weber, T. Havermeier, R. Grisenti, X. Liu, Y. Morisita, S. Schössler, L. Schmidt, M. Schöffler, et al. Localization of inner-shell photoelectron emission and interatomic Coulombic decay in  $\text{Ne}^-$ . *J. Phys. B*, 41(10):101002, 2008. URL <http://www.iop.org/EJ/abstract/0953-4075/41/10/101002>.
- [24] V. Kuznetsov and N. Cherepkov. Auger decay of fixed-in-space linear molecules. *J. Electron Spectrosc. Relat. Phenom.*, 79:437–440, MAY 1996. ISSN 0368-2048. URL [http://dx.doi.org/10.1016/0368-2048\(96\)02889-7](http://dx.doi.org/10.1016/0368-2048(96)02889-7).
- [25] A. Landers, F. Robicheaux, T. Jahnke, M. Schöffler, T. Osipov, J. Titze, S. Lee, H. Adaniya, M. Hertlein, P. Ranitovic, I. Bocharova, D. Akoury, A. Bhandary, T. Weber, M. Prior, C. Cocke, R. Dörner, and A. Belkacem. submitted to *Phys.Rev.Lett.*, 2009.
- [26] LBNL. ALS beamlines, technical specifications, 2008. URL <http://www.als.lbl.gov/als/techspecs/>.
- [27] F. Legare, K. F. Lee, I. V. Litvinyuk, P. W. Dooley, S. S. Wesolowski, P. R. Bunker, P. Dombi, F. Krausz, A. D. Bandrauk, D. M. Villeneuve, and P. B. Corkum. Laser coulomb-explosion imaging of small molecules. *Phys. Rev. A*, 71(1):013415, 2005. doi: 10.1103/PhysRevA.71.013415. URL <http://link.aps.org/abstract/PRA/v71/e013415>.
- [28] W. Leo. *Techniques for nuclear and particle physics experiments: a how-to approach*. Springer, 1994.
- [29] C. Letertre and B. Schorr. Multidimensional linear interpolation, 11 1984. URL <http://wwasdoc.web.cern.ch/wwasdoc/shortwrupsdir/e104/top.html>.
- [30] X.-J. Liu, H. Fukuzawa, T. Teranishi, A. D. Fanis, M. Takahashi, H. Yoshida, A. Cassimi, A. Czasch, L. Schmidt, R. Dorner, K. Wang, B. Zimmermann, V. McKoy, I. Koyano, N. Saito, and K. Ueda. Breakdown of the two-step model in k-shell photoemission and subsequent decay probed by the molecular-frame photoelectron angular distributions of  $\text{CO}_2$ . *Physical Review Letters*, 101(10):109901, 2008. doi: 10.1103/PhysRevLett.101.109901. URL <http://link.aps.org/abstract/PRL/v101/e109901>.
- [31] F. Martin, J. Fernandez, T. Havermeier, L. Foucar, T. Weber, K. Kreidi, M. Schöffler, L. Schmidt, T. Jahnke, O. Jagutzki, A. Czasch, E. P. Benis, T. Osipov, A. L. Landers, A. Belkacem, M. H. Prior, H. Schmidt-Böcking, C. L. Cocke, and R. Dorner. Single Photon-Induced Symmetry Breaking of  $\text{H}_2$  Dissociation. *Science*, 315(5812):629–633, 2007. doi: 10.1126/science.1136598. URL <http://www.sciencemag.org/cgi/content/abstract/315/5812/629>.
- [32] D. Mathur. Multiply charged molecules. *Physics reports*, 225(4):193–272, 1993.
- [33] D. Miller. *Free Jet Sources in Atomic and Molecular Beam Methods*, ed. G. Scoles. Oxford University Press, Oxford/New-York, 1998.

- [34] S. Miyabe, C. W. McCurdy, A. E. Orel, and T. N. Rescigno. Theoretical study of asymmetric molecular-frame photoelectron angular distributions for c 1s photoejection from co<sub>2</sub>. *Physical Review A (Atomic, Molecular, and Optical Physics)*, 79(5):053401, 2009. doi: 10.1103/PhysRevA.79.053401. URL <http://link.aps.org/abstract/PRA/v79/e053401>.
- [35] W. Moddeman, T. Carlson, M. Krause, B. Pullen, W. Bull, and G. Schweitzer. Determination of the K—LL Auger Spectra of N<sub>2</sub>, O<sub>2</sub>, CO, NO, H<sub>2</sub>O, and CO<sub>2</sub>. *The Journal of Chemical Physics*, 55(5):2317, 1971. URL <http://link.aip.org/link/?JCPA6/55/2317/1>.
- [36] H. Pauly. *Atom, Molecule, and Cluster Beams I*, volume 1. Springer-Verlag, 2000.
- [37] *Anweisungen zum Physikalischen Anfänger-Praktikum*. Physikalisches Institut Goethe-Universität Frankfurt, 2003.
- [38] M. N. Piancastelli. The neverending story of shape resonances. *Journal of Electron Spectroscopy and Related Phenomena*, 100(1-3):167 – 190, 1999. ISSN 0368-2048. doi: DOI:10.1016/S0368-2048(99)00046-8. URL [http://dx.doi.org/10.1016/S0368-2048\(99\)00046-8](http://dx.doi.org/10.1016/S0368-2048(99)00046-8).
- [39] K. C. Prince, L. Avaldi, M. Coreno, R. Camilloni, and M. de Simone. Vibrational structure of core to rydberg state excitations of carbon dioxide and dinitrogen oxide. *Journal of Physics B: Atomic, Molecular and Optical Physics*, 32(11):2551–2567, 1999. URL <http://stacks.iop.org/0953-4075/32/2551>.
- [40] Roentdek, 2009. URL <http://www.roentdek.de/>.
- [41] D. Rolles, G. Prümper, H. Fukuzawa, X.-J. Liu, Z. D. Pešić, R. F. Fink, A. N. Grum-Grzhimailo, I. Dumitriu, N. Berrah, and K. Ueda. Molecular-frame angular distributions of resonant co:c(1s) auger electrons. *Phys. Rev. Lett.*, 101(26):263002, 2008. URL <http://link.aps.org/abstract/PRL/v101/e263002>.
- [42] N. Saito, A. De Fanis, K. Kubozuka, M. Machida, M. Takahashi, H. Yoshida, I. Suzuki, A. Cassimi, A. Czasch, L. Schmidt, et al. Carbon K-shell photoelectron angular distribution from fixed-in-space CO<sub>2</sub> molecules. *Journal of Physics B: Atomic, Molecular and Optical Physics*, 36(1):25–30, 2003. URL <http://www.iop.org/EJ/article/0953-4075/36/1/104/b30114.html>.
- [43] M. Schmidbauer, A. Kilcoyne, H. Koeppe, J. Feldhaus, and A. Bradshaw. Shape resonances and multielectron effects in the core-level photoionization of CO<sub>2</sub>. *Phys. Rev. A*, 52:2095, 1995. URL [http://prola.aps.org/abstract/PRA/v52/i3/p2095\\_1](http://prola.aps.org/abstract/PRA/v52/i3/p2095_1).
- [44] L. Schmidt. *Effekte molekularer Symmetrien in der Elektronenemission bei langsamen He<sup>2+</sup>-He - Stoessen: Eine kinematisch vollstaendige experimentelle Untersuchung*. PhD thesis, Goethe Universität Frankfurt am Main, 2000. URL <http://www.atom.uni-frankfurt.de/web/publications/files/LotharSchmidt2000.pdf>.
- [45] L. P. H. Schmidt, S. Schossler, F. Afaneh, M. Schoffler, K. E. Stiebing, H. Schmidt-Bocking, and R. Dornier. Young-type interference in collisions between hydrogen molecular ions and helium. *Phys. Rev. Lett.*, 101(17):173202, 2008. doi: 10.1103/PhysRevLett.101.173202. URL <http://link.aps.org/abstract/PRL/v101/e173202>.

- [46] M. Schöffler. Ion focussing with an electrostatic lens. April 2009.
- [47] M. Schöffler, J. Titze, N. Petridis, T. Jahnke, K. Cole, L. Schmidt, A. Czasch, D. Akoury, O. Jagutzki, J. Williams, et al. Ultrafast Probing of Core Hole Localization in N<sub>2</sub>. *Science*, 320(5878):920, 2008. URL <http://www.sciencemag.org/cgi/content/full/320/5878/920>.
- [48] M. S. Schöffler, K. Kreidi, D. Akoury, T. Jahnke, A. Staudte, N. Neumann, J. Titze, L. P. H. Schmidt, A. Czasch, O. Jagutzki, R. A. C. Fraga, R. E. Grisenti, M. Smolarski, P. Ranitovic, C. L. Cocke, T. Osipov, H. Adaniya, S. Lee, J. C. Thompson, M. H. Prior, A. Belkacem, T. Weber, A. Landers, H. Schmidt-Bocking, and R. Dörner. Photo-double-ionization of h<sub>2</sub>: Two-center interference and its dependence on the internuclear distance. *Phys. Rev. A*, 78(1):013414, 2008. doi: 10.1103/PhysRevA.78.013414. URL <http://link.aps.org/abstract/PRA/v78/e013414>.
- [49] V. Sharma, B. Bapat, J. Mondal, M. Hochlaf, K. Giri, N. Sathyamurthy, et al. Dissociative Double Ionization of CO<sub>2</sub>: Dynamics, Energy Levels, and Lifetime. *J. Phys. Chem. A*, 111(41):10205–10211, 2007. URL <http://pubs.acs.org/doi/abs/10.1021/jp070257k>.
- [50] A. Slattery, T. Field, M. Ahmad, R. Hall, J. Lambourne, F. Penent, P. Lablanquie, and J. Eland. Spectroscopy and metastability of CO. *The Journal of chemical physics*, 122:084317, 2005.
- [51] M. M. Somoza. Franck-condon principle — wikipedia, image permission gfdl and cc-by-sa 2.5. URL <http://en.wikipedia.org/wiki/File:Franck-Condon-diagram.png>.
- [52] A. Staudte. *Subfemtosecond Electron Dynamics of H<sub>2</sub> in Strong Fields or The Quest for the Molecular Clock*. PhD thesis, Universität Frankfurt, 2005. URL <http://www.atom.uni-frankfurt.de/web/publications/files/AndreStaudte2005.pdf>.
- [53] W. Stolte, D. Hansen, M. Piancastelli, I. Dominguez Lopez, A. Rizvi, O. Hemmers, H. Wang, A. Schlachter, M. Lubell, and D. Lindle. Anionic photofragmentation of CO: a selective probe of core-level resonances. *Physical review letters*, 86(20):4504, 2001. URL <http://link.aps.org/doi/10.1103/PhysRevLett.86.4504>.
- [54] F. P. Sturm, M. Schöffler, S. Lee, T. Osipov, N. Neumann, H.-K. Kim, S. Kirschner, B. Rudek, J. B. Williams, J. D. Daughhetee, C. L. Cocke, K. Ueda, A. L. Landers, T. Weber, M. H. Prior, A. Belkacem, and R. Dörner. Photo and Auger Electron Angular Distributions of Fixed-in-Space CO<sub>2</sub>. submitted to *Phys. Rev. A*, Jun 2009.
- [55] Z. Vager, R. Naaman, and E. P. Kanter. Coulomb Explosion Imaging of Small Molecules. *Science*, 244(4903):426–431, 1989. doi: 10.1126/science.244.4903.426. URL <http://www.sciencemag.org/cgi/content/abstract/244/4903/426>.
- [56] T. Weber. *Untersuchung der verschränkten Bewegung freier Elektronenpaare emittiert aus Ein- und Zweizentren Coulomb-Potentialen in Photoabsorptionsprozessen*. PhD thesis, Goethe Universität Frankfurt am Main, 2003. URL [http://www.atom.uni-frankfurt.de/web/publications/files/Thorsten\\_Weber\\_2003screen.pdf](http://www.atom.uni-frankfurt.de/web/publications/files/Thorsten_Weber_2003screen.pdf).
- [57] T. Weber, M. Weckenbrock, M. Balsler, L. Schmidt, O. Jagutzki, W. Arnold, O. Hohn, M. Schöffler, E. Arenholz, T. Young, et al. Auger electron emission from

- fixed-in-space CO. *Physical Review Letters*, 90(15):153003–153003, 2003. URL <http://link.aps.org/doi/10.1103/PhysRevLett.90.153003>.
- [58] T. Weber, A. O. Czasch, O. Jagutzki, A. K. Müller, V. Mergel, A. Kheifets, E. Rotenberg, G. Meigs, M. H. Prior, S. Daveau, A. Landers, C. L. Cocke, T. Osipov, R. D. Muino, H. Schmidt-Böcking, and R. Dörner. Complete photo-fragmentation of the deuterium molecule. *Nature*, 431:437–440, 2004. URL <http://www.nature.com/nature/journal/v431/n7007/full/nature02839.html>.
- [59] K. Woolfe. Beamline 11.0.2 (mes) eps dwg., 11 2002. URL [http://www-controls.als.lbl.gov/alscg/docs/eps/eps\\_drawings/11\\_0\\_2.pdf](http://www-controls.als.lbl.gov/alscg/docs/eps/eps_drawings/11_0_2.pdf).
- [60] M. Yamazaki, J. Adachi, Y. Kimura, A. Yagishita, M. Stener, P. Decleva, N. Kosugi, H. Iwayama, K. Nagaya, and M. Yao. Decay channel dependence of the photoelectron angular distributions in core-level ionization of Ne dimers. *Phys. Rev. Lett.*, 101(4): 043004, 2008. URL <http://link.aps.org/doi/10.1103/PhysRevLett.101.043004>.
- [61] K. Zähringer, H.-D. Meyer, and L. S. Cederbaum. Angularly resolved auger rates of lif and hf. *Phys. Rev. A*, 46(9):5643–5652, Nov 1992. doi: 10.1103/PhysRevA.46.5643. URL <http://link.aps.org/doi/10.1103/PhysRevA.46.5643>.

# Acknowledgements

At first, I want to thank the four people who were probably the most important helping me to write this thesis. I am grateful to my professor Reinhard Dörner for having given me the opportunity to go to Berkeley and to perform there the experiment on which this diploma thesis was based on. After my return to Frankfurt, his door was always open for questions, and he took time for discussing even detailed problems of the data analysis. I am thankful for his confidence and help in writing the publication submitted to PRA. The other person who made the stay at LBNL possible was Dr. Thorsten Weber. As my supervisor in Berkeley, he organized the invitation to Berkeley Lab and took care of all necessary proceedings. He guided me through the preparation of the beamtime and was patient in explaining me how to prepare and run an experiment. His precision and care of detail are exceptional; I learned a lot from that.

I am particularly thankful and happy for the help and teaching Dr. Markus Schöffler offered me. He lead the measurements during the beamtime, and with his ease and good mood he explained me during nights at the beamline, but also afterwards, how to 'drive the taxi to its destination'. After beginning his postdoc position at LBNL and in numerous skype-sessions afterwards, he taught me data analysis with the root package and many other things. I hope that we will have the possibility to work together in the future.

Dr. Till Jahnke is the last person I would like to thank in this context. Even though he is the most wanted person in the IKF and always digged by questions from all students of our group, he took time for helping me in questions of data analysis, c<sup>++</sup> programming and physics.

With Benedikt Rudek, I shared not only the office at LBL, but also the destiny as a diploma student in Berkeley. We became good friends and have seen many beautiful sceneries and experienced great moments during our trips in California. Dr. Ali Belkacem and the whole group in Berkeley made integration in the group easy. Sun Lee taught me the procedures at the COLTRIMS chamber and showed me how to manage things at LBL. Dr. Timur Osipov, Dr. Marc Hertlein and Dr. Matthias Weckenbrock supported me whenever I needed help or advice. Unfortunately, I did not find much time for working on the high-harmonics laser system with Tom Alisson and Dr. Jeroen Van Tillborg, but still they explained me some basics. Especially Jeroen became a good friend, and I am thankful for his moral support.

During the beamtime, additionally to the people from Berkeley, there were also Nadine Neumann, Sophie Kirschner and Hong-Keun Kim, as well as Prof. Allen Landers, Joshua Williams and Jacob Daughhetee putting a lot of effort in the success of the experiment. Special thanks to Dr. Hendrik Bluhm for helping so much during the beamtime and for the idea of the focus-adjustment scintillator.

Even though we were not working together on a specific experiment, Dr. David Kilcoyne was somewhat of a mentor, explaining me numerous things at the ALS and sharing his long experience.

I would like to thank the whole group in Frankfurt but I can try to specify this somehow. I thank Katharina Kreidi for introducing me in the group and for my first beamtime, Dr. Achim Czasch and Dr. Lutz Foucar for their help in c<sup>++</sup> programming, Dr. Lothar Schmidt for answering any random electronics question and Dr. Robert Grisenti for his help as an expert in gas-expansions. I am grateful for enriching discussion with Robert,

Sven, Jasmin, Moritz, Tilo (thanks for the gas-expansion template), Birte. Special thanks to Nikos for clubbing in Frankfurt.

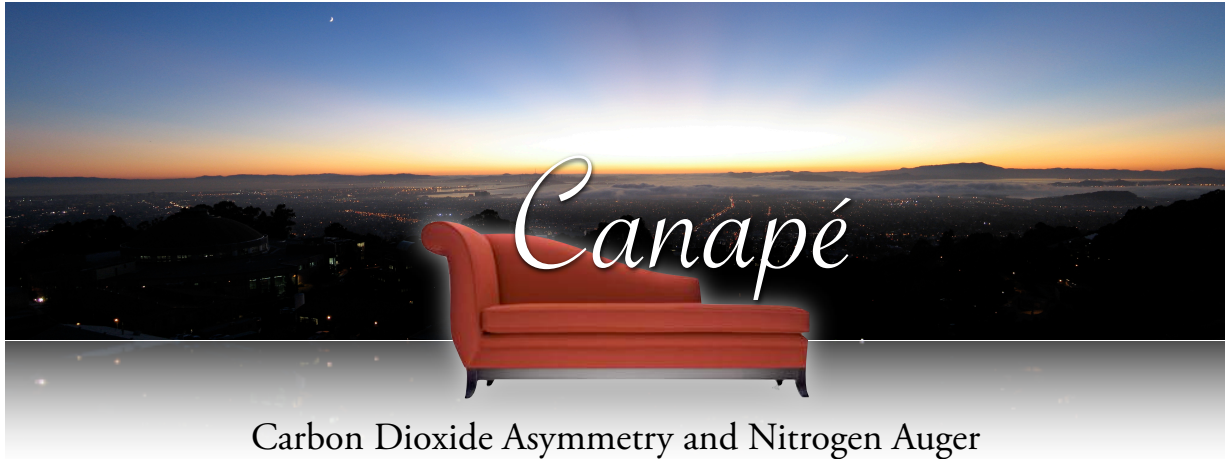
Fortunately I met so many friends in Berkeley who made the stay in California amazing. A big hug for my flat-mates and now good friends Zsuzsana and Lauriane and to and Kathi, Sebastien and Kevin. Thanks to the best party-crew ever: Ali, Sebastian, Manuel, Patricia, Jen, Katie, Raphael, Antoine, Jessie, Don and Jonathan. Hard work will only be successful if you let it rest sometimes and take the time to free your mind.

With my good friend Heike Berleth, I spent so much time together during our physics studies, calculating exercises and enjoying life in Paris. She has some responsibility for this work, telling me finally to start in Prof. Dörner's group. I thank one of the best theoretical physicists Ulf Bissbort for his patience in explaining and especially derivation of several problems in quantum mechanics and statistics.

Thanks to Holger for providing me a  $\text{\LaTeX}$  template and to Erin for proofreading the thesis.

Last but not least, I am grateful to my parents and my sister for always having supported me in every possible way.

I dedicate this work to my grandmother Elsa Hagemeyer who would be so happy to see me now, and to Marianne Beuchert who always predicted that I would become a professor one day, but "hopefully not in atomic physics".



Carbon Dioxide Asymmetry and Nitrogen Auger  
Electron Photoionization Experiment